

Dissertation for Doctor of Philosophy

**A Multiscale Computational Study of Brain Stimulation:
Investigation of Activation of Cortical Neurons**

Hyeon Seo

School of Electrical Engineering and Computer Science

Gwangju Institute of Science and Technology

2017

박사학위논문

뇌 자극에 관한 멀티스케일 시뮬레이션 연구:
대뇌 피질 신경세포의 활성화 조사

서 현

전 기 전 자 컴 퓨 터 공 학 부

광 주 과 학 기 술 원

2017

A Multiscale Computational Study of Brain
Stimulation: Investigation of Activation of Cortical
Neurons

뇌 자극에 관한 멀티스케일 시뮬레이션 연구:
대뇌 피질 신경세포의 활성화 조사

Dedicated to my family.

PhD./EC Hyeon Seo. A Multiscale Computational Study of Brain Stimulation: Investigation
20132003 of Activation of Cortical Neurons. School of Electrical Engineering and Computer
Science. 2017. 102p. Prof. Sung Chan Jun.

Abstract

Brain stimulation is an appealing method for the treatment of neurological disorders. To achieve optimal stimulation parameters and a better understanding of the underlying mechanisms, we applied computational modeling studies of brain stimulation. In this dissertation, we investigate the effects of brain stimulation encompassing noninvasive to invasive approaches to the neural activations. Furthermore, we try to increase the realism and detail of the volume conductor model of the head to find the precise target sites and how neural responses vary with stimulation types. The anatomically realistic head model was constructed using magnetic resonance imaging to reflect precise anatomical information. Then, we attached electrodes onto the scalp or into the brain according to stimulation types. For transcranial magnetic stimulation magnetic dipoles representing coil were considered. Using these head models, we calculated realistic electric fields and integrated them into the compartmental neuronal models. The cellular targets and initiation sites were analyzed according to different stimulation types. During the subdural cortical stimulations, we found that the target regions varied according to stimulus polarities and that anodal stimulations activate the top of the gyrus and that cathodal stimulations induce a relatively lower excitability at the lip and bank along the sulcus. For the transcranial magnetic stimulation, neural excitability was characterized as a function of coil orientation. We also proposed a semi-invasive approach—the transcranial channel combined with the transcranial direct current stimulation—to improve the focality and magnitude of neuromodulation. The outcome of this dissertation could provide insights into the action mechanisms of brain stimulation and the predicted outcome from therapy.

©2017

Hyeon Seo

ALL RIGHTS RESERVED

국 문 요 약

뇌 자극 기법이란 외부 전기적 자극을 통해 뇌를 활성화 시키는 치료요법으로 난치병으로 알려져 있는 여러 뇌 질환에 대해 효과가 보고되고 있다. 하지만 치료 효과에 대한 메커니즘 이해 부족으로 타겟 영역이나 자극 조건이 무분별하다는 한계를 가지고 있다. 본 논문에서는 시뮬레이션 연구를 통해 최적화된 자극 조건을 제시하고 이에 따른 메커니즘에 대한 이해를 돕고자 한다. 뇌 자극의 전기적/자기적 방식에 따른 영향과 전극의 침습 정도, 자극의 세기 및 그 밖의 다양한 성질에 따른 변화를 관측하기 위해 자기공명영상을 이용한 해부학적 정교 뇌 모델과 대뇌 피질 신경세포를 구축하였다. 구축된 시뮬레이션 환경을 통해 외부 전기 자극에 따라 발생하는 전기장 분포를 보다 정확히 계산하고 신경세포에 전달함으로써 활성화 역치와 발생하는 위치 등을 분석하였다. 침습적 뇌 자극 시, 양극의 경우 뇌회 윗부분에 위치한 신경세포들의 활동 전위가 유도됐으며 음극의 경우 열구를 따른 뇌회 벽면에 위치한 신경세포들에 대해 상대적으로 낮은 활성화 반응이 유도됨을 관측하였다. 비침습적 자기 자극의 경우 신경세포의 활성화 반응이 코일의 방향과 대응되는 특징을 보였고 준침습성 자극을 통해 외부 자극을 손실없이 뇌에 집중적으로 전달할 수 있음을 확인하였다. 본 논문에서는 다양한 뇌 자극 기법에 따른 신경세포의 활성화 반응을 조사하여 자극에 따른 기전의 이해를 돕고 더 나아가 자극의 효과를 예측하였다.

©2017

서 현

ALL RIGHTS RESERVED

Contents

Abstract	i
List of contents	iii
List of Tables.....	vi
List of Figures	vii
I. Introduction.....	1
1.1 Overview of electrical brain stimulation.....	1
1.2 Volume conductor model of the human head	2
1.2.1 Field computation for electrical stimulation	4
1.2.2 Field computation for magnetic stimulation	6
1.2.3 Electrode factors	7
1.2.4 Conductivity properties	7
1.3 Computation of neural activation.....	8
1.3.1 Activating function.....	8
1.3.2 Multi-scale Modeling	10
1.4 Outline of the dissertation	11
1.4.1 Effect of Anatomically Realistic Full-Head Model on Activation of Cortical Neurons in Subdural Cortical Stimulation—A Computational Study	12
1.4.2 Computational Study of Subdural Cortical Stimulation: Effects of Simulating Anisotropic Conductivity on Activation of Cortical Neurons	12
1.4.3 A multi-scale computational model of the effects of TMS on motor cortex	12
1.4.4 Effect of a Transcranial Channel as a Skull/Brain Interface in High-Definition Transcranial Direct Current Stimulation—A Computational Study.....	13
II. Effect of Anatomically Realistic Full-Head Model on Activation of Cortical Neurons in Subdural Cortical Stimulation—A Computational Study	14
2.1 Introduction.....	14
2.2 Methods	15

2.2.1 Two head models of subdural cortical stimulation	1 5
2.2.2 Conductivity assignment	1 7
2.2.3 Compartment models of pyramidal neurons	1 8
2.3 Results.....	1 9
2.4 Discussion.....	2 6
III. Computational Study of Subdural Cortical Stimulation: Effects of Simulating Anisotropic Conductivity on Activation of Cortical Neurons	3 2
3.1 Introduction.....	3 2
3.2 Methods	3 3
3.2.1 Construction of the anatomically realistic head model.....	3 3
3.2.2 Conductivity assignment	3 5
3.2.3 Compartment models of pyramidal neurons.....	3 7
3.3 Results.....	3 9
3.3.1 Comparison between anisotropic and isotropic conductivity	3 9
3.3.2 Comparison among various anisotropic conductivities	4 1
3.4 Discussion.....	4 4
IV. A multi-scale computational model of the effects of TMS on motor cortex.....	5 0
4.1 Introduction.....	5 0
4.2 Methods	5 1
4.2.1 Volume conductor model	5 1
4.2.2 Field calculations.....	5 2
4.2.3 Multi-compartmental neuronal models.....	5 3
4.2.4 Computation of neuronal activation induced by stimulation	5 4
4.3 Results.....	5 4
4.4 Discussion.....	6 2

V. Effect of a Transcranial Channel as a Skull/Brain Interface in High-Definition Transcranial Direct Current Stimulation—A Computational Study	6 7
5.1 Introduction.....	6 7
5.2 Methods	6 8
5.2.1 The volume conduction model of an anatomically realistic head.....	6 8
5.2.2 The compartmental model of pyramidal neurons	6 9
5.3 Results.....	7 0
5.3.1 Effects of varying the dimension of the transcranial channel	7 0
5.3.2 Displacement of the electrodes from the transcranial channel.....	7 9
5.4 Discussion	8 0
VI. Conclusion and discussion	9 0
References	9 2

List of Tables

2.1 The minimum threshold (mA) for each polarity in comparison between the extruded slab model and the anatomically realistic head model	22
3.1 Conductivities of tissues and electrodes.....	35
3.2 Longitudinal and transverse conductivity of WM tensor elements calculated using the artificial anisotropy with volume constraint according to anisotropic factors	36
3.3 The minimum excitation thresholds (mA) over three polarities between the anisotropic and isotropic models; parentheses indicate the location of the neuron(s) excited.....	42
3.4 The minimum excitation thresholds (mA) of L5 neurons in the anatomically realistic head model over the six anisotropic models.	45
5.1 Variation in the stimulus-induced EF within the brain with increments in the shaft diameter of the T- and I-shaped channels.	71

List of Figures

1.1 The four-layer concentric sphere head model	3
1.2 The anterior-posterior cross-section of the extruded slab model of the precentral gyrus with surrounding structures.	3
1.3 The tetrahedral finite element meshes constructed from MRI.....	4
1.4 Compartmental models of cortical neurons.....	10
2.1 The shape of the extruded slab model	16
2.2 The shape of the anatomically realistic head model.....	17
2.3 Schematic view of distribution of the compartmental pyramidal neuronal models.	19
2.4 The spatial extent of the excitation thresholds in the extruded-slab model.	21
2.5 The spatial extent of the excitation thresholds projected on the cortical surface in the anatomically realistic head model.....	23
2.6 The relative ratio (%) of neurons excited with three different polarities: (anodal (A); cathodal (C), and bipolar (B) stimulations).	24
2.7 Initiation site of action potential over anodal (+) and cathodal (–) stimulation	25
3.1 The shape of the anatomically realistic head model.....	34
3.2 Schematic view of the neuronal model morphology and placement.	37
3.3 Placement of L5 and L3 pyramidal neuronal models in the anatomically realistic head model.....	38
3.4 Comparison between isotropic and anisotropic conductivity for anodal, cathodal and bipolar stimulation.....	40
3.5 The relative ratio (%) of neurons excited with stimulation at three different polarities (anodal (A), cathodal (C), and bipolar (B) stimulation).....	41
3.6 Comparison among various anisotropic conductivities for anodal, cathodal and bipolar stimulation .	43
3.7 The relative ratio of the number of L5 neurons excited for three polarities	44
4.1 The volume conductor model and coil placement	52
4.2 The placement of L5/L3 PNs in the head model.	53
4.3 Effects of coil orientation on the electric fields.....	55
4.4 The spatial extent of predicted excitability based on the orthogonal component of the electric field (E_{\perp}) and detailed simulations of L5/L3 PNs.....	57
4.5 The percentage of L5 and L3 PNs that are activated for a stimulation intensity at the motor threshold	

(67 A/ μ s) as a function of coil orientation	58
4.6 The percentage of action potential initiation sites of L5 and L3 PNs for a stimulation intensity corresponding to the motor threshold over different coil orientations.....	59
4.7 Virtual recordings of membrane potential dynamics of L5/L3 PNs	60
4.8 The impact of dendritic tree morphology of L5 PNs was evaluated by rotating them in steps of 45° for a fixed coil orientation at +180°	61
5.1 The shape of the anatomically realistic head model	68
5.2 Distribution patterns of stimulus-induced EFs decomposed into radial and tangential fields on the cortical surface	72
5.3 Membrane polarization for neuronal compartments in L5 and L3 PNs with various diameters of the T-shaped transcranial channel	74
5.4 The spatial extent of membrane polarizations for L5 and L3 PNs focused on precentral gyrus	76
5.5 Distribution patterns of stimulus-induced electric fields on cross-sectional view.....	78
5.6 Distribution patterns of stimulus-induced electric fields when the electrodes and T-shaped channel are placed above the central sulcus	78
5.7 The spatial extent of membrane polarization of L5 (a) and L3 (b) PNs when the electrodes and T-shaped channel are placed above the central sulcus	80
5.8 The impacts of morphology of L5 PNs on stimulus-induced membrane polarizations in the HD-tDCS combined with T-shaped transcranial channel	81
5.9 The relationship between somatic size and stimulus-induced polarization	82
5.10 EF distributions with respect to displacement of the center (active) electrode relative to the transcranial channel	83
5.11 The distributions of membrane polarization in neuronal compartments (ROI) in L5 (a) and L3 PN (b)	85

I. Introduction

1.1 Overview of electrical brain stimulation

Electrical brain stimulation is an intriguing electrotherapy designed to expedite neuronal modulation in the brain through a regulated current. Brain stimulation has been applied as a treatment for various neurological disorders and as an adjunct to medical therapy when chemical or surgical techniques cannot achieve a satisfactory level of improvement. It spans the fields of functional neurosurgery, such as chronic pain¹⁻⁴, rehabilitation⁵⁻⁸, Parkinson's disease^{2,9-11}, essential tremor^{2,12}, and other brain disorders.

Brain stimulation can be performed in both noninvasive and invasive approaches, depending on whether input devices are implanted. At the beginning, an implanted electrical brain stimulation was proposed to treat chronic refractory neuropathic pain¹³, and a later noninvasive approach for several neurological and psychiatric disorders was reported^{14,15}. Compared to non-invasive stimulation, invasive procedures enable one to selectively target specific regions of the cortex more effectively and provide superior effects for such disabilities as chronic pain and movement disorders¹⁶⁻¹⁸. Invasive stimulation is classified by epidural cortical stimulation (ECS) through electrodes located above the dura mater, and subdural cortical stimulation (SuCS) is achieved by placing electrodes below the dura mater. The invasive approach, in particular, has some advantages, including targeting the cortical surface with a less intense current than in a noninvasive approach. However, this approach is not as safe as noninvasive ones^{6,16,17} that allow neuromodulation without surgical procedures¹⁹⁻²².

The transcranial direct current stimulation (tDCS) and transcranial magnetic stimulation (TMS) are the most commonly used techniques for noninvasive brain stimulation. tDCS allows neuromodulation by delivering a weak direct current (up to 2 mA) through electrodes on the scalp. This method has attracted considerable interest, as it is safe, inexpensive, portable, and simple to implement^{19,20}. Conventional tDCS with rectangular pads conveys a weak current that is distributed broadly over a large brain area. As the scalp has high impedance, most of the current applied is shunted, and therefore, the currents that enter the brain are weakened and activate a relatively larger brain area^{23,24}. Because an electrode montage of tDCS can shape the induced current's distribution^{21,25,26}, to achieve the targeted neuromodulation, Datta et al. proposed an

advanced montage of high-definition tDCS (HD-tDCS), that has an active center electrode surrounded by four return electrodes to enhance spatial focality^{23,26}. Physiological studies of HD-tDCS have explored its plasticity effects in pain and motor excitability^{24,27–29}. In comparison, TMS is a neurostimulation and a neuromodulation technique that noninvasively activates neurons in the brain^{30,31}. It generates a time varying magnetic field using a coil above the head, which induces an electric field in the brain that can be of sufficient magnitude to depolarize neurons. In recent years, TMS has been widely tested as a tool for the diagnosis and treatment of a broad range of neurological and psychiatric disorders^{32–34}.

Despite its widespread use, brain stimulation has been employed with lesser tuned stimulation parameters that are determined primarily by clinical experience, due to the lack of a complete understanding about how the current input propagates in the cortex and which cortical targets are activated. Furthermore, the large number of potential combinations of stimulation parameters (e.g., electrode shape and placement, stimulus amplitude, frequency, polarity, pulse width, etc.) lead to uncertain therapeutic outcomes¹⁷, thereby making it more difficult to determine the optimal parameters. A computational study is therefore one of the most useful approaches in investigating the influence of these various parameters.

Recent research has been conducted to analyze the underlying mechanism of CS via a computational approach to determine optimal stimulation parameters. Such studies have led to improvements in therapeutic effects by inferring neuronal excitability from the estimated electric field (EF) or current density (CD) induced by input current^{21,23,26,35–50} or by incorporating neuronal models^{51–63}.

1.2 Volume conductor model of the human head

To elucidate the spatial extent of the induced electric field or current density, a volume conductor model of a human head is proposed, and two forms of simplified and anatomically realistic head models have been used primarily. The simplified head model for the noninvasive approach is a simple concentric spherical model composed of three and four layers based on the assumption that the head is a perfect sphere to reduce complexity^{26,64–67}, as shown in Figure 1.1. This model shows quantitative consent by using the electroencephalographic and magnetoencephalographic data and experimental results for transcranial stimulation^{68,69}.

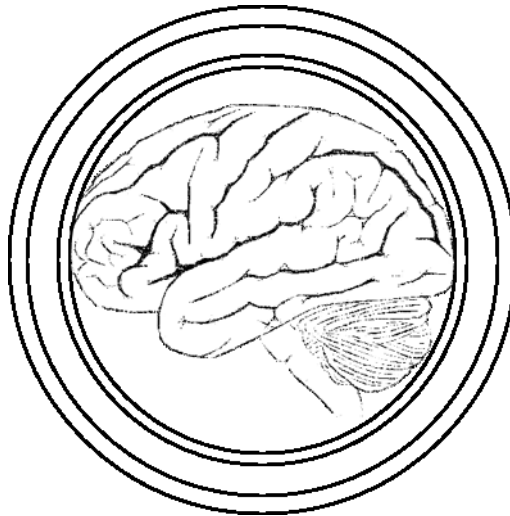


Figure 1.1 The four-layer concentric sphere head model. Tissue layers from outer to inner composite scalp, skull, cerebrospinal fluid and brain.

Another form of simplified head model applied for invasive stimulation is an extruded slab model that represents a part of the brain, typically the precentral gyrus area^{35,36,52,53,61,63,70}, as shown in Figure 1.2. The extruded slab model is composed of precentral gyrus and surrounding sulci and gyri because invasive stimulation may stimulate a relatively focal area of the brain compared to noninvasive stimulation. The extruded slab model is composed of a higher number of layers compared to the sphere model, such as the

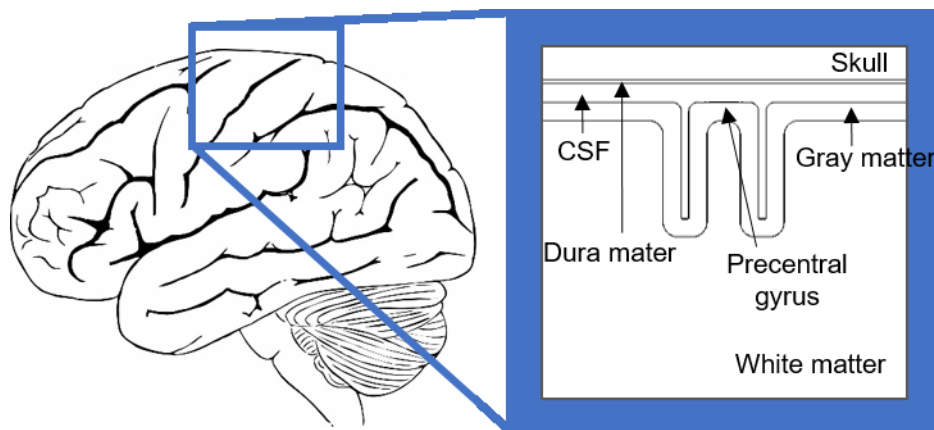


Figure 1.2 The anterior-posterior cross-section of the extruded slab model of the precentral gyrus with surrounding structures. This model applies epidural or subdural cortical stimulation by placing the electrodes on the dura mater or under the dura mater.

scalp, skull, dura mater, cerebrospinal fluid (CSF), gray matter (GM) and white matter (WM), as the electrodes for invasive stimulation are placed closer to the brain. The simplified head models, which are the sphere and extruded slab models, generalize the head size and structure, and thus they limit a direct link between an estimated stimulus-induced electric field and individual physiological observations.

To provide precise information about head anatomy, an anatomically realistic head model is constructed that represents the entire geometry of the head, and this model helps to calculate the realistic electric field that are undisputed in estimating the target area accurately^{21,23,37–50}. The individualized anatomically realistic head model is constructed using magnetic resonance images (MRIs), as shown in Figure 1.3. The process is started by extracting the borders between different materials and then creating tetrahedral finite element meshes. The anatomically realistic head model reflects not only anatomical information but also anisotropic conductivity utilizing diffusion tensor imaging (DTI), but it comes at a significant computational cost.

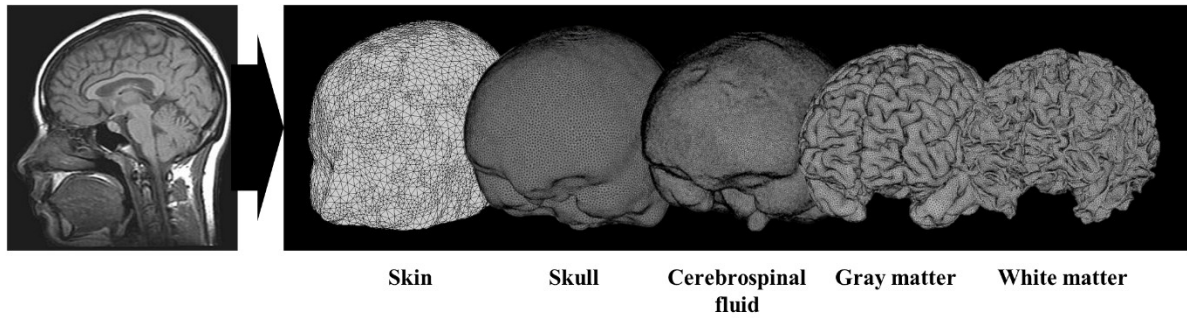


Figure 1.3 The tetrahedral finite element meshes constructed from magnetic resonance imaging. Volumetric depictions of skin, skull, cerebrospinal fluid, gray matter, and white matter are illustrated.

1.2.1 Field computation for electrical stimulation

Based on quasi-static approximations, $\partial E / \partial t$ and $\partial B / \partial t$ in the calculation of E (electric field) and B (magnetic field) in Maxwell's equations can be ignored as source terms^{71,72}. Thus we can get below quasi-static approximation of Maxwell's equations:

$$\nabla \cdot E = \frac{\rho}{\epsilon_0}$$

$$\nabla \times E \approx 0$$

$$\nabla \cdot B = 0$$

$$\nabla \times B \approx \mu_0 J,$$

where ρ is charge density, ϵ and μ stand for physical properties of the media, and J is current density.

From these equations, we can derive two facts:

$$\text{Fact 1. } \nabla \times E = 0 \Rightarrow E = -\nabla V \quad \because (\nabla \times (\nabla f) = 0 \text{ for all } f)$$

$$\text{Fact 2. } \nabla \times B = \mu_0 J \Rightarrow \nabla \cdot J = 0 \quad \because (\nabla \cdot \nabla \times B = 0 = \nabla \cdot \mu_0 J).$$

The total current emerging in the brain is usually composed of two terms: primary current ($J^p(r)$) that flows from the source (dendritic trees of pyramidal cells of the cortex) and impressed secondary current ($J^v(r) = \sigma(r)E(r)$, where σ denotes the electric conductivity) that is a passive current arising from a bioelectric source .

The formulation produced by electrical stimulation is made by assuming that bioelectrical sources have a negligible impact on the stimulus-induced electric field⁵². Therefore, only a passive current is left and then the total current is expressed as follows:

$$J^{\text{total}} = \sigma E.$$

Following Fact 1, the electric field E is expressed as the negative gradient of the potential field and the total current becomes:

$$J^{\text{total}} = -\sigma \nabla V.$$

Substituting total current into the equation of Fact 2 yields the Laplace equation of the potential field:

$$\nabla \cdot \sigma \nabla V = 0.$$

The boundary conditions applied are the Neumann boundary condition in which the electric current that flows through the scalp is negligibly small the surface of the scalp (current density = 0), and the external stimulus through electrodes are applied as $V = \text{constant}$ at the electrode surface^{35,52}.

Finally, we can divide the problem domain into many subdomains (called finite elements) of the constructed tetrahedral element meshes. In order to solve the differential equations and given conditions, the finite element method (FEM) is incorporated as it can easily handle any complex shape of a problem's domain with a prescribed condition.

1.2.2 Field computation for magnetic stimulation

Similar to that described in field computation for electrical stimulation (1.2.1), the electric field induced by magnetic stimulation follows in the quasi-static approximation of Maxwell's equations^{41,73–77}:

$$\vec{E} = -\frac{\partial \vec{A}}{\partial t} - \nabla V = -\vec{E}_p - \vec{E}_s,$$

with the vector potential \vec{A} and electric potential V . The electric field induced by TMS is composed by the sum of the primary electric field (\vec{E}_p) that is induced directly by the changing magnetic field from the coil and the secondary field (\vec{E}_s) that is the scalar potential field caused by charge accumulations at tissue interfaces.

The primary electric field (\vec{E}_p) that is completely determined by the coil geometry is described by^{74,78,79}:

$$\frac{d\vec{A}}{dt} = \frac{\mu_0 N dI/dt}{4\pi} \int \frac{d\vec{l}}{|\vec{r} - \vec{r}_0|},$$

where $\mu_0 = 4\pi \times 10^{-7} \text{H/m}$ is the permeability of free space, and N is the number of windings in the coil with the time dependent coil current dI/dt . The integration is performed with the vector $d\vec{l}$ that is vector representing the source point to the field point. Thus the primary electric field is calculated straight-forward by approximating the coil by many magnetic dipoles.

The secondary field (\vec{E}_s) is then computed via FEM using magnetic vector potential \vec{A} as input. We can derived the Poisson equation for electric potential V that is solved in the volume conductor model by multiplying electric field with the conductivity tensor σ and using the subset of Maxwell's equation under quasi-static conditions ($\nabla \times \frac{1}{\mu} B = -\sigma E$):

$$\nabla \times \frac{1}{\mu} B = -\sigma \frac{\partial \vec{A}}{\partial t} - \sigma \nabla V \Rightarrow \nabla \cdot \sigma \nabla V = -\nabla \sigma \frac{\partial \vec{A}}{\partial t} \because (\nabla \cdot \nabla \times B = 0).$$

The Neumann boundary condition is applied, as follows:

$$\vec{n} \cdot \vec{j} = 0 \Leftrightarrow \vec{n} \cdot \sigma \vec{E} = 0 \Leftrightarrow \vec{n} \cdot \left(\sigma \nabla V + \sigma \frac{\partial \vec{A}}{\partial t} \right) = 0.$$

Ampere's law with current conservation is applied and the electric field induced by magnetic stimulation is

solved by the sum of the primary electric field given by a gradient of vector potential and the secondary field that can be expressed as the gradient of the potential field.

1.2.3 Electrode factors

The electrode's size, number, shape and location are crucial factors that determine the stimulus targets. For example, conventional transcranial current stimulation uses rectangular pads to deliver a weak current through electrodes on the scalp; however, they activated a relatively larger brain area, and an even higher intensity of the electric field has occurred beside the area under the target electrode^{16,23,24}. To improve the focality of the spatial distribution of the electric field, a smaller target electrode and a bigger reference electrode are introduced. Advanced configuration, called high-definition tDCS (HD-tDCS), is proposed. This configuration consists of an active center electrode surrounded by four return electrodes for targeted neuromodulation^{23,26}, and the researchers revealed that HD-tDCS induces the maximal stimulus-induced electric field magnitude directly underneath the target electrode with enhanced focality compared to conventional tDCS. For the subdural cortical stimulation, a paddle-array electrode showed a synergistic effect such that the affected brain area becomes larger and deeper when stimulus amplitude was about 2V, but we could not observe this effect using a single electrode⁸⁰. Various coil designs for TMS have been proposed, as the locus of neural activation can be approximated where the stimulus-induced electric field is maximal⁸¹. Deng et al., quantified the focality and depth of penetration of the electric field by incorporating 50 coils and found a depth-focality trade-off⁸². The figure 8 coil has been used widely to produce more focalized electric field, while the coils induced a wider electric field in which the circular coil had the ability to stimulate deeper regions directly. Additional novel coil designs for TMS are continually being introduced^{82,83}.

1.2.4 Conductivity properties

The different tissues of the head model have inhomogeneous electrical properties and the white matter is well known to be anisotropy. With head tissues, the skull has less conductivity and consists of a soft bone layer (spongiosa) enclosed by two harder bone layers (compacta). Since the skull has lower conductivity and the scalp has high impedance, both play a vital role during tDCS by causing a large shunting effect and shifting the stimulated areas¹⁹. Inside the skull, cerebrospinal fluid that is a clear body fluid with high

conductivity and the current produced by tDCS flows through the high conductive cerebrospinal fluid and results in the diffusion of the current. Isotropic conductivity for gray matter is considered as this matter is mainly composed of cell bodies. White matter consists of the axons mostly projecting to other areas, and thus it has higher anisotropic conductivity such that the induced-current flows along fibers.

White matter anisotropy is important for targeting deeper brain regions⁴⁵. Diffusion tensor imaging (DTI) provides conductivity tensor information from which we can infer anisotropic properties of white matter by the diffusion tensor; the details about how to incorporate anisotropic conductivity are introduced in section 3.2.2.

1.3 Computation of neural activation

Electrical brain stimulation induces external electric fields and the neurons within these fields may be depolarized and/or hyperpolarized from their resting state. For example, depending upon the polarity of transcranial direct current stimulation, anodal stimulation increases the cortical excitability while cathodal stimulation induces inhibition⁸⁴⁻⁸⁶. When a stimulus-induced electric field can be of such a sufficient magnitude that its depolarization may reach the threshold, the action potential is generated. However, the neuronal activation is not simply determined by stimulus amplitude. There are many combinations of crucial factors that affect the amounts and pattern of neural polarization such as neuronal morphology, electrical properties, and stimulus-induced field direction, frequency, and wave form. Thus the magnitude of the electric field and current density might introduce an insufficient prediction of the patterns of neural targets. Then with just the field's strength, we still cannot understand the detailed biophysical mechanisms.

1.3.1 Activating function

The prediction of changes in transmembrane potential by the external stimuli can be determined by an electrical circuit representing the cable equation. The most acceptable passive cable equation that contains active Hodgkin-Huxley elements was developed by Roth and Bassar⁸⁷, and the model is appropriate for describing the subthreshold behavior induced by electromagnetic stimulation. The neuron is approximated by a series of small compartments, and then the current flow across the i -th membrane as described below:

Ohm's law: $r_i I_i = -\partial V / \partial x$

The law of conservation of current: $i_m = -\partial I_i / \partial x$

The membrane current is given by, $i_m = c_m \partial V / \partial t + V / r_m$.

r_i : a resistance per unit length

I_i : the axial intra-cellular current

i_m : the membrane current per unit length

V : intracellular potential

c_m : capacitance per unit length

r_m : resistance times unit length

The combination of these equations yields,

$$r_m c_m \frac{\partial V}{\partial t} + V = \frac{r_m}{r_i} \frac{\partial^2 V}{\partial x^2}.$$

This equation considers the axial component of the electric field as a negative gradient of the intracellular potential. When the external stimuli are applied, the additional source of electric field is added,

$$r_i I_i = -\partial V / \partial x$$

$$\Leftrightarrow E_i = -\partial V / \partial x + E_x(x, t).$$

Then the equation is altered to include the external source:

$$r_m c_m \frac{\partial V}{\partial t} + V = \frac{r_m}{r_i} \frac{\partial^2 V}{\partial x^2} - \frac{r_m}{r_i} \frac{\partial E_x}{\partial t}.$$

Before the external stimuli are applied, the intracellular potential and its derivative are zero, and thus the second term on the left side and first term on the right side will drop out. Under these conditions, the changes in the membrane's potential is approximated to the derivative of the additional source of the electric field (activating function):

$$\frac{\partial V}{\partial t} = -\frac{1}{r_i c_m} \frac{\partial E_x}{\partial t}.$$

The activating function is widely used to approximate the polarization of neural elements in the cortex. During epidural cortical stimulation, while higher electric field strength has focused on the top of gyrus, the activating function exhibited different patterns between anodal and cathodal stimulations^{35,52}. However, cathodal stimulation showed inverted signs of the activating functions induced by anodal stimulation due to

the linearity of the head model with respect to electrical field. In addition, analysis using the electric field could not consider different neuronal morphologies and their electrical properties. Therefore, morphologically reconstructed compartmental neuronal models are incorporated into the volume conductor head model to yield a more accurate estimation of neuronal activation.

1.3.2 Multi-scale Modeling

Describing the neural targets remains a challenge due to their complicated morphology and cellular geometry (Figure 1.4). It has been investigated using multi-compartmental models of cortical neurons^{51,87-93}, and then the researchers found the type of cell that is preferentially activated. They also analyzed the threshold of action potential, the action potential initiation sites, what the spatial patterns of the threshold are, and the way the membrane polarization interacts with the stimulus-induced electric field.

For the fundamental questions regarding the neural targets, Radman et al. reconstructed morphologically and functionally diverse groups of inhibitory interneurons and excitatory pyramidal neurons from rats when

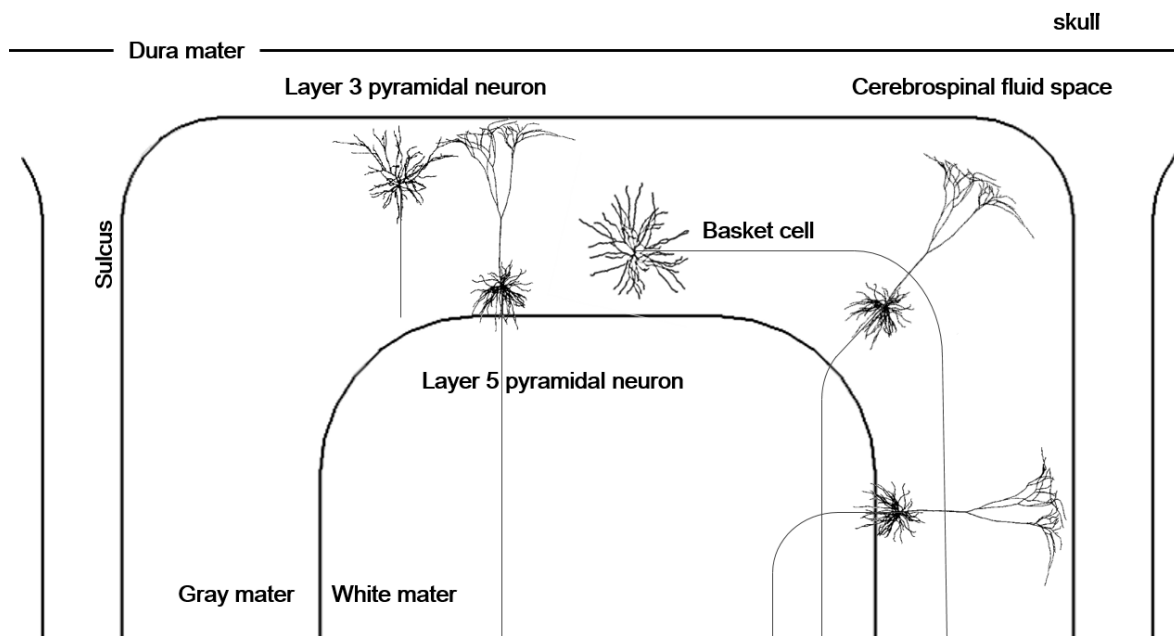


Figure 1.4 Compartmental models of cortical neurons. Note that pyramidal neurons orient to the perpendicular direction to the cortical surface within the gray matter, then the axons of layer 5 pyramidal cell bends differently toward internal capsule.

the neuronal models were positioned inside the uniform electric fields⁵⁵. They found a linear polarization according to stimulus amplitude at subthreshold fields and non-linear responses at suprathreshold fields. Likewise, the neuronal responses produced by noninvasive stimulation were investigated on the uniform electric field; for transcranial magnetic stimulation, the uniform field was considered due to the small size of neurons compared to the stimulation coils⁵¹. During transcranial direct current stimulation the uniform electric field was assumed due to the observation of the uniform voltage gradient in gyri-precise head model⁵⁶. In contrast to noninvasive stimulation in which the applied current was dispersed, invasive stimulation induced a focalized electric field. Therefore, rather than considering a uniform electric field, they tried to incorporate a distribution of stimulus-induced electric field to the compartmental neuronal models by virtually combining them into the extruded slab model^{53,59,61,63}. The neuronal models were coupled with the extruded slab model by positioning a series of center points composing compartments of neuronal models because the neuronal models consisted of a series of compartments connected by resistors and the differential cable equation could be solved at each center point of each compartment. The stimulus-induced potential fields were then calculated and subjected to extracellular mechanisms. Through activation of cortical neurons, the precise target region could be observed according to various stimulus parameters and the protocols that were selectively target either the basket cell or pyramidal cells could be observed. However, while the neuronal activation was determined by the potential field generated by the head model, the extruded slab model could not provide the realistic potential field compared to the anatomically realistic head model. While coupling neuronal models with the extruded slab model was quite straightforward, the anatomically realistic head model required complicate procedure due to its irregular geometry. Despite the higher computational cost to incorporate neuronal models into the anatomically realistic head model, this had advantages in that we can predict more precise and subject-specific target regions according to the individual head models^{58–60,94}.

1.4 Outline of the dissertation

The goal of this research is to investigate the activation of cortical neurons using multi-scale modeling and the cellular target area and their responses produced by the brain stimulation encompassing invasive to noninvasive approaches. Subsequent chapters of this dissertation will address the following aims:

1.4.1 Effect of Anatomically Realistic Full-Head Model on Activation of Cortical Neurons in Subdural Cortical Stimulation—A Computational Study

Two kinds of head models are used for subdural cortical stimulation: the extruded slab model and the anatomically realistic head model. The extruded slab model is composed by regular geometry and thus can be coupled with neuronal models with ease; however, it could induce inaccurate predictions of neural responses due to model simplicity. In contrast, the anatomically realistic head model increases realism, but it requires not only a huge computational cost but also considerable manual works for construction.

In Chapter 2, we constructed two types of head models—the extruded slab model and the anatomically realistic head model—for subdural cortical stimulation and these head models were coupled with compartmental neuronal models of layer 5 and layer 3 pyramidal neurons. Then we investigated whether the anatomically realistic head model yielded better estimation of activation of pyramidal neurons compared to the extruded slab model. We found that layer 3 pyramidal neurons had comparable stimulation thresholds in both head models, while layer 5 pyramidal neurons showed a notable discrepancy between the models; in particular, layer 5 pyramidal neurons demonstrated asymmetry in the thresholds and in the action potential initiation sites in the anatomically realistic full-head model.

1.4.2 Computational Study of Subdural Cortical Stimulation: Effects of Simulating Anisotropic Conductivity on Activation of Cortical Neurons

One of the benefits of the anatomically realistic head model is that we could incorporate anisotropic information through diffusion tensor imaging. In Chapter3, we investigated the impact of incorporating anisotropic conductivity of the white matter with various ratios of anisotropic conductivity on the neuronal activation produced by subdural cortical stimulation. We found that the anisotropic model showed that neurons were activated in the deeper bank (along the sulcus) during cathodal stimulation and in the wider crown (top of gyrus) during anodal stimulation when compared to the isotropic model. Furthermore, excitation thresholds varied with anisotropic principles, especially with anodal stimulation.

1.4.3 A multi-scale computational model of the effects of TMS on motor cortex

The detailed biophysical mechanisms through which transcranial magnetic stimulation activates cortical

circuits are still not fully understood. In Chapter 4, we present a multi-scale computational model to describe and explain the activation of different cell types in motor cortex due to transcranial magnetic stimulation. It determines precise electric fields based on an individual head model derived from magnetic resonance imaging and calculates how these electric fields activate morphologically detailed models of different neuron types. We predict detailed neural activation patterns for different coil orientations consistent with experimental findings. Beyond this, the model allows us to predict activation thresholds for individual neurons and precise initiation sites of individual action potentials on the neurons' complex morphologies.

1.4.4 Effect of a Transcranial Channel as a Skull/Brain Interface in High-Definition Transcranial Direct Current Stimulation—A Computational Study

In Chapter 5, we proposed the semi-invasive approaches, which is a transcranial channel. The transcranial channel is composed of a biocompatible and highly conductive material that helps convey the current induced by transcranial direct current stimulation to the target area. However, it has only been proposed conceptually, and there has been yet to be concrete study of its efficacy. Thus, we conducted a computational investigation of this conceptual transcranial model with high-definition transcranial direct current stimulation that induces focalized neuromodulation to determine whether inclusion of a transcranial channel performed effectively. We found that the inclusion of a transcranial channel induced polarization at the target area 11 times more than did the conventional HD-tDCS without the transcranial channel.

II. Effect of Anatomically Realistic Full-Head Model on Activation of Cortical Neurons in Subdural Cortical Stimulation—A Computational Study

2.1 Introduction

Incorporating compartmental neuronal models into the complex head model was challenging, as it incurred huge computational costs. Even building the model may take a significant amount of manual work and require various imaging resources^{41,48}. Hence, it would be useful to know how significantly the anatomically realistic head model improves the estimation of cellular mechanisms, despite the complex and large computation processes required. Several studies have examined the effects of different volume conductor models on the EF/CD induced during transcranial magnetic stimulation⁴⁸, deep brain stimulation⁹⁵, and SuCS⁸⁰. They reported that there were substantial differences between the simplified partial head model and the realistic full head model. However, these effects were inferred from stimulus-induced EF/CD as the stimulus-induced neuronal responses have not yet been investigated.

In this regard, by comparison to the simplified partial-head model, the effects on activation of cortical neurons were investigated in the anatomically realistic head model by incorporating layer 5 pyramidal neuronal models, and our group presented the results at EMBC 2013⁹⁶. In our preliminary work, we modeled a small number of neurons, adjusted their locations manually, and then investigated the neuronal activation over the stimulus polarities in these head models. This study was limited because it did not consider anisotropic conductivity properly in the anatomically realistic head model, and it was simulated with too few neurons to represent the precentral gyrus. For these reasons, in this work, we constructed an anatomically realistic head model with anisotropic conductivity acquired from diffusion tensor (DT) imaging and a large number of neurons that represented two kinds of pyramidal neuronal models (layers 3 and 5). Those pyramidal neurons were then distributed uniformly within the two head models in order to compare their neuronal activation. Activation of neuronal models was observed with the three stimulus polarities of anodal, cathodal, and bipolar stimulation. In addition, excitation thresholds that represent the stimulus amplitude needed to trigger a neuron's action potential and the site of that action potential initiation were analyzed. Thus, our focus on the discrepancies between the two common head models was designed primarily to

determine whether or not the anatomically realistic head model yielded better estimation of cortical neuronal activation, which is not yet understood clearly. For this reason, this work may be considered an extended version of our conference article⁹⁶.

2.2 Methods

2.2.1 Two head models of subdural cortical stimulation

Two volume conduction head models for SuCS (a simplified partial head and an anatomically realistic full head), including stimulus electrodes, were developed to investigate the effects of head model geometry on the activation of cortical neurons. First, we constructed the simplified partial head model (extruded slab), which has a uniform brain geometry along the z-axis and an intrinsic two-dimensional geometry, as illustrated in Figure 2.1. Details were described previously⁹⁶. The dimensions of the precentral gyrus (8.5 mm) as reduced in the present model to more closely match the dimensions of the precentral gyrus in the anatomically realistic head model. This model is restricted to the precentral gyrus and its surrounding sulci and gyri. Two covered, disc-type electrodes, 13 mm apart, were placed on the cortex parallel to the precentral gyrus. These electrodes were designed by considering the clinical use of strip-type electrodes and the ease of modeling the electrodes in the anatomically realistic head model³⁸. In a clinical situation, a pulse generator (reference electrode) would be implanted in the pectoral region; however, that was not a possible consideration in this model. It was assumed that all boundaries, except the upper boundary of the skull that was set as an electric insulator, are grounded during monopolar stimulation (anodal or cathodal), as shown in Figure 2.1 (c and d).

The second model is the anatomically realistic head model obtained from MRI data (Figure 2.2). A whole upper body from the Visible Human Project of Korea⁹⁷ and the brain MRI of one living human were obtained from the SimNIBS⁴¹. We note that this human MRI data is anonymous and publicly accessible. For this reason, this study did not require Institutional Review Board (IRB) approval from the Gwangju Institute of Science and Technology (GIST).

The anatomically realistic full head model was constructed using well-known tools: FreeSurfer^{98,99},

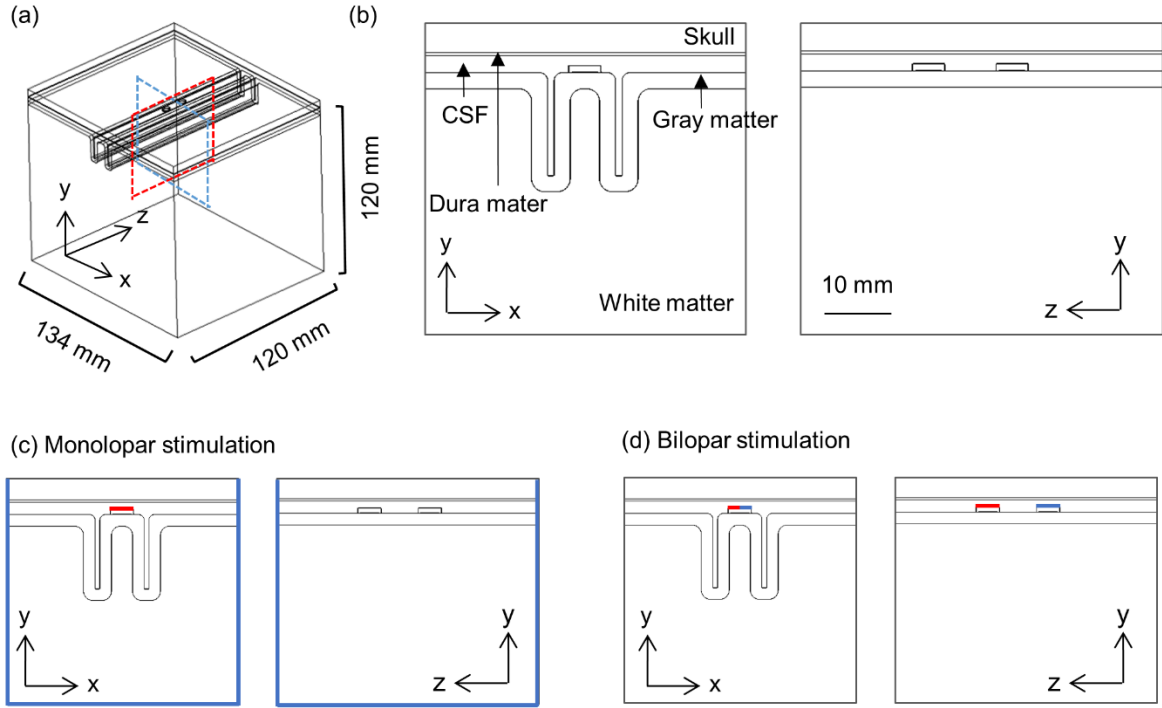


Figure 2.1 The shape of the extruded slab model. (a) Three-dimensional extruded slab model representing motor cortex, and (b) a cross-section of the model passing through electrodes. The boundary condition for monopolar (c) and bipolar (d) stimulation are illustrated; we apply the active current at red colored boundary and the ground is indicated by blue line.

FMRIB FSL⁹⁹, and Seg3D¹⁰⁰ (refer to Kim et al.⁸⁰ for details). Then, two electrodes were designed with same configuration as those in the simplified partial head model and placed on the precentral gyrus representing the hand area (Figure 2.2(a)). One reference electrode (height = 12 mm; diameter = 11.5 mm) was attached to the chest. Finally, optimized volumetric mesh was generated using iso2mesh¹⁰¹ and TetGen¹⁰².

These 3D computational head models were implemented in COMSOL Multiphysics (v4.3b, COMSOL, Inc., Burlington, MA, USA) and solved using the finite element method (FEM). The number of total tetrahedral elements in the simplified partial and anatomically realistic head models was approximately 1.2 million and 8.8 million, respectively. The bi-conjugate gradient method (a relative tolerance of 1×10^{-6}) with preconditioning of an algebraic multigrid was applied.

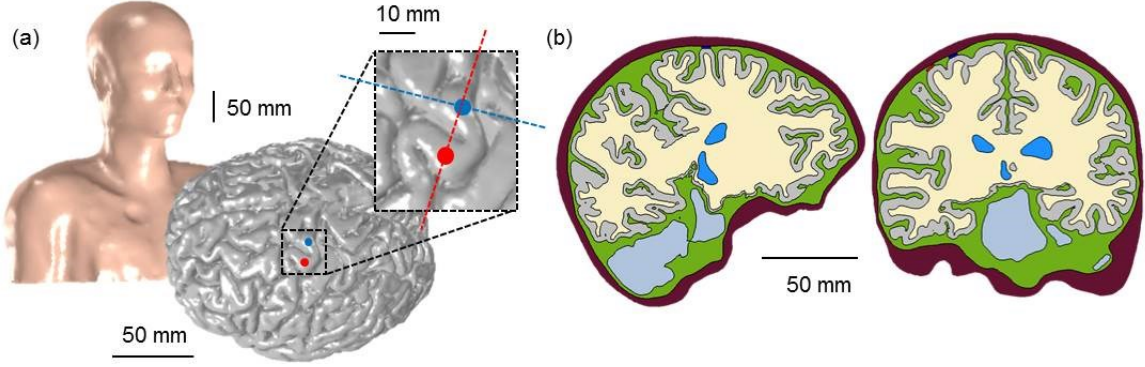


Figure 2.2 The shape of the anatomically realistic head model. (a) The complex, whole-head model (left) and placement of subdurally implanted electrodes on the gray matter (right), and (b) the cross-section perpendicular to the top electrode (blue circle; left) and parallel (right) to the two electrodes.

2.2.2 Conductivity assignment

Anisotropic conductivity was assigned to the WM only, and other segmented layers of the head models were set to isotropic conductivity (in S/m)^{23,52,103–106}: scalp: 0.465; skull: 0.01; dura mater: 0.065; CSF: 1.65; gray matter: 0.276; electrode: 9.4×10^6 ; and substrate: 0.1×10^{-9} . For more details on the conductivity assignment, refer to Seo et al.^{58,96}. In the simplified partial head model, we assumed that the dominant direction of the fibers was perpendicular to the skull (y-axis). In contrast, in the anatomically realistic head model, the major direction of the fibers was stretched, reflecting the complex geometry of the brain. Therefore, anisotropic information was acquired from diffusion tensor magnetic resonance imaging (DT-MRI) provided by SimNIBS example dataset⁴¹ under the assumption that conductivity and diffusion tensors share the same eigenvectors¹⁰⁷.

In this work, we adopted the eigenvector from DT-MRI and set the same eigenvalues as those in the extruded slab model, such that the longitudinal direction was set to 1.1 S/m with the transverse direction at 0.13 S/m^{35,108}. The tensor representation of WM anisotropy is given by

$$\sigma = S \begin{bmatrix} \sigma^L & 0 & 0 \\ 0 & \sigma^T & 0 \\ 0 & 0 & \sigma^T \end{bmatrix} S^T,$$

where S is an orthonormal eigenvector matrix and σ^L and σ^T are conductivities in the longitudinal and

transverse directions.

2.2.3 Compartment models of pyramidal neurons

We developed two types of layer 5 (L5) and layer 3 (L3) pyramidal neuronal models because pyramidal neurons are known to be the primary activators of the corticospinal tract and may provide the main input to the direct pathway^{63,109}. Their morphology and electrical properties were taken from the cat visual cortex¹¹⁰ and then modified by lengthening them 60% in order to fit human brain geometry⁶¹.

Those neuronal models were indirectly coupled with the head models, so that electric potentials calculated in each head model were, as an extracellular stimulation, applied to neuronal models with a 100 μ s monophasic pulse. We then analyzed the threshold for direct activation and the sites of action potential initiation for the two different models by varying stimulus polarities and amplitudes. We note that the simulations for neuronal models were performed in the NEURON environment¹¹¹.

Two kinds of neuronal models were distributed uniformly within the region of interest (ROI) of $50 \times 50 \times 50 \text{ mm}^3$ with the electrodes located in the middle of each of the two models. In the extruded slab model, because of its symmetric geometry, the neuronal models were placed from the crown in the precentral gyrus to the opposite crown in the post-central gyrus along the path of the central sulcus, spaced 1 mm apart (Figure 2.3 inset). Therefore, in the transverse cross-section (xy-plane), 57 neuronal models for each layer (L5 or L3) and a total of 2,907 neuronal models each (L5 or L3) were constructed. As shown in Figure 2.3(a), the axons of L5 neurons were bent partially beyond the boundary between the GM and WM, and each soma of the L5 and L3 neuronal models was placed 0.6 mm and 1.8 mm above the boundary between the GM and WM^{61,112}. In the anatomically realistic head model, two types of L5 and L3 neuronal models were constructed with configurations equivalent to those in the extruded slab model. Due to the model's complex geometry, each neuronal model was allocated to each triangular face comprising the surface of the GM within the ROI. Therefore, a total 12,824 models for L5 and L3 neurons were modeled; the details are described in Seo et al.⁵⁸.

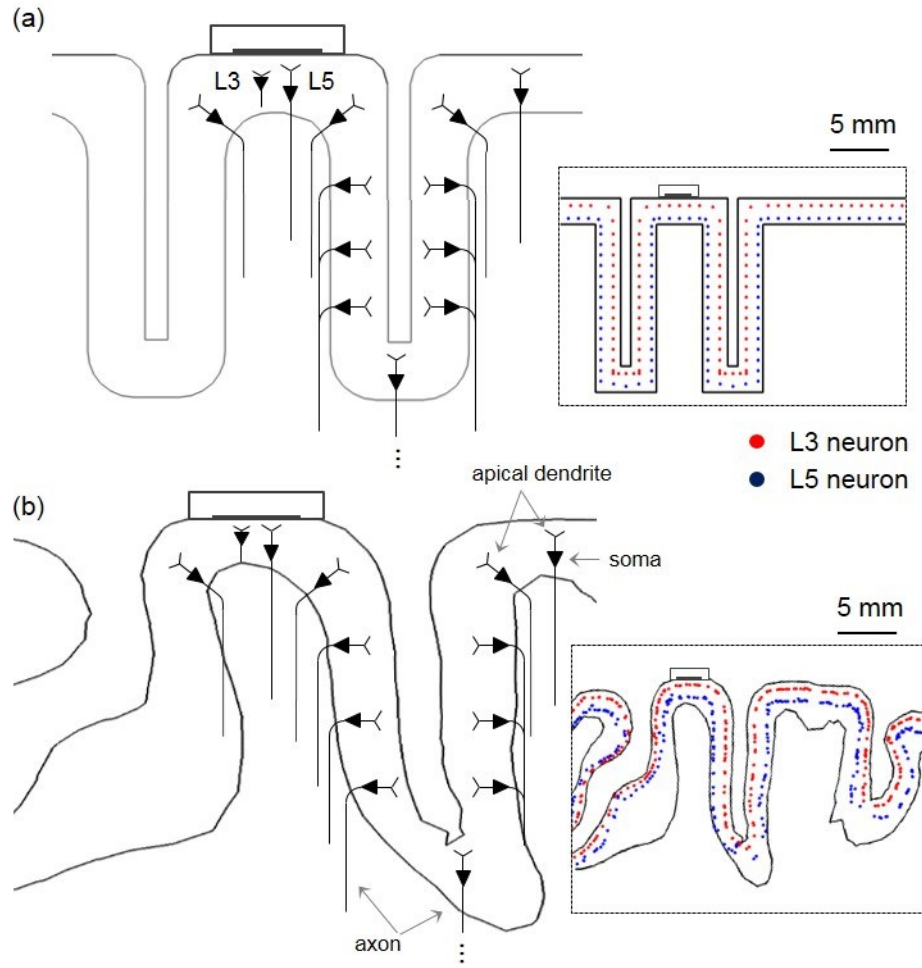


Figure 2.3 Schematic view of distribution of the compartmental pyramidal neuronal models. In the cross sections perpendicular to the electrode, neurons represent relative orientations according to their locations. However, only a few neurons among the uniform neuronal models are shown for illustrative purposes. Inset indicates the positions of L5 and L3 somata, distributed uniformly and marked as dots in (a) the extruded slab model and (b) anatomically realistic head model.

2.3 Results

To investigate the influence of head model geometry on neuronal activation, we applied a 100 μ s monophasic rectangular pulse to the motor cortex by varying stimulus polarity (anode and cathode). The excitation thresholds necessary to evoke action potential of neuronal models were then measured in both the

extruded slab and anatomically realistic head models over various stimulus amplitudes. Due to the advantages that this process held for our simulation study, we considered stimulus amplitudes up to 100 mA, which is far higher than the typical acceptable range of under 20 mA^{5-7,16,113}. In this way, it is possible to observe the trends in neuronal activations.

Figures 2.4 and 2.5 illustrate the spatial extents of the excitation thresholds in the extruded slab and anatomically realistic head models, respectively. They show similar threshold patterns and spatial extents. On the whole, during anodal stimulation, neurons in the crown beneath the electrode have generally had the lowest thresholds, while the lip to upper part of the bank and the opposite lip were excitable in L5 and L3 neurons, respectively. Cathodal stimulation activated neurons in the deeper bank compared to anodal stimulation, while bipolar stimulation seemed to be a superposition of the two monopolar stimulations: cathodal and anodal. Differences between the two models were characterized in the cathodal stimulation. In the anatomically realistic head model, the patterns of spatial extent seemed asymmetric. In both L5/L3 neurons, the bank along the central sulcus was observed to be most excitable area, while the bank along the precentral sulcus was not (Figure 2.5 (c)). An activated area with stimulus amplitude lower than 20 mA (represented by white contour lines (b) and highlighted by light yellow shaded region(c) in Figure 2.4 and Figure 2.5) was focused around even bank during cathodal stimulation in the anatomically realistic head model. However, in the extruded slab model, the crown was found to be the most excitable area regardless of stimulus polarities, and it had symmetric patterns of excitation threshold due to its inherently symmetric geometry. For further investigation, the ratio of excited neurons to total neurons was observed for three different anodal/cathodal/bipolar stimulations (Figure 2.6). When we focused on L5 neurons excited under the stimulus amplitude of 20 mA (represented by the light yellow shaded region in Figure 2.6), the extruded slab model induced a much higher percentage of excited neurons than did the anatomically realistic head model during anodal stimulation and a smaller percentage during cathodal stimulation. It did not show substantial differences in L3 neurons during cathodal stimulation. Overall, it was evident that the extruded slab model yielded notably higher percentages of excited neurons than did the realistic head model during anodal stimulation, which suggests that the extruded slab model may overestimate the stimulation effects. We observed that anodal stimulation started to excite neurons at lower stimulus amplitudes than did cathodal stimulation; however, this was reversed at high stimulus amplitudes. This behavior was observed in both

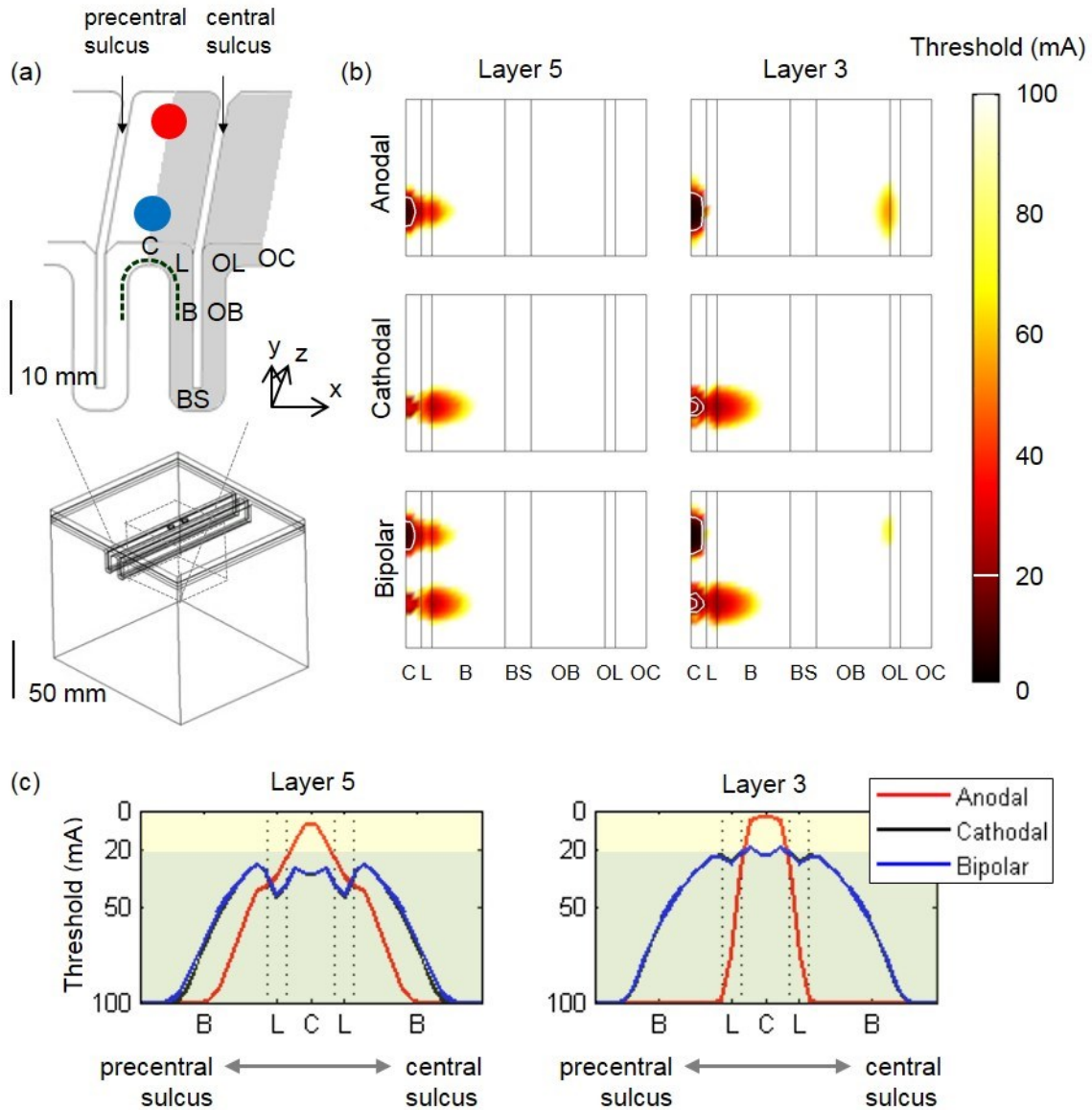


Figure 2.4 The spatial extent of the excitation thresholds in the extruded-slab model. (a) Because of symmetric geometry, neuronal models were distributed within half of the cortex, which is represented as a gray colored region; in the x-y plane, the gray matter (GM) is classified according to the cortex location and orientation. The crown (C) is the region directly under the electrode, and the lip (L) and bank (B) are located along the fold on gyrus; the bottom sulcus (BS) lies beneath the central sulcus; the postcentral gyrus consists of the opposite bank (OB), opposite lip (OL), and opposite crown (OC). (b) The spatial extent of the thresholds stretching the surface from the gray colored region in (a) in the x-direction is shown. The horizontal axis represents the abbreviation of the different region of the cortex; the white contour lines represent excitation thresholds < 20 mA. (c) Excitation thresholds along the curve (depicted as a dotted curve

in (a)) from the bank of the precentral sulcus to the bank of the central sulcus under the active electrode (blue circle).

L3/L5 neurons and both head models (over about 25 – 30 mA in L3/L5 neurons in the anatomically realistic head model; and over about 30 mA in L3 neurons and about 50 mA in L5 neurons in the extruded slab model). Overall, bipolar stimulation excited more neurons than did the others because it seemed to be a summation of cathodal and anodal stimulations.

For the given stimulus polarity and cell types (L5 or L3), we summarized the minimum excitation threshold required to evoke neuronal activity and the area where excited neurons are located, which are tabulated in Table 2.1. Consistent with previous findings from the ratio of neurons excited over varying stimulus amplitudes (Figure 2.6), we note in Table 2.1 that anodal stimulation had substantially lower thresholds than did cathodal stimulation. As shown in previous results (Figure 2.4 and Figure 2.5), bipolar stimulation was shown to be a simple summation of anodal and cathodal stimulations. Thus in bipolar stimulation, the minimum thresholds under the active electrode were identical to those of anodal stimulation, and under the ground electrode they had the same minimum thresholds to cathodal stimulation. During anodal stimulation, the minimum thresholds were increased from the crown to the bank along the fold of gyrus (the minimum thresholds in the lip and bank were 17 and 23 mA for L5 neurons, and 7 and 55 mA for L3 neurons), while during cathodal stimulation, neurons in the bank had lowest threshold and the minimum thresholds in the crown and lip were comparable (the minimum thresholds in the crown and lip were 21 mA for L5 neurons, and 14 and 15 mA for L3 neurons). It is interesting that, during cathodal stimulation, the

Table 2.1 The minimum threshold (mA) for each polarity in comparison between the extruded slab model and the anatomically realistic head model. Parentheses indicate the location of the neuron(s) excited.

Polarity	Extruded slab model		Anatomically realistic head model	
	L5 neurons	L3 neurons	L5 neurons	L3 neurons
anodal	7 (C)	3 (C)	8 (C)	3 (C)
cathodal	21 (C)	12 (C)	13 (B)	11 (B)
bipolar	7(C)	3 (C)	8(C)	3(C)

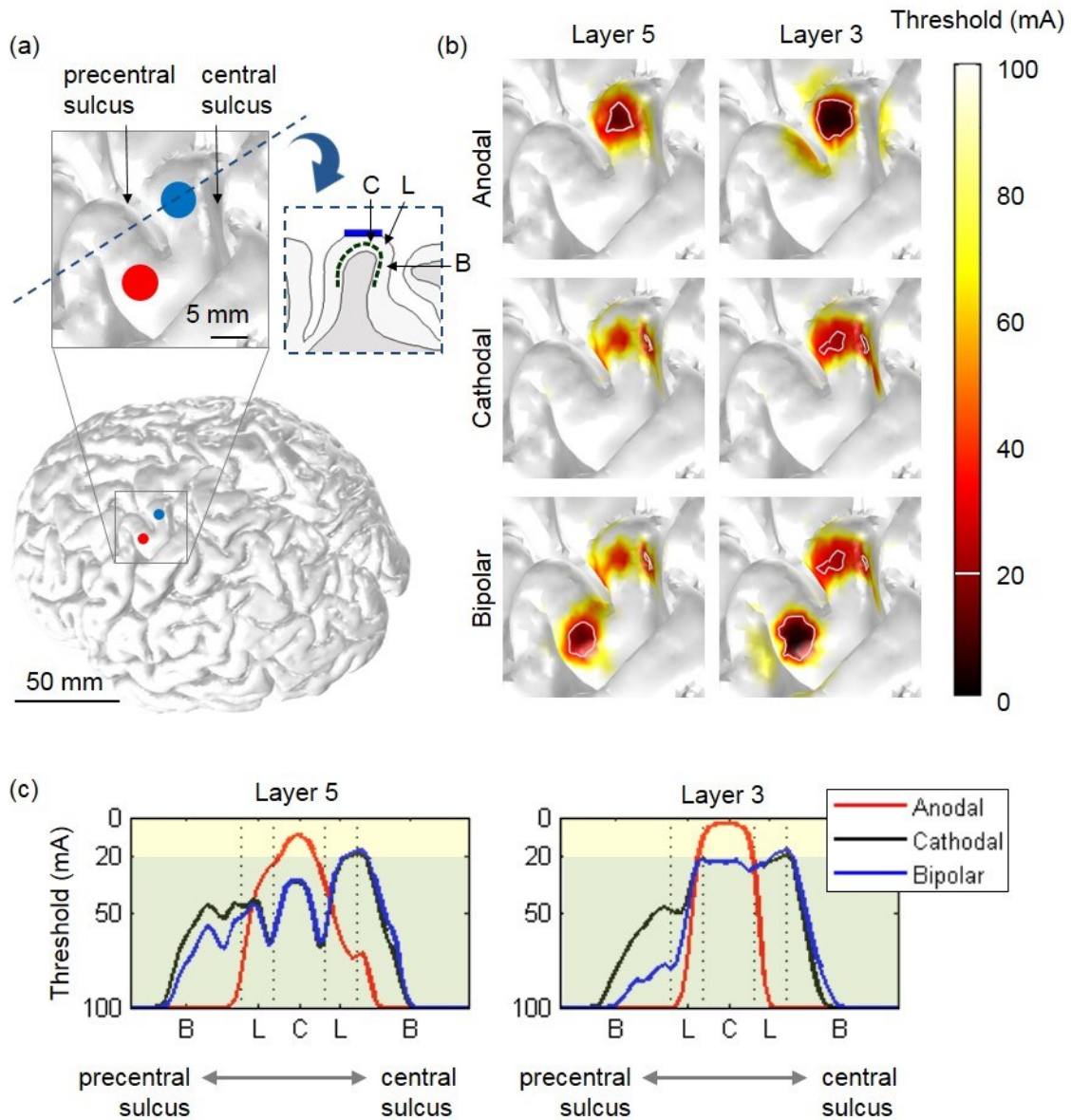


Figure 2.5 The spatial extent of the excitation thresholds projected on the cortical surface in the anatomically realistic head model. (a) Electrodes were placed on the precentral gyrus representing the hand area; the left inset represents the expansion of the GM surface and right inset indicates the cross-section perpendicular to the top electrode (following blue colored dotted line) with the cortex location of the crown (C), lip (L), and bank (B). In bipolar stimulation, the upper electrode represents the cathode (blue), while the bottom electrode is the anode (red). For convenience, monopolar stimulation was applied using only the upper electrode; (b) this is the spatial extent of the thresholds of L5 and L3 neurons in the anatomically realistic head model; the white contour lines represent excitation thresholds < 20 mA. (c) Excitation

thresholds along the curve (depicted as a dotted curve in the right inset of (a)) from the bank of the precentral sulcus to the bank of the central sulcus under the active electrode (blue circle).

minimum threshold of L5 neurons in the anatomically realistic head model was substantially lower (60%) than in the extruded slab model. In the extruded slab model, neurons excited at the lowest threshold were located uniformly on the crown, regardless of polarities, while in the anatomically realistic head model, cathodal stimulation activated the bank at 11 mA (L3 neurons) or 13 mA (L5 neurons), which are the minimum excitation thresholds.

The site of initiation of the action potential evoked by extracellular stimulation was examined by recording membrane potentials at several different locations on L5 and L3 neurons (Figure 2.7). We observed the initiation sites of L5/L3 neurons that evoked action potentials under the 100 mA stimulus amplitude and found that they varied according to the neuronal model's location, morphology, and stimulus polarities. The axon terminal was frequently excited in L3 neurons, which may be due to the finite length of L3 neurons within gray matter (GM). The axon at the boundary between GM and white matter (WM)—where conductivity changes abruptly—was often observed as the initiation site for L5 neurons. Cathodal stimulation evoked the excitation of L3 neurons on the crown (perpendicular to the electrode) at the initial segment, while anodal stimulation evoked L3 neurons at the axon terminal. However, L5 neurons on the crown were

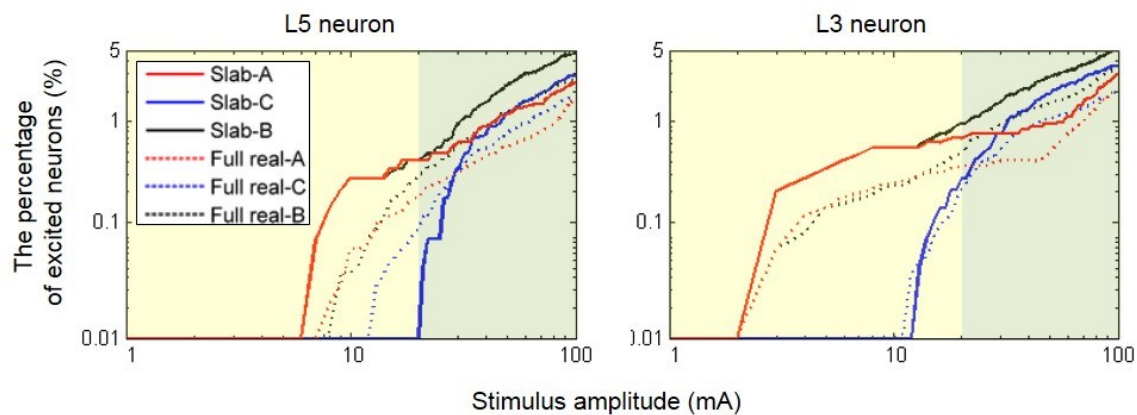


Figure 2.6 The relative ratio (%) of neurons excited with three different polarities: (anodal (A); cathodal (C), and bipolar (B) stimulations). Layer 5 (L5) and layer 3 (L3) pyramidal neurons are compared within the extruded slab model (slab) and anatomically realistic head model (full real); neurons that evoke action potentials within 20 mA are highlighted in light yellow.

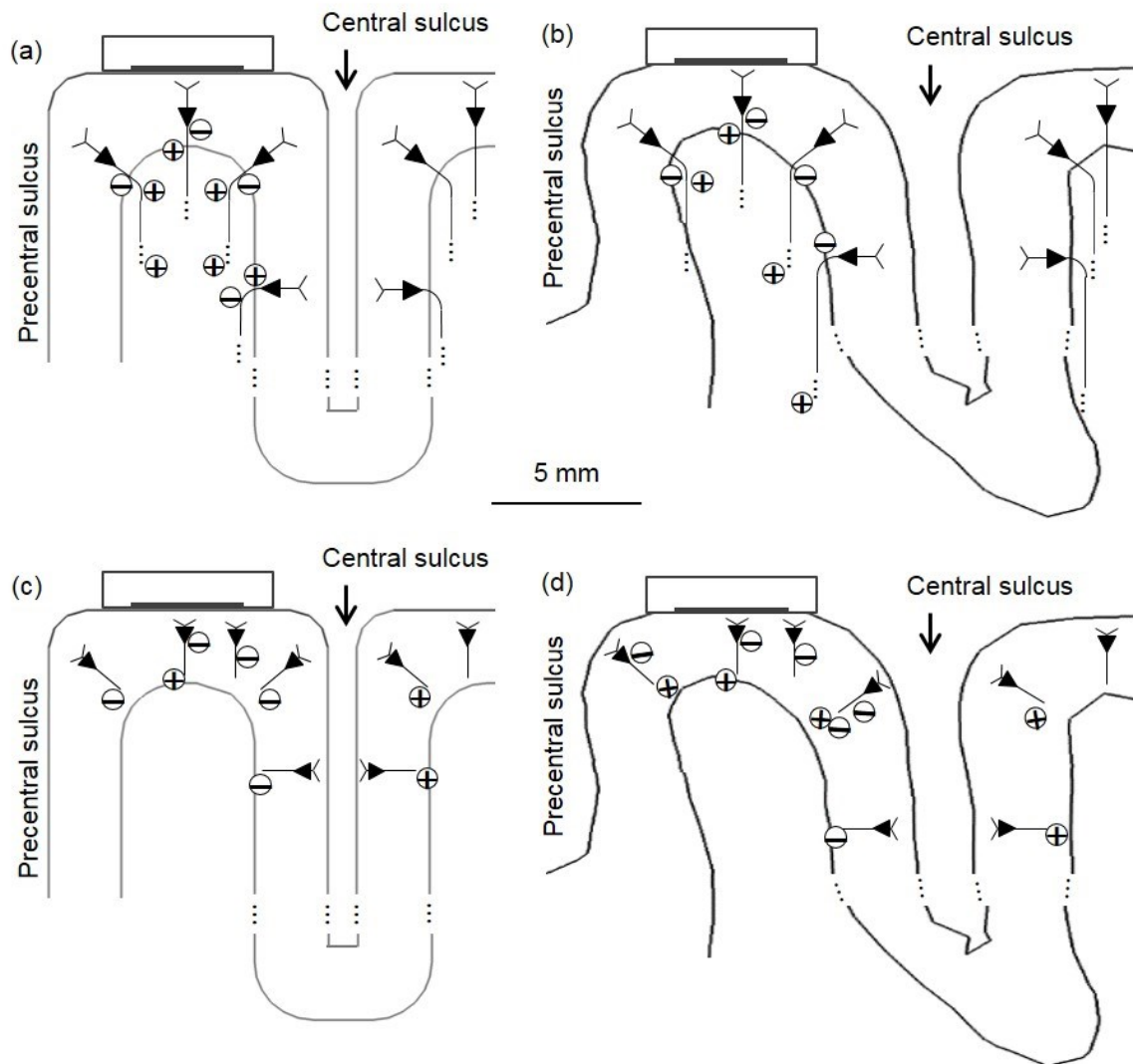


Figure 2.7 Initiation site of action potential over anodal (+) and cathodal (-) stimulation. (a) L5 neurons and (c) L3 neurons in the extruded slab model; (b) L5 neurons and (d) L3 neurons in the anatomically realistic head model.

evoked at the boundary between GM and WM for both anodal and cathodal stimulations. In the lip and the bank following the fold of the gyrus, the initiation site for L5 neurons in the anatomically realistic head model was the axon terminal during anodal stimulation and the boundary between GM and WM during cathodal stimulation. In the extruded slab model, neurons in both the lip and the bank showed inconsistent initiation sites.

The major differences between the two head models were likely due to the asymmetric geometry of

the anatomically realistic head model; differences were observed around the lip, in particular. During anodal stimulation, initiation sites of L5 neurons at the lip were located at the bends in the axons on the side of the precentral sulcus, as well as at the axon terminals in the direction of the central sulcus. These asymmetric initiation sites were also observed around the lip in L3 neurons.

2.4 Discussion

Computational brain modeling could be a prerequisite in determining the optimal parameters necessary to design efficient electrotherapy treatments^{17,19}. Thus far, many computational studies have been extrapolated cellular targets of electrical stimulation by stimulus-induced electric fields. For precise patterns of electric fields, the importance of the anatomically realistic head model has emerged for individualized modelling according to each subject by incorporating magnetic resonance imaging (MRI) and diffusion tensor MRI (DT-MRI); it has also been investigated actively by noninvasive electrical stimulation^{19,21,23,37,40,41,50}. Edward et al. constructed three different head models using each subject MRI and then validated a computational model for estimating the stimulus-induced electric field in human transcranial stimulation²¹. They revealed that the model data were consistent with the motor responses across subjects. Furthermore, operating under the assumption that induced electric field is comparable to cortical activation, they found that the model predicted a significant difference (more than twofold) in the induced electric field on the primary motor cortex across subjects. The computation study of Truong et al. reports the comparable variation across subjects and describes the importance of the construction of an individualized anatomically realistic head model⁵⁰; however, only a few studies of invasive electrical stimulation have been performed using the anatomically realistic head model^{38,80,96}. It is understood that invasive stimulation may stimulate a relatively smaller focal area of the brain than noninvasive stimulation; thus, the use of a more complex head model representing the whole brain area may actually be relatively less demanding.

In general, the degree of activation can be approximated by employing the stimulus-induced electric field or current density. In particular, the electric field is known to relate directly to neuronal activation under the quasiuniform assumption¹⁹. Another way to estimate the extent of neuronal activation is to compute the second derivative of the potential along the direction of the neurons (directional derivative) which is known

as the activating function⁹². However, these methods may be less accurate in estimating neuronal activation because neuronal morphologies and their electrical properties are not fully considered.

The activating function shows a simple reversal in signs between anodal and cathodal stimulations because the brain model is linear with respect to electric potential. Due to such limitations of simple extrapolations, a compartmental neuronal model is incorporated into computational brain models in order to yield more accurate estimations of neuronal activation^{52,53,61,63}. However, in previous studies, the compartmental neuronal models were coupled with the extruded slab model, which is a very simplified and less accurate model that may lead to inaccurate estimations of neuronal activation due to a modeling error.

The insertion of electrodes into the anatomically realistic head model is difficult in terms of generating the computational mesh due to irregular brain tissue morphologies. In this work, the insertion of electrodes into the realistic head model was attempted and an anatomically realistic head model was eventually constructed. We then incorporated numerous numbers of compartmental models of L5/L3 pyramidal neurons combined with the anatomically realistic head model, enabling us to directly investigate the effects of head model mismatch. In this work, this model mismatch was analyzed in terms of four distinct aspects: 1) spatial extent of threshold, 2) the percentage of excited neurons, 3) the minimum threshold, and 4) initiation site of action potentials.

First, in the spatial extent of excitation thresholds, asymmetric patterns in the anatomically realistic head model were observed compared to the simplified extruded slab model. Specifically, during cathodal stimulation, L5 neurons in the bank close to the central sulcus were activated more than the L5 neurons in the precentral sulcus, although this is not illustrated clearly in Figure 2.5. The bank along the central sulcus is known to be the anatomical location of the motor area of the hand¹¹⁴, which is the most critical target area of invasive stimulation⁶. As a result, it is believed that the anatomically realistic head model may estimate cellular targets more accurately than the extruded slab model.

Second, regarding the percentage of excited neurons, the extruded slab model induced more depolarization (a higher ratio of excited neurons) during anodal stimulation and more hyperpolarization (a lower ratio of excited neurons) during cathodal than did the anatomically realistic head model. This result was expected based on our earlier study⁸⁰, where we reported the current distribution difference in SuCS between the realistic head model and the extruded slab model. The extruded slab model was more likely to

overestimate neuronal activation in SuCS than was the anatomically realistic head model. However, this work may be the first report that, at the neuron level, the activation effects of cortical neurons in the extruded slab model may be relatively overestimated compared to the anatomically realistic head model.

Third, regarding the minimum threshold, the model discrepancy was notable during cathodal stimulation. The crown was the area where the top of gyrus was activated most easily in the extruded slab model, while the bank was activated well in the anatomically realistic head model. In addition, regarding the initiation site of action potentials, the two head models yielded similar behaviors on initiation sites, except for in the lip and in the bank. This discrepancy may come from asymmetry in the anatomically realistic head model.

We observed that differences in the head models yielded variations in excitation thresholds; the distinctions were more notable in L5 neurons than in L3 neurons. We understand that L5 neurons are affected significantly by the geometry of the brain model because of its longer axon that extends into the WM, while L3 neurons are located within the GM.

The simulated pyramidal neuronal responses showed an agreement with the empirical findings from previous research. Gorman reports that, at the threshold of stimulus amplitude necessary to elicit neuronal responses, a direct wave was elicited during anodal stimulation, while cathodal stimulation produced an indirect response¹⁰⁹. As stimulus amplitude increased up to supramaximal intensity, cathodal stimulation produced a greater response in the direct and indirect activations than anodal stimulation. In this work, we investigated the individual neuronal models which enabled us to observe the direct response. At the stimulus amplitude where anodal stimulation evoked action potentials of L5 and L3 neurons, cathodal stimulation did not excite any neurons (Figure 2.6). Interestingly, there were points of intersection between anodal and cathodal stimulations that were about 25-30 mA in the anatomically realistic head model and about 30 or 50 mA in the extruded slab model; at a higher stimulus amplitude than those points, cathodal stimulation produced a higher percentage of excited neurons than did anodal stimulation.

The minimum excitation thresholds (Table 2.1) are in accordance with previous results that show anodal stimulation activated neurons at lower stimulus amplitudes than did cathodal stimulation^{3,52,53,61,109,115,116}. Bipolar stimulation appeared to be a superposition of anodal and cathodal stimulations, as shown in Figure 2.4, Figure 2.5 and Table 2.1. This is consistent with the results of previous

computational studies^{3,52,53,61,63}, which report that bipolar stimulation with an inter-electrode distance greater than 10 mm produces little interference. In this work, inter-electrode distances are greater than 10 mm in both head models.

Initiation sites of action potential varied according to the position of the neuronal models, stimulation polarity, and relative direction of the stimulus-induced electric field^{61,93}. According to our computational study, L3 neurons were initiated easily at the axon terminal, while the action potential of L5 neurons was initiated frequently at the boundary between the GM and WM, where conductivity changes abruptly¹¹⁷. Furthermore, we observed that during cathodal stimulation, initiation sites were pinpointed more in areas closer to soma than were those produced by anodal stimulation; these findings are relevant to existing studies^{52,53,61,63,118} which report the longer latency in cathodal stimulation compared to anodal stimulation in experimental studies and investigate the stimulation effects on invasive approaches in computational studies.

In this work, the neuronal model was based on properties from the cat visual cortex due to limited knowledge about properties and morphologies of most human cortical neurons. Despite this uncertainty in the neuronal models, it was observed that the computational results were quite reasonably consistent with experimental data. The compartmental models of pyramidal neurons used in this work were incorporated also on several computational studies to investigate stimulation effects. Wongsarnpigoon et al. studied the effects of electrode position and geometry on neuronal activation in the epidural cortical stimulation⁶¹. Prior to the computational study, they validated compartmental pyramidal neuronal models located in the crown by comparing with these models with experimental data. Kamitani et al. constructed neocortical neuronal models in TMS and showed brief firing followed by a silent period of duration, which was comparable to experimental data of TMS⁵¹. Thus, these studies provide a valid rationale of computational results that well match those in this study.

It is challenging to make direct comparisons between the extruded slab model and anatomically realistic head model; however, as both models are the most commonly used in invasive CS studies, we analyzed the responses of neuronal models induced by differences in the head models and then observed the discrepancy in those neuronal responses. Grant and Lowery proposed an ellipsoid-shaped realistic head model that sets the ground on the bottom, where the reference electrode can be located⁹⁵. This ellipsoid realistic head model was compared with a cubit model that set the ground at all exterior boundaries. They

found that electrical grounding and the finite conducting volume of the head had considerable effects on the electrical potential, electrical field, and activating function. This may imply that the effects of different head models may be due to the grounding effect. In this regard, we investigated grounding effects under a more extended extruded slab model and set the reference electrode on the bottom. This model was proposed by⁶³ and considers boundary conditions based on a realistic head model⁹⁵. Then, we compared two kinds of extruded slab models during monopolar stimulation and found that the two models had comparable excitation thresholds, with an average 2.33% difference.

Other critical model parameters that may have a significant impact on any discrepancy between the extruded slab and anatomically realistic head models include the model anisotropy of conductivity and geometry. First, we investigated whether or not anisotropic conductivity has a significant effect on cellular targets. Two computational head models were set to isotropic conductivity (WM conductivity was assigned to 0.126 S/m³⁷), and then stimulation changes induced by tissue anisotropy to the equivalent isotropic model were assessed. The anisotropic models yielded substantially different results compared to the isotropic models. As tabulated in Table 2.1, during anodal stimulation, the minimum thresholds were 3 mA in the anatomically realistic head model and 7 mA in the extruded slab model; cathodal stimulation had a much higher value of the minimum threshold compared to anodal stimulation. In contrast to the results from anisotropic models, results of the model being set to the isotropic conductivity showed minimum thresholds were much higher during anodal stimulation than during cathodal stimulation. The minimum thresholds in the extruded slab model were 23 mA and 15 mA in anodal and cathodal stimulations, respectively. In the anatomically realistic head model, they were 19 mA and 7 mA, respectively. Interestingly, these results from isotropic models were irrelevant to the experimental ones that showed anodal stimulation activated neurons at lower stimulus amplitude than did cathodal stimulation^{3,109,115,116}. Furthermore, isotropic models excited far more neurons during anodal stimulation and fewer neurons during cathodal stimulation compared to the anisotropic model⁵⁸. As a result, we concluded that anisotropy of conductivity, as well as the complexity of head model geometry, are major factors that produce the discrepancies between the extruded slab and anatomically realistic head models.

The positions of the L5/L3 neurons may influence our computational results. In order to estimate these effects on neuronal activation, we slightly disposed the neuronal models; positions of L3/L5 neurons were

shifted upward or downward by 1 mm in the perpendicular direction to the cortical surface. We observed that L5 neurons, which are activated under 100 mA, showed an average of 6.36% differences and L3 neurons had an average of 7.3% differences during monopolar stimulations. In addition, in order to briefly investigate the effect of neuron orientation, we rotated it up to 90 degrees in increments of 30 degrees, since the morphology of dendrites is not symmetric. Slight change was observed, with a maximum of 2.8% differences in both L5 and L3 neurons according to the rotation of the dendrites. These investigations showed that the positions of neurons had mild effects on neuronal activations; however, spatial extent of thresholds, minimum threshold, or patterns of percentage of excited neurons were not substantially varied.

Through this computational study, we revealed that the anatomically realistic head model may be recommended as an effective, beneficial model used to investigate cellular targets and detailed neuronal responses. This recommendation comes despite the fact that relatively smaller and more focalized areas may be involved in the investigations as well as construction of the realistic head model requires substantial efforts. The increased effort might be due to incorporating precise information of model anatomy and anisotropic conductivity acquired from MRI and DT-MRI. For further study, we plan to model communicating populations of neurons and generate indirect responses following synaptic excitations. It is expected that the advantages of the anatomically realistic head model will be more considerable in this further study because of the larger area that may be involved in neuronal excitation.

We know that a target-neural element is necessary to improve clinical results, and it is believed that targeted neural elements may vary according to electrode positions, geometry, and polarities⁶¹. For example, the analgesic effect of motor cortex stimulation is related to the specific neurons excited in the superficial cortical layer and not to the intensity of the stimulus⁴. In the same context, effects are also related to electrode locations: electrodes placed perpendicular to the precentral gyrus were recommended in order to improve therapeutic effects^{3,4}, while other studies have demonstrated improved outcomes with electrodes oriented parallel to the precentral gyrus¹. In our work, we demonstrated that the anatomically realistic head model is more useful in investigating the target area and detailed responses of neuronal activation. Further studies should focus on parametric analyses using the anatomically realistic head model rather than the extruded slab model.

III. Computational Study of Subdural Cortical Stimulation: Effects of Simulating Anisotropic Conductivity on Activation of Cortical Neurons

3.1 Introduction

To improve the spatial accuracy of stimulation a realistic head model has been used widely, because magnetic resonance (MR) images can be used to reflect brain anatomy^{21,23,37–50}. These studies have incorporated the anisotropic conductivity derived from diffusion tensor (DT) imaging into their head models^{40–46} and have shown variation in the spatial patterns and strength of induced EF/CD, as well as alteration of current flow in directions parallel to the white matter (WM) fiber tract according to the inclusion of anisotropy. However, most investigations using anisotropic conductivity with realistic head models have focused on noninvasive approaches, while invasive studies are rare. The most recent study examined the effects of SuCS on anisotropic conductivity using a realistic head model⁸⁰, but this investigation using a realistic head model was limited to macroscopic or mesoscopic estimations of EF/CD in the cortex, rather than microscopic estimations at the neuronal level.

The simple quantification of EF or CD is insufficient to explain complex neuronal modulation, because responses of cortical neurons vary depending on their shape, size, location, and orientation^{56,61,119}. For a detailed investigation at the neuronal level, compartmental cortical neuronal models coupled with the head model are required. However, due to the complex brain geometry of the realistic head model, those neuronal models are usually combined with a simplified head model (extruded slab model). The simplified extruded slab model represents the typical precentral gyrus region and this simple geometry makes it easy to couple neuronal and brain models in a straightforward manner. However, due to possible modeling error (anatomical mismatch of the volume conduction model of simplified and real head models), this method is expected to produce non-negligible discrepancies between computational and empirical (ground truth) electric fields, which can be a crucial factor in determining whether or not neuronal activation takes place^{23,41,77}. In a recent study, the effects of transcranial direct current stimulation (tDCS) on cortical neurons were assessed using a realistic head model⁵⁶, in which neuronal activation was investigated under the assumption that tDCS produces uniform electric fields in gray matter (GM); thus, complex brain geometry

effects have not been considered directly in neuronal models.

To the best of our knowledge, the computational study of SuCS using an anatomically realistic head model has not been investigated at the neuronal level. In response to this need, the significance of neuronal activation by a realistic electric field produced by SuCS was reported by our group at the EMBC 2013⁹⁶; in preliminary work, small numbers of neurons in the computational domains were considered concisely for comparison between the simplified extruded slab model and realistic head model. However, this study did not consider anisotropic conductivity in the WM properly and the number of neurons was too small to represent the typical neurons in the brain cortex. For these reasons, in this work, we constructed an anatomically realistic full head model with anisotropic conductivity acquired from DTI and a large number of neuronal models. Two types of layer 3 and layer 5 pyramidal neuronal models were developed for uniform distribution around the precentral gyrus.

Our goal was to investigate the effect of anisotropic conductivity on neuronal activation produced by SuCS using the anatomically realistic head model with three types of stimulation polarities (cathodal, anodal, and bipolar). Their influence was explored by quantitative estimation of excitation thresholds that evoke neuron activation, as well as the percentage of neurons excited and the minimum threshold.

3.2 Methods

3.2.1 Construction of the anatomically realistic head model

A volume conduction model of the human head, including stimulus electrodes, was developed using a brain and whole human body MRI acquired from SimNIBS⁴¹ and the visible human project of Korea⁹⁷ (Figure 3.1). We note that these human MRI data are anonymized, de-identified, and are publicly accessible. For this reason, the institutional review board (IRB) approval of Gwangju Institute of Science and Technology (GIST) was not required for this study. We segmented WM, GM and the cerebellum based on FreeSurfer^{98,120}, and used FMRIB FSL⁹⁹ to extract CSF, ventricles, skull and scalp. The shape of the upper

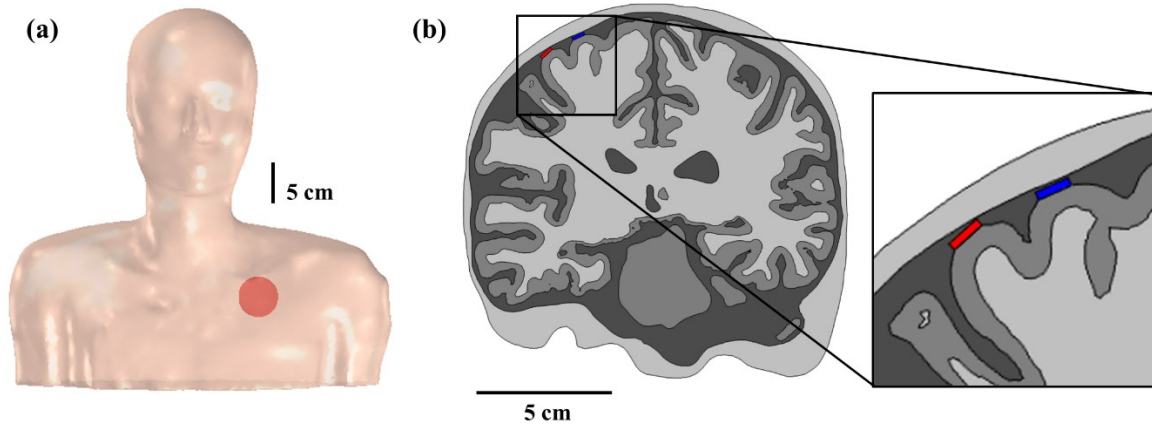


Figure 3.1 The shape of the anatomically realistic head model. (a) Whole head model with reference electrode (red circle) and (b) cross-section of head model for subdural cortical stimulation are shown. Red and blue dots on the cortex represent implanted electrodes.

body was extracted using Seg3D¹⁰⁰. Before creating tetrahedral finite element meshes from surface meshes, we attached two electrodes to the precentral gyrus representing the hand area¹¹⁴. We designed two disc-typed electrodes (height = 0.1 mm; diameter = 4 mm) to be covered with substrates (height = 1.1 mm; diameter = 5 mm), and these two electrodes were implanted subdurally 13 mm apart. The substrate was constructed by considering the clinical use of strip-type electrodes, but we limited the substrate to surround a disc-type electrode because of the difficulty of modeling strip-type electrodes in the brain³⁸. Then, we considered upper electrode (blue in Figure 3.1(b)) only as an active electrode for monopolar stimulation (anodal or cathodal); upper electrode as a cathode and bottom electrode (red in Figure 3.1(b)) as an anode were considered for bipolar stimulation. In a clinical situation, a pulse generator is implanted in the pectoral region; thus, a disc-type reference electrode (height = 12 mm; diameter = 11.5 mm) was modeled on the chest. Finally, we generated optimized volumetric mesh using iso2mesh¹⁰¹ and tetgen¹⁰².

These 3D computational models were input in COMSOL Multiphysics (v4.3b, COMSOL, Inc., Burlington, MA, USA) and solved numerically by the finite element method. The number of total tetrahedral mesh elements was 8.8 million. Smaller elements were used primarily around the cortex near electrodes and then they became larger toward the chest area. The bi-conjugate gradient method (a relative tolerance of 1×10^{-6}) with preconditioning of an algebraic multigrid was used as a solver.

3.2.2 Conductivity assignment

Anisotropic conductivity assigned to the WM was constructed in the anatomically realistic head model. Except for WM, all other tissue types were modeled as isotropic. The conductivities for each layer, which were obtained from the literature^{35,37,52,108}, are tabulated in Table 3.1.

In the anatomically realistic head model, it was difficult to determine the major anisotropic direction of WM, because fibers were distributed in a complex manner due to the complexity of brain geometry. Accordingly, we derived an electrical conductivity tensor of WM for the anatomically realistic head model from the water diffusion, as measured by diffusion tensor magnetic resonance imaging (DT-MRI), assuming that conductivity and diffusion tensors share the same eigenvectors¹⁰⁷. In this case, we shared only eigenvectors tensor provided by SimNIBS example dataset⁴¹ and then set the eigenvalue along the largest and perpendicular eigenvectors in three ways. First we used artificial anisotropy with a fixed value (fixed value

Table 3.1 Conductivities of tissues and electrodes.

Compartment	Conductivity (S/m)
Substrate conductivity	0.1×10^{-9}
Electrode conductivity	9.4×10^6
Scalp	0.465
Skull	0.01
Dura mater	0.065
CSF	1.65
Gray matter	0.276
White matter (isotropic)	0.126
White matter (parallel to fibers)	1.1
White matter (perpendicular to fibers)	0.13

anisotropy). We set the eigenvalue along the largest eigenvector (σ^{long} , longitudinal direction) as 1.1 S/m, and the perpendicular eigenvectors (σ^{trans} , transverse direction) as 0.13 S/m, as were shown in Table 3.1. Next, we modeled the conductivity tensor σ of the WM as follows:

$$\sigma = S \text{ diag}(\sigma^{\text{long}}, \sigma^{\text{trans}}, \sigma^{\text{trans}}) S^T \quad (1)$$

where S is the orthogonal matrix consisting of unit length eigenvectors of the diffusion tensor.

In addition to obtaining a more generalized conductivity tensor, we used a direct transformation approach with volume normalization (volume normalization anisotropy) and artificial anisotropy with volume constraint (volume constraint anisotropy)^{121,122}.

The volume normalization anisotropy maintains the mean conductivity of the tensors at the isotropic WM value (σ^{iso}). It calculates normalized eigenvalues σ'_{v_i} as

$$\sigma'_{v_i} = \sigma_{v_i} \frac{\sigma^{\text{iso}}}{\sqrt[3]{\sigma_{v_1}\sigma_{v_2}\sigma_{v_3}}} \quad (2)$$

where σ_{v_i} is the conductivity tensor eigenvalue of the DTI data.

The volume constraint anisotropy fixed the artificial anisotropy ratio to the eigenvalues by calculating

$$\sigma^{\text{long}} = \sqrt[3]{(\sigma^{\text{iso}})^3 r^2} \quad (3)$$

$$\sigma^{\text{trans}} = \sqrt[3]{(\sigma^{\text{iso}})^3 / r} \quad (4)$$

where r is the anisotropic factor ($r=2$ if 2:1, $r=5$ if 5:1, and so on). We varied the anisotropic factor from 2, 5, and 10 to 100; the conductivity values are tabulated in Table 3.2.

Table 3.2 Longitudinal and transverse conductivity of WM tensor elements calculated using the artificial anisotropy with volume constraint according to anisotropic factors. (r).

	$r=2$	$r=5$	$r=10$	$r=100$
σ^{long}	0.200	0.368	0.585	2.714
σ^{trans}	0.100	0.074	0.059	0.027

3.2.3 Compartment models of pyramidal neurons

In this work, layer 5 (L5) and layer 3 (L3) pyramidal neuronal models were constructed. We used the detailed morphology and electrical properties from the cat visual cortex¹¹⁰ and lengthened the neuronal models by 60% to fit human brain geometry⁶¹. Briefly, low density Na⁺ channels were present in the soma and dendrites, and high density channels were present in the axon hillock and initial segment. The axon and soma included fast K⁺ channels, while dendrites did not. Slow K⁺ channels and high-threshold Ca²⁺ channels were present in both soma and dendrites. Simulations were performed in the NEURON environment¹¹¹.

Due to the complexity and limitations of computational resources, such neurons could not be constructed explicitly in the 3D computational models. Thus, two kinds of L5 and L3 neuronal models were positioned virtually in the anatomically realistic head model. We computed the fields of stimulus-induced potentials distributed in the head model, and then the electric potentials were applied to each compartment of

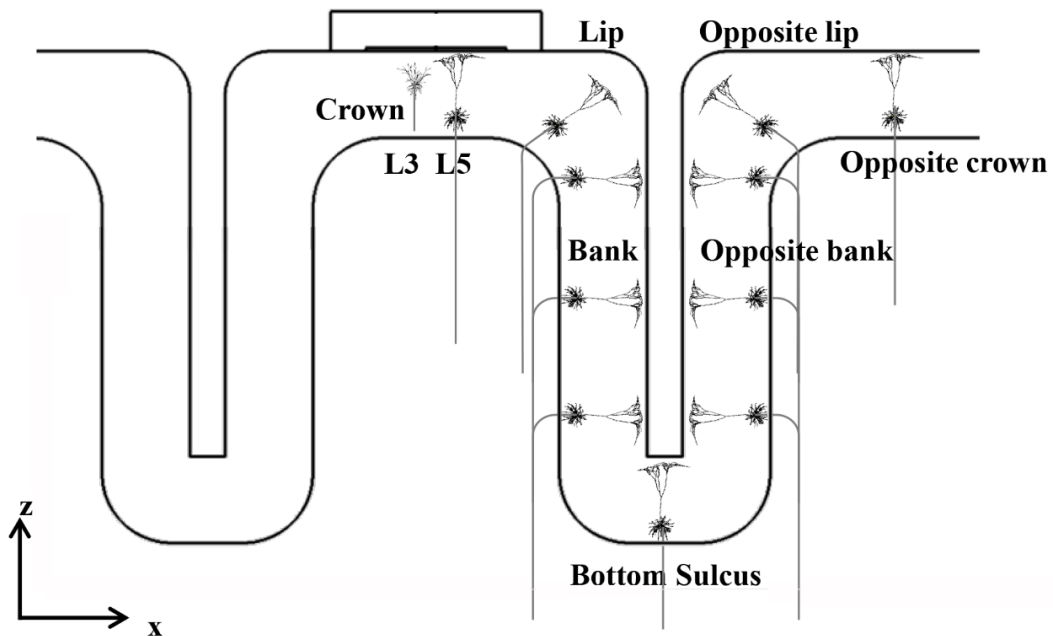


Figure 3.2 Schematic view of the neuronal model morphology and placement. Orientations of layer 3(L3) and layer 5(L5) pyramidal neuronal models are shown, with bends in different locations. They represent only one aspect of the uniform neuronal models.

the neuronal models by extracellular stimulation. We applied a monophasic rectangular stimulating pulse 100 μs in duration, and defined the excitation threshold of a neuron when the membrane potential at one of the nodes in the corresponding neuronal model was raised by 70 mV or more above the resting potential⁶³.

Rather than modeling the neuronal models within the whole brain area, we designated the region of interest (ROI) as a regular hexahedron within a volume of $5 \times 10^3 \text{ mm}^3$ with the electrodes in the middle, and placed two types of L5 and L3 neuronal models uniformly in the ROI to reduce superfluous computations. The orientation of the neuronal model was perpendicular to the cortex. L5 neurons curved beyond the boundary between GM and WM, while L3 models were located within the cortex. The soma of L5 and L3 neuronal models were placed 0.6 mm and 1.8 mm above the boundary between the GM and WM⁶¹. These neuronal models are illustrated in detail in Figure 3.2. Each of the L5 and L3 neuronal models was allocated in each triangular element comprising the GM surface and aligned with the normal direction of this element. Therefore, we constructed a total of 12,824 neuronal models each (L5 or L3) and distributed them uniformly, as shown in Figure 3.3. This process was implemented in MATLAB (MathWorks, Natick, MA, USA) and COMSOL 4.3b with MATLAB.

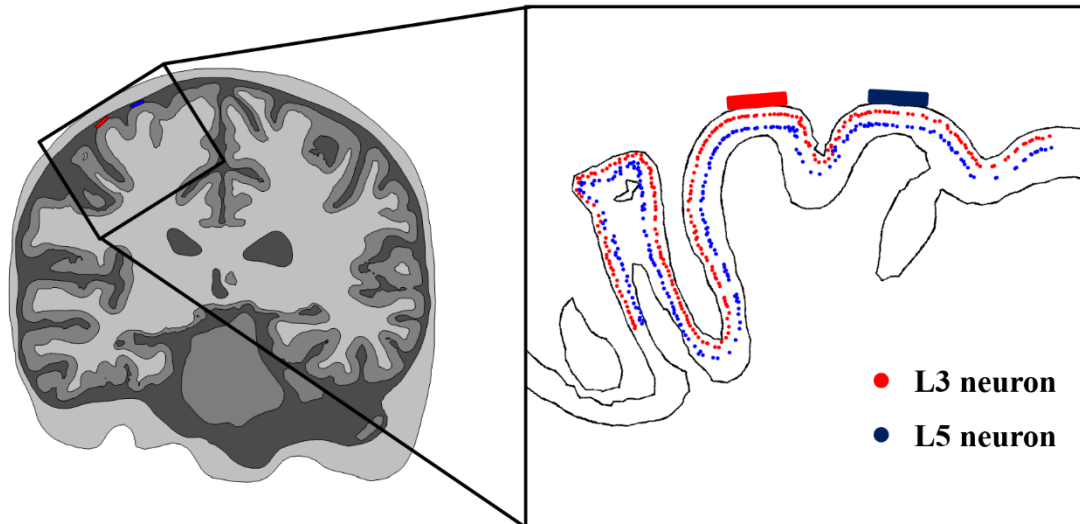


Figure 3.3 Placement of L5 and L3 pyramidal neuronal models in the anatomically realistic head model. Locations of L5 and L3 somata are marked as colored dots (blue: L5, red: L3) in cross-section passing through two electrodes.

3.3 Results

First, to investigate the influence of anisotropic conductivity on neuronal activation, we compared the effects of simulating the anisotropic and isotropic conductivity using the anatomically realistic head model. Next, to gain further insight into the anisotropic conductivity, three methods were incorporated to determine the anisotropic information. We analyzed the effect of anisotropic conductivity on pyramidal neuronal activation by increasing the stimulus amplitude up to 100 mA. Even though this amplitude is impractical, in the light of the advantages of the simulation study, we observed the tendency for neuronal responses up to this higher amplitude.

3.3.1 Comparison between anisotropic and isotropic conductivity

We assessed the changes induced by tissue anisotropy relative to the equivalent isotropic model. For the isotropic model, WM conductivity was assigned to 0.126 S/m, while fixed value anisotropy (1.1 S/m and 0.13 S/m conductivity values in longitudinal and transverse directions, respectively) was applied to the anisotropic model.

The inclusion of anisotropy in the model changed the spatial extent of the excitation thresholds, as illustrated in Figure 3.4. L5 neurons in the anisotropic model were excited in a wider area around the crown during anodal stimulation and in a narrower, but deeper, bank area during cathodal stimulation than those in the isotropic model. Like L5 neurons, L3 neurons in the anisotropic model were activated more widely during anodal stimulation than those in the isotropic model, but they were activated slightly more in the deeper bank during cathodal stimulation. The overall change induced by anisotropy was smaller in L3 than in L5 neurons. This can be accounted for as follows: most L3 neurons were located within the GM, where the anisotropic WM conductivity may have minimal effects on L3 neurons.

Figure 3.5 presents the relative ratio of L5 and L3 neurons excited in the isotropic and anisotropic models as stimulus amplitude increased. In L5 neurons, the anisotropic model yielded substantially different results from the isotropic model: the anodal stimulation excited far more neurons, while the cathodal stimulation excited noticeably fewer neurons in the anisotropic model. L3 neurons showed behavior similar to those in L5, but the difference was quite small. This demonstrated the minimal effect of anisotropy on L3

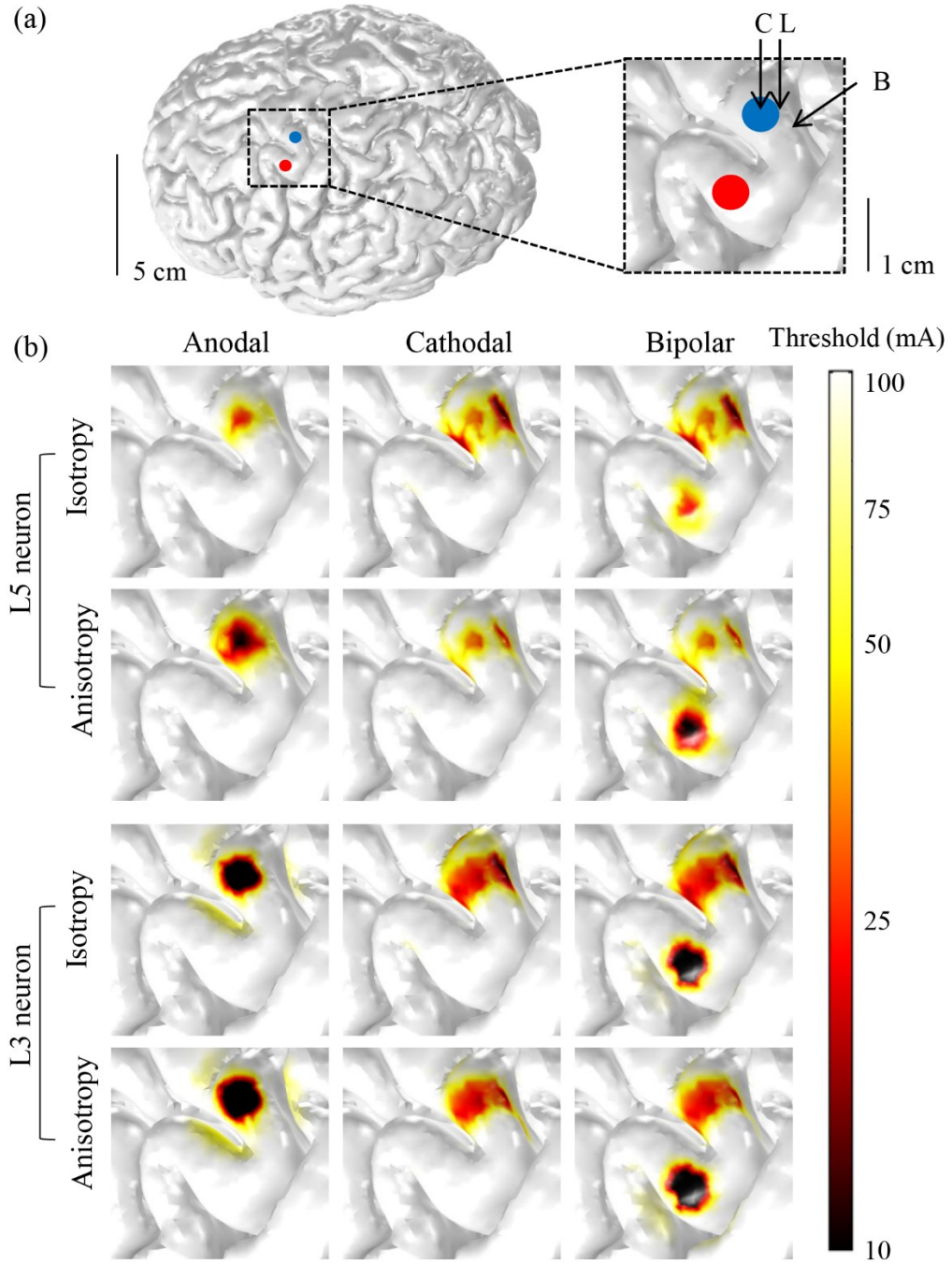


Figure 3.4 Comparison between isotropic and anisotropic conductivity for anodal, cathodal and bipolar stimulation. (a) Electrode placement in the anatomically realistic head model. Inset represents the ROI, including the crown (C), lip (L) and bank (B) on the GM. (b) The spatial extent of the excitation thresholds for L3 and L5 neurons between the isotropic and anisotropic models over three polarities.

neurons, but its relatively larger effect on L5 neurons. We observed bipolar stimulation was not noticeably different between the anisotropic and isotropic models.

Table 3.3 illustrates the minimum excitation threshold (minimum input current to modulate neurons) for three different polarities in two models (the isotropic and anisotropic models). Similar to the results in Figure 3.5, the minimum thresholds of L5 neurons were quite different between models. The anisotropic model yielded a much lower minimum threshold with anodal stimulation and a higher threshold with cathodal stimulation than the isotropic model. However, the bipolar stimulation yielded a lower threshold between the two polarities (cathodal and anodal); As for L3 neurons, there was a small difference only with cathodal stimulation; the anisotropic model had a slightly higher threshold than the isotropic model.

3.3.2 Comparison among various anisotropic conductivities

Previously, we observed that L3 neurons are considerably less sensitive to WM anisotropy than L5 neurons. In this section, we investigated further the effect of anisotropic conductivities on L5 neurons. There are various principles that apply to the adaptation of anisotropic conductivity. In addition to the fixed value anisotropy, two principles of anisotropic adaptation were introduced: volume normalization anisotropy and volume constraint anisotropy with varying anisotropic factors ($r=2, 5, 10$, and 100). A detailed description was presented in the section ‘Conductivity assignment.’

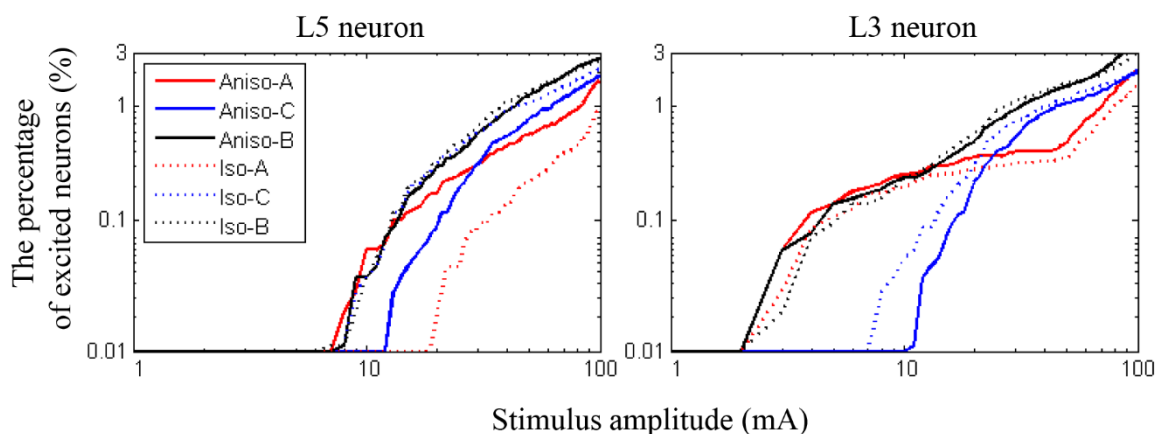


Figure 3.5 The relative ratio (%) of neurons excited with stimulation at three different polarities (anodal (A), cathodal (C), and bipolar (B) stimulation). L5 and L3 neurons in the anatomically realistic head model were compared between the isotropic (iso) and anisotropic (aniso) models.

Table 3.3 The minimum excitation thresholds (mA) over three polarities between the anisotropic and isotropic models; parentheses indicate the location of the neuron(s) excited.

polarity	L5 neuron		L3 neuron	
	Isotropy	Anisotropy	Isotropy	Anisotropy
Anodal	19 (C)	8 (C)	3 (C)	3 (C)
Cathodal	7 (B)	13 (B)	8 (B)	11 (B)
Bipolar	7 (B)	8 (C)	3 (C)	3 (C)

Figure 3.6 illustrates the spatial extent of the excitation thresholds of L5 neurons over three polarities for the six anisotropic models. Volume normalization anisotropy and volume constraint anisotropy with $r=2$ yielded almost identical behavior. As the anisotropic factor (r) in the volume constraint anisotropy increased, the anodal stimulation yielded a wider area of excitation. While the difference was quite small, the cathodal stimulation produced a slightly narrower area and seemed to activate neurons in the deeper bank as the anisotropic factor increased. Bipolar stimulation may yield the simple superimposition of anodal and cathodal stimulations.

Figure 3.7 presents the relative ratio of L5 neurons excited over the six anisotropic models (volume normalization anisotropy, volume constraint anisotropies ($r=2, 5, 10, 100$), and fixed value anisotropy). The overall behaviors of the relative ratio of L5 neurons excited were quite similar to the spatial extent of the thresholds (Figure 3.6). During anodal stimulation, both volume normalization anisotropy and volume constraint anisotropy with $r=2$ yielded comparable ratios of neurons excited, and the number of neurons excited increased as the anisotropic factor increased. In cathodal stimulation, the numbers of neurons excited showed a very small difference over the anisotropic models, but conversely, they became slightly higher as the anisotropic factor decreased. When the impractical factor ($r=100$) of volume constraint anisotropy was excluded, we found that the fixed value anisotropy yielded the greatest number of neurons excited in anodal stimulation and the fewest number in cathodal stimulation.

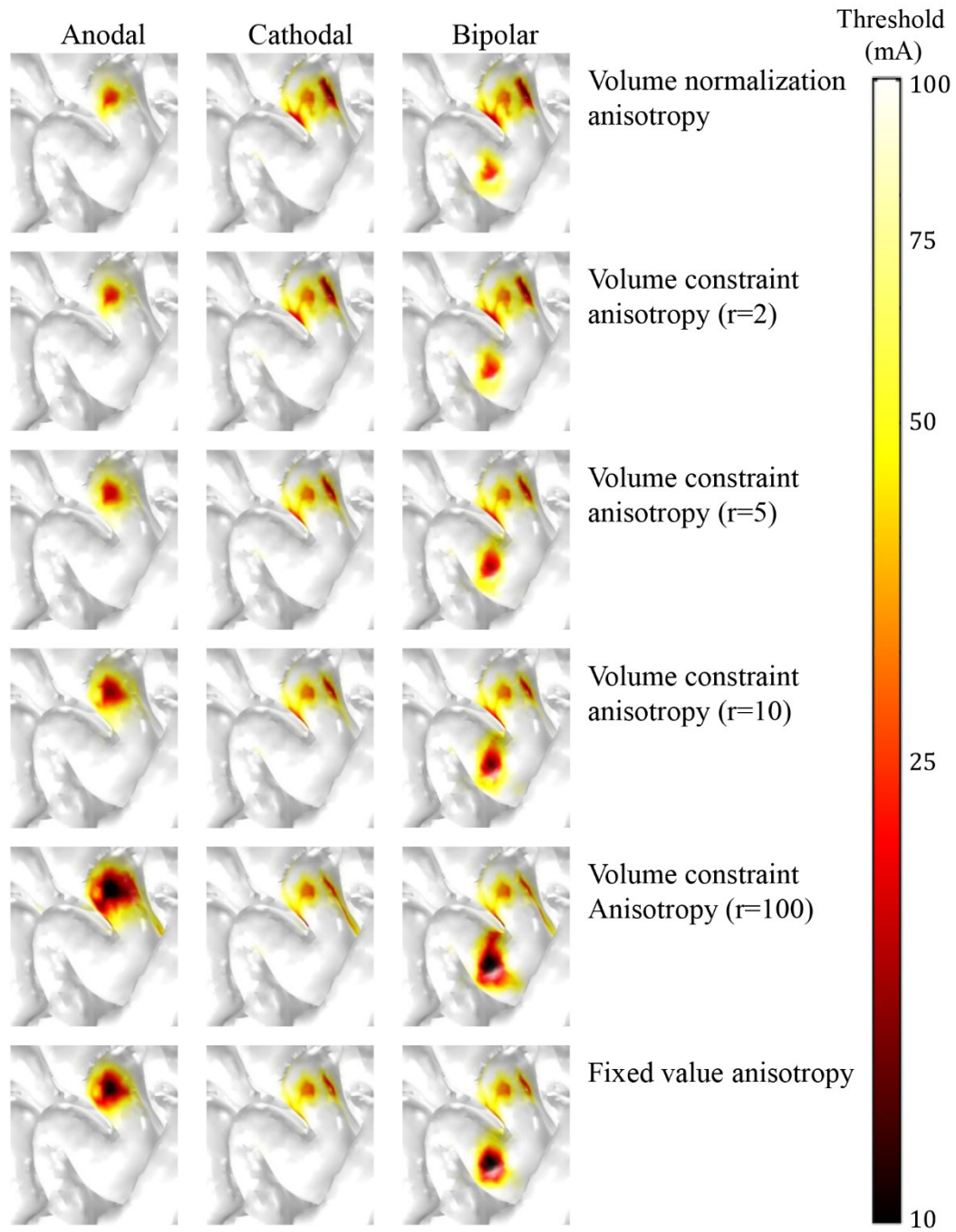


Figure 3.6 Comparison among various anisotropic conductivities for anodal, cathodal and bipolar stimulation. Spatial extents of excitation thresholds of L5 neurons are shown in various anisotropic models within the ROI shown in Fig 4(A).

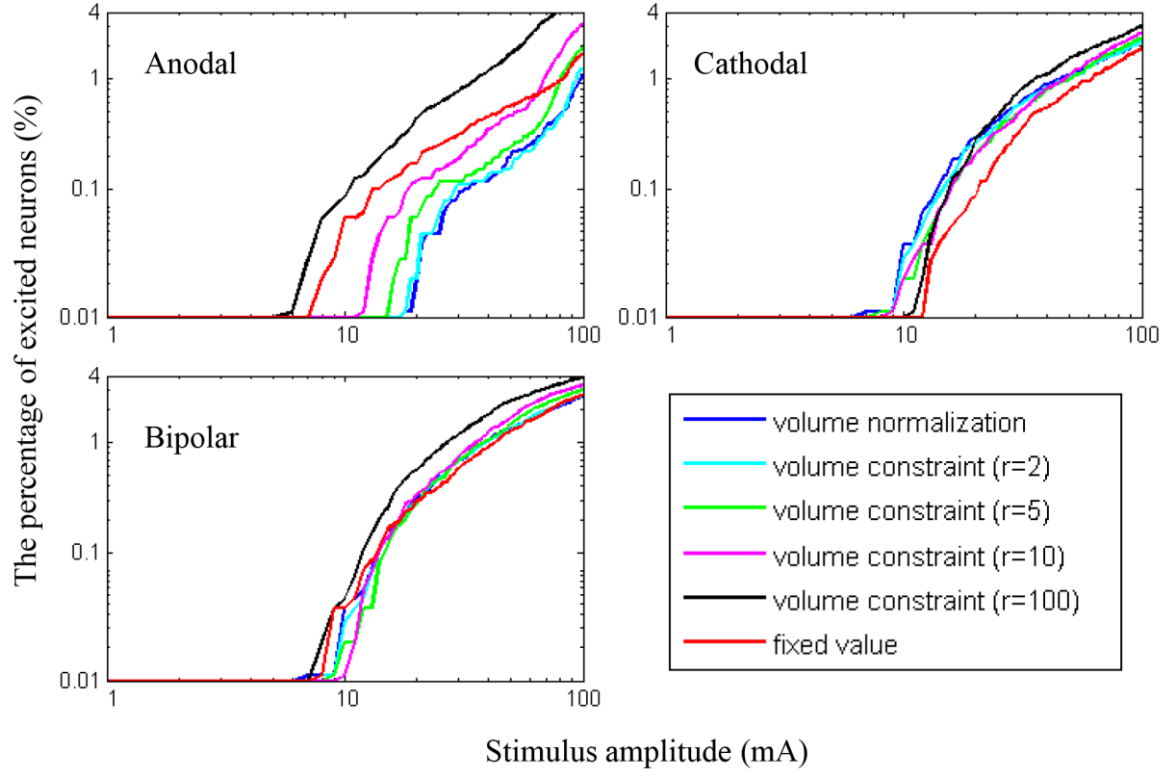


Figure 3.7 The relative ratio of the number of L5 neurons excited for three polarities. The six different anisotropic models were compared.

The minimum excitation thresholds of L5 neurons were estimated over the six anisotropic models, as tabulated in Table 3.4. It is clear that the higher anisotropic factor (r) of volume constraint anisotropy decreased the minimum threshold during anodal stimulation, while it increased the minimum threshold slightly during cathodal stimulation. Therefore, the minimum thresholds for the anodal stimulation decreased more than those for cathodal stimulation when $r=100$. The crown was the primary area activated with the minimum threshold during anodal stimulation, while the bank was activated during cathodal stimulation. It is quite interesting that for high anisotropic factors ($r=5, 10, 100$), the bipolar stimulation yielded slightly higher than minimum thresholds between the anodal and cathodal stimulations.

3.4 Discussion

To investigate the effects of the anisotropic model compared to the isotropic model, we introduced

Table 3.4 The minimum excitation thresholds (mA) of L5 neurons in the anatomically realistic head model over the six anisotropic models; parentheses indicate the location of neuron(s) excited: crown (C) and bank (B).

Polarity	Norm	Vol (r=2)	Vol (r=5)	Vol (r=10)	Vol(r=100)	Fixed value
Anodal	18 (C)	18 (C)	16 (C)	12 (C)	6 (C)	8 (C)
Cathodal	7 (B)	8 (B)	8 (B)	9 (B)	11 (B)	13 (B)
Bipolar	7 (B)	8 (B)	9 (B)	10 (B)	8 (C)	8 (C)

the principle of fixed value anisotropy, choosing eigenvalues reported by Wongsarnpiggon et al.^{61,108}. During anodal stimulation, the anisotropic model activated neurons in a relatively wider area than the isotropic model; however, during cathodal stimulation, we observed conversely that a narrower area was activated in the anisotropic model than in the isotropic model. Consistently, the anisotropic model had the lowest minimum thresholds during anodal stimulation, while the isotropic model showed the lowest minimum thresholds during cathodal stimulation. These results produced by the anisotropic model matched well with previous studies^{3,52,53,61,109,115,116}, which reported that anodal stimulation had a lower minimum threshold than cathodal stimulation, while isotropic stimulation did not. We observed that anisotropic conductivity played a critical role in neuronal activation; such observations have been reported in studies on source localization or noninvasive stimulations^{40,121,122}.

To investigate further the effects of the anisotropic models on neuronal activation, we adapted two types of approaches to determine the anisotropic information derived from the DT-MRI. First, we looked at the volume normalization anisotropy, which normalizes conductivity tensors to compensate for variations in isotropic conductivity. Second, we investigated volume constraint anisotropy, which is used with a wide range of anisotropy ratios. We found that variation in the anisotropic information induced an altered spatial extent of the threshold and percentage of excited neurons, especially in anodal stimulation; however, it is still ambiguous which approach is appropriate. According to previous work^{108,123}, the anisotropic ratio of WM is known to be 1:10. However, due to the paucity of direct measurements of anisotropic conductivity¹⁰⁸ and the variation (both regionally and pathologically^{40,124}) in the anisotropy ratios, the optimal method of taking into

account WM anisotropy remains unknown to date.

Several previous modeling studies have investigated the effects of invasive cortical stimulation at the neuronal level^{52,53,61,63} by developing a simplified extruded slab model and examining the influence of various parameters on neuronal activation. In the early stages, a small number of neuronal models were constructed on the precentral gyrus^{52,53}, and the leverage of model geometry, electrode placement and stimulus polarities were tested. More recently, a greater number of neuronal models and more varied types of neurons have been introduced in a larger cortical area^{61,63}. Most of these studies have focused on the investigation of activated neural elements produced by ECS^{52,53,61}. Furthermore, Zwartjes et al. proposed stimulation protocols that target selected neuronal populations⁶³. Although they provided insight with respect to neuronal activation, information related to SuCS is difficult to predict due to the different placement of electrodes. Moreover, those neuronal models were coupled with the simplified extruded slab model, which represents the precentral gyrus only. Thus, in this study, we used the anatomically realistic head model with anisotropic conductivity derived from MR-DTI to yield more accurate extrapolation of neuronal activation, which may be distinct from earlier work.

Electrode location (on/under the dura mater), detailed neuronal morphologies, and computationally realistic brain models were also introduced distinctively in this work, but we observed results consistent with existing studies. During anodal stimulation, the crown, which lies beneath the active electrode, was the most excitable area, as most neurons in the crown were perpendicular to the electrode surface. In addition to the crown, cathodal stimulation favored excitation of the upper bank, where neurons are aligned primarily parallel to the electrode surface. Further, we found that axons were more excitable than soma and dendrites. These results are consistent with those reported in earlier studies^{52,53,61,63}.

It is interesting to note that the spatial extent of the excitation thresholds in bipolar stimulation was almost identical to the superimposition of both anodal and cathodal stimulations. This may be due to the large electrode center-to-center distance (13 mm in this work). It has been reported^{52,53,61,63,125} that the anodal and cathodal fields during bipolar stimulation scarcely interfered with electrodes at least 10 mm apart, which is relevant to our results.

Our empirical results showed consistently that anodal stimulation activated pyramidal neurons directly at lower amplitudes than cathodal stimulation^{3,109,115,116}. Further, Hern et al. reported that in

corticofugal fibers, cathodal stimulation elicited excitation thresholds 1.5-5 times higher than anodal stimulation¹¹⁵. Comparing the minimum excitation thresholds in the anatomically realistic head model with fixed value anisotropy, anodal stimulation was 8 and 3 mA for the L5 and L3 neuronal models, respectively, while cathodal stimulation was 13 and 11 mA. Thus, cathodal stimulation was 1.6 and 3.7 times higher than anodal stimulation for L5 and L3 neurons, respectively. These results reconfirm the fact that anodal stimulation produces lower current thresholds than cathodal stimulation, and these ratios agree well with the results of other experiments¹¹³. Further, we found that pyramidal neurons in the lip of the central sulcus responded at lower thresholds in cathodal than anodal stimulation, which is consistent with the results of Phillips' experiment¹¹⁶.

Responses in the pyramidal tract following cortical stimulation are known to be classified into D- and I- wave responses^{109,116,126}. The initial positive deflection is interpreted as a D-wave, which is likely produced by direct activation of cells in the motor cortex. Next, a series of variable positive deflections of the I-wave follow from synaptic excitation and/or re-excitation of pyramidal cells with longer latencies. According to Gorman¹⁰⁹, at the threshold of stimulating intensities to evoke neuronal responses, the D-wave was elicited in anodal stimulation, while cathodal stimulation evoked I-waves. At suprathreshold stimulating intensities, both anodal and cathodal stimulation produced D- and I-waves. At supramaximal stimulation, cathodal stimulation produced larger amplitude D- and I-waves than anodal stimulation. In this work, we explored the individual neuronal responses to determine the cellular target of stimulation, so that we could observe direct responses (D-wave) only. The rate of neurons excited in the anisotropic model well represented the comparison between polarities, as shown in Figure 3.5. When anodal stimulation began to trigger action potentials, cathodal stimulation did not. Moreover, anodal stimulation excited more neurons at lower amplitudes than cathodal stimulation. However, by increasing the stimulus amplitude, cathodal stimulation evoked action potentials in more neurons than anodal stimulation. These results are consistent with previous experimental observations of the D-wave.

Wongsarnpigoon et al. studied the effects of electrode position and geometry on neuronal activation by ECS⁶¹. Before beginning the study, they validated a compartmental pyramidal neuronal model located in the crown by comparing it with experimental data. In this work, we employed the pyramidal neuronal models used in Wongsarnpigoon et al.⁶¹, which were modified versions of cat visual cortex¹¹⁰ fitted to human brain

geometry. These provided a valid rationale of the simulation results that well matched those in our study.

In our model, we considered the L5 and L3 pyramidal neuronal models; their morphologies and electrical properties were taken from cat visual cortex¹¹⁰, because to our knowledge the properties and morphologies of most human cortical neurons have not been described well thus far. Due to this uncertainty with regard to neuronal properties, computational results may lead to inaccurate neuronal responses. For example, in the previous modeling study¹²⁷, the presence of collaterals reduced the excitation threshold by 50%, and even evoked action potentials in neurons that were perpendicular to the electrode during cathodal stimulation⁶³, while unbranched neurons were not activated¹²⁵. Despite this possible discrepancy in the neuronal models, we reproduced quite reasonable computational results that are comparable to experimental data. As a consequence, we expect that excitation thresholds induced by SuCS may be estimated reasonably through our computational model.

We constructed individualized and non-communicating populations of neurons. This limits the observations of the I-wave that is followed by indirect and trans-synaptic activation. The reason for investigating the I-wave is that, under certain conditions, cathodal stimulation activated cellular targets more readily than anodal stimulation². This implies that motor cortex stimulation activates cortical neurons largely indirectly. Although observing multiple interconnected neurons is important in indirect responses, the response of a single pyramidal neuron is also useful¹¹⁶. Because these neurons are activated directly from the common path issuing from the cortex, they may give evidence of which neurons are recruited by the stimulus-induced electric field.

There were several limitations in our modeling study with the anatomically realistic head model: first is the substrate shape inserted. In this work, we only considered substrates surrounding electrodes. In order to investigate whether the substrate shape affects neuronal excitation, we constructed two types of electrodes in the simplified extruded slab model. One was a $5 \times 18 \text{ mm}^2$ sized strip-type electrode and the other was a disc-type electrode with covered substrates that were designed for this study. Then, we compared the excitation thresholds of L5 neurons during bipolar stimulation, and the thresholds differed only up to an average of 0.37%, which is negligibly small. Even though the complex brain geometry of the anatomically realistic head model may be affected by these changes, it is also possible that it has only a minor influence. Another modeling issue is the construction of the dura mater. Due to the extreme thinness of the dura mater,

we were not able to include it in the anatomically realistic head model. However, because electrodes in SuCS are located under the dura mater and we focused on activation within the cortex, the exclusion of the dura mater may be permissible. We underpinned it by comparing the extruded slab model with and without dura mater, which showed 0.003% differences in the excitation thresholds of L5 neurons during bipolar stimulation. Dura mater construction is necessary to consider ECS further, as it is used more widely than SuCS. Thus, the inclusion of the dura mater in both ECS and SuCS computational studies will be considered in future work.

IV. A multi-scale computational model of the effects of TMS on motor cortex

4.1 Introduction

The efficacy of TMS has been demonstrated; however, there remains a large degree of uncertainty regarding the factors influencing the affected brain areas and relevant circuits. To provide a better understanding of the biophysical mechanisms behind TMS, several computational studies have been performed to try to reveal the effects of a number of parameters that lead to variable outcomes. The majority of models predict the brain regions influenced by TMS based on stimulus-induced electric fields^{55,78}. While early studies utilized spherical models of the human head, in recent years high-resolution volume conduction models of the head were developed from human magnetic resonance imaging (MRI) to improve accuracy of calculated electric fields^{41,42,47,73,77,79,128–130}. These models revealed that the geometry of the volume conduction model, such as complex gyral folding patterns and sulcus width, is one of the key parameters determining the induced electric field. In addition, computational studies were extended by connecting numerical results with experimental observations to show the correlation between computed electric fields with physiological observations^{67,131,132}.

Directly monitoring target cells' activities under stimulation would be immensely valuable for the interpretation of TMS effects, but few such studies exist^{133,134}. However, computational studies can explore the effects of the electromagnetic fields on neural activation by simulating models of neural stimulation in silico. In early computational models, straight axonal fibers were considered numerically and the response of neurons induced by the external field was modeled by means of the cable equation^{87,89}. Later models investigated the role of cell morphology using multi-compartmental modeling^{51,54,62}. Since the responses of cortical neurons vary depending on not only the neuronal morphology but also orientation relative to the induced electric field and stimulus amplitude^{55,56,85,119}, anatomical information such as cortical folding that induces a wide range of field orientations was fed into the neuronal models by applying the calculated electric field from the head model to the neuronal models^{94,135}.

Here, we use an advanced multi-scale modeling approach that combines a high-resolution head model with detailed multi-compartmental neuron models. We construct an anatomically realistic head model

based on MRI and calculate the external currents that affect neurons via the TMS-induced electric field with high accuracy. We concentrate on the hand knob area of the motor cortex that is the predominant target of many TMS studies^{1,131}. A multitude of layer 5 and layer 3 pyramidal neurons (L5/L3 PNs) is incorporated on the basis that they might be primary activators of the corticospinal tract and provide the main input to the direct pathway^{54,94,109,136}. We estimate the target area of activation as a function of coil orientation as well as the stimulation intensities required to activate neurons. Finally, we predict the precise sites where the neurons initiate their action potentials.

4.2 Methods

In order to study the cellular effects of TMS in the brain we employed a multi-scale computational modeling approach combining a volume conductor head model with detailed neuronal models of cortical pyramidal neurons. The motor cortex, especially the hand area, was considered as a cortical target location. The volume conductor head model was used to simulate the stimulus-induced electric fields. The precise impact of these fields on different neural targets was evaluated using multi-compartmental models of pyramidal neurons embedded into the head model. This allowed us to predict differences in individual neuron's susceptibility to TMS depending on neuron placement and coil orientation.

4.2.1 Volume conductor model

The simulated effects of TMS depend not only on stimulation parameters but also on the anatomical information specified in the volume conductor model. To calculate the precise electric field, a volume conductor head model for TMS that reflected T1-weighted and T2-weighted magnetic resonance (MR) images was constructed using SimNibs v1.1^{41,137}. Briefly, segmentation of white matter (WM), gray matter (GM), cerebrospinal fluid (CSF), skull and skin was based on FreeSurfer v5.3.0^{98,120}, FSL v5.0.0⁹⁹ and MeshFix v2.0¹³⁸, as shown in Figure 4.1(a). Then, the head model was constructed by generating an optimized tetrahedral volume mesh using an enhanced resolution in the region of interest (ROI) around the hand knob using Gmsh¹³⁹. The total number of tetrahedral elements was approximately 5.6 million. At each layer of the head model, isotropic conductivity was assigned with the following values (in S/m): WM: 0.126;

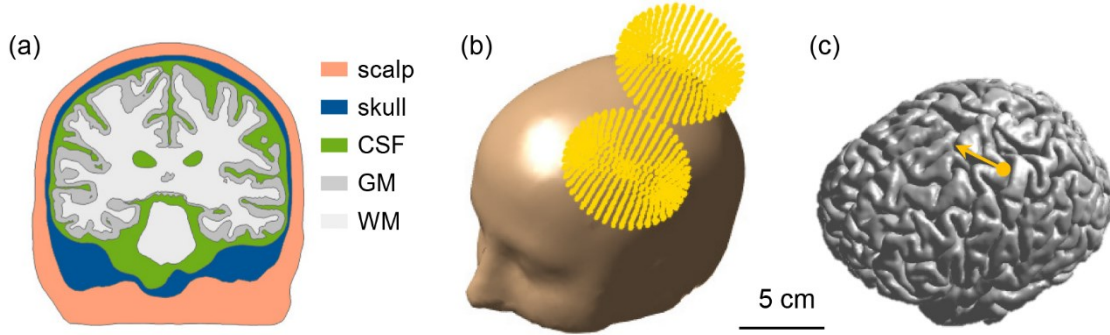


Figure 4.1 The volume conductor model and coil placement. (a) Cross-section displaying the scalp, skull, cerebrospinal fluid, gray matter and white matter. (b) The computed coil location is superimposed on the head model. (c) The yellow dot indicates the location of the center of the TMS coil on the border between gray matter and cerebrospinal fluid, and the coil handle is oriented in the direction of the yellow arrow.

GM: 0.276; CSF: 1.654; skull: 0.01; and skin: 0.465.

4.2.2 Field calculations

The electric field induced by TMS was calculated using SimNIBS v.1.1^{41,137}, $\vec{E} = -\frac{\partial \vec{A}}{\partial t} - \nabla \phi = -\vec{E}_p - \vec{E}_s$, consisted of primary (\vec{E}_p) and secondary (\vec{E}_s) electric fields. The primary electric field was directly determined by the coil geometry and the head model. The secondary electric field was solved via a finite element method using the GetFEM++ library and MATLAB^{137,140}. The Magstim 70 mm figure-8 coil was represented by magnetic dipoles positioned above the hand knob (Figure 4.1) and the stimulator output was set to 1 A/ μ s. The coil orientation was defined relative to the direction of the central sulcus such that the electric field induced was in anterior to posterior direction (Figure 4.1(c)). Then, three additional coil orientations were tested by rotating in steps of 45 degrees and reversed orientations were simulated by changing the sign of the current through the coil.

To investigate the TMS-induced cellular effects, we quantified the magnitude of the electric field $|\vec{E}|$ and the orthogonal component of the electric field $E_{\perp} = \vec{E} \cdot \vec{n}$ to the gray matter surface, where \vec{n} is the normal vector for the boundary surface element. The orthogonal component was expected to contribute to TMS-induced brain activation by the theoretical cortical column cosine model of TMS efficacy (C^3 -model)^{73,141}.

4.2.3 Multi-compartmental neuronal models

We adapted existing multicompartmental models of layer 5 and 3 pyramidal neurons (L5/L3 PNs) from cat visual cortex¹¹⁰ using the NEURON simulation software¹¹¹. The electrical properties were unchanged from the original models. Briefly, a high density of fast, inactivating voltage-dependent Na⁺ channels were present in the axon hillock and axon initial segment, and a low density of these channels was presented in the soma and dendrites. Slow Ca²⁺-dependent K⁺ channels and high threshold Ca²⁺ channels were located in the soma and dendrites. Except for the dendrites, fast K⁺ channels were present. L5/L3 PNs were combined virtually with the head model and modified to accommodate the irregular geometry of the cortex^{53,58,61,63,94,135}, as shown in Figure 4.2. The dendritic trees were lengthened or shortened by re-scaling them according to the local dimensions of the cortex such that dendrites reached layer 1 and the orientation was perpendicular to the cortical surface^{61,112}. Since the morphology of the dendritic trees was not symmetric and it might influence the neuronal activation, L5/L3 PNs had randomly rotated dendritic trees at different locations. The axons of L5 PNs were defined to curve beyond the boundary between GM and WM toward the corpus callosum. The axons of L3 PNs were defined to terminate in layer 5/6 within the GM. To reduce superfluous computations, we preselected a region of interest (ROI) of $50 \times 50 \times 50 \text{ mm}^3$ around the hand knob and then placed L5/L3 PNs in each triangular element comprising the gray matter surface. Altogether, a

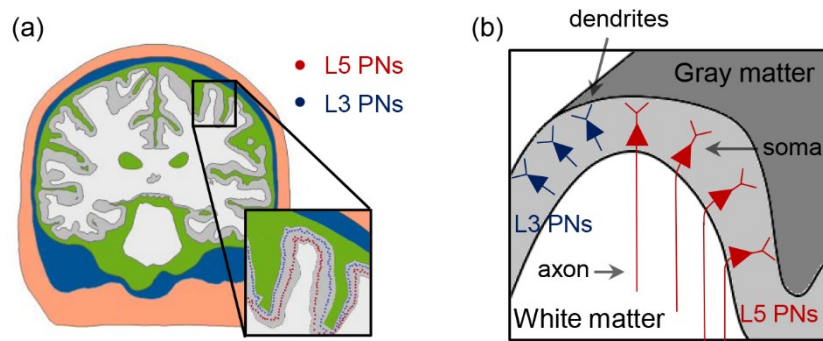


Figure 4.2 The placement of L5/L3 PNs in the head model. (a) The distributions of somata of L5/L3 PNs are marked as colored dots (red: L5; blue: L3). (b) A schematic view of the distribution of the L5/L3 PNs is shown along the cortex folding (gray colored area); note the bending of L5 PN axons when crossing the boundary between gray matter and white matter.

total of 10,888 L5 PNs and 10,888 L3 PNs was constructed. This process was implemented in MATLAB (MathWorks, Natick, MA, USA).

4.2.4 Computation of neuronal activation induced by stimulation

The membrane potentials induced by stimulation were approximated by adding an external current source I_{ext} to the cable model^{31,54,62,87,89}:

$$I_{ext} = -\frac{1}{r_a} \frac{\partial E_l}{\partial l},$$

where r_a is the axial resistance per unit length and E_l represents the component of the electric field that is parallel to each compartment of the PNs. The derivative of the electric field along each compartment was calculated at each center point by $\vec{l}^T(\nabla E)\vec{l}$, where ∇E contains the components of the electric field gradient tensor that are estimated by computing the difference of electric fields at neighboring points displaced by ± 1 mm along each axis¹¹⁷.

We calculated a monophasic pulse that induced a fluctuating magnetic field through an RLC circuit as detailed in⁵⁷,

$$i(t) = \sin(\omega t) \exp(-t/\tau),$$

where $\omega = 30$ kHz is the angular frequency and $\tau = 0.08$ ms is the decay time. The I_{ext} at each compartment was then multiplied by the normalized time derivative of the monophasic pulse. Finally, we obtained the spatial and temporal membrane potential dynamics. They were used to measure the excitation thresholds, the stimulation site and action potential propagation.

4.3 Results

Figure 4.3 depicts the magnitude of the electric fields ($|\vec{E}|$, top row) and the orthogonal component of the electric fields (E_{\perp} , bottom row) for different coil orientations. All calculations were performed for a rate of change of the coil current of 1 A/ μ s. Electric fields had higher magnitudes in the precentral and postcentral gyrus and focused on the top of the gyri, regardless of coil orientations. We observed only slight changes in the field strengths depending on coil orientation. In contrast, the orthogonal component of electric

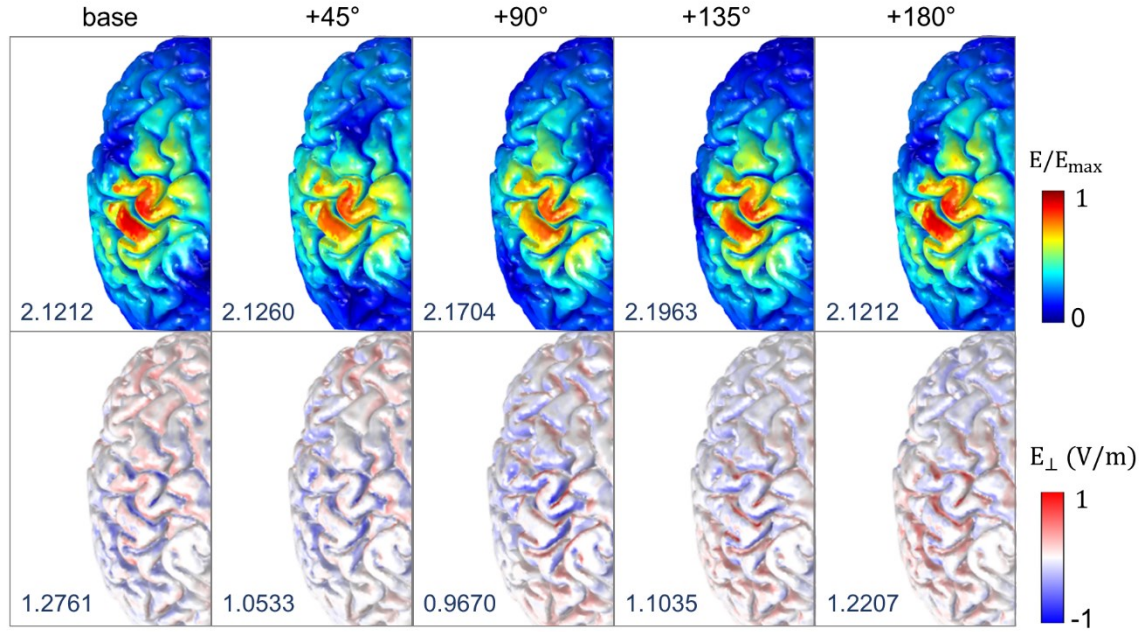


Figure 4.3 Effects of coil orientation on the electric fields. The spatial patterns of magnitude of electric fields ($|\vec{E}|$, top row) and its component orthogonal to the gray matter surface (E_{\perp} , bottom row) are visualized; the color scale is adapted for better visualization. The black arrows indicate different coil orientations, and the maximum value of $|\vec{E}|$ and E_{\perp} (measured in V/m) are given in the bottom left of each figure.

fields (E_{\perp}) showed different spatial patterns compared to the electric field magnitude. High strengths of E_{\perp} were found on the walls of the gyri and strongly depended on coil orientation. Furthermore, while the spatial extent of $|\vec{E}|$ was the same for the standard orientation and the +180 degree orientation, the sign of E_{\perp} in the +180 degree orientation was reversed due to the reversed sign of the induced electric fields. Interestingly, the maximum value of $|\vec{E}|$ depended on coil orientation; it was lowest in the standard coil orientation and highest at +135 degrees. However, the maximum values of E_{\perp} were highest for the standard coil orientation and lowest at +90 degrees.

To assess the neuronal activations as a function of coil orientation, we determined the excitation threshold required to cause action potentials of L5/L3 PNs. For each coil orientation, we kept increasing the stimulator output until a neuron generated an action potential or we reached a maximum rate of change of the current defined as 171 A/ μ s. Our focus is on the excitability for a stimulation intensity corresponding to 67 A/ μ s, as this value corresponds to the average motor threshold for the Magstim 200 stimulator connected

to the coil modeled^{67,117,135,142}. The excitability of L5/L3 PNs was predicted either by the direct estimation of the electric field (E_{\perp} map in the Figure 4.4(c)) or by simulating the induced depolarization and firing of the detailed neuronal models (threshold maps in Figure 4.4(d,e)). The color of the threshold maps represents the stimulator output necessary to activate the corresponding cell and the estimated excitable area in the E_{\perp} maps. The blue colored areas indicate an excitability in the opposite direction, because the head model was linear with respect to the electric field. As shown in Figure 4.4(a), we virtually divided the precentral and postcentral gyrus to better visualize the excitability in the walls of the gyrus.

In L5 PNs, we observed that the predicted excitability depended on coil orientation for both E_{\perp} and threshold maps (Figure 4.4(c,d)). For the base orientation and +45 degrees, a high excitability was predominantly observed in the wall of the precentral gyrus. In contrast, for orientations +90 degrees to +225 degrees we observed high excitability in the wall of the postcentral gyrus. Comparing these threshold maps to the E_{\perp} maps, we see that the threshold maps show activated L5 PNs in some additional smaller areas with comparatively small E_{\perp} values. From +90 to +180 degrees, the excited regions were quite well matched to the results from E_{\perp} . Furthermore, in the standard direction, the spatial extents of L5 PNs that were activated for stimulation intensities corresponding to the motor threshold seemed to enlarge with increasing coil rotation, while for the opposite direction of the coil current highly excitable areas shrank with increasing coil rotations.

Overall, the excitability in L3 PNs showed behavior comparable to that of L5 PNs (Figure 4.4 (d,e)), but notable differences in threshold maps between L5 and L3 PNs were as follows: while L5 PNs in the top of the gyri were never activated, L3 PNs were excited in the top and also the wall of gyri. The excitable areas of L3 PNs caused by the +90 and +135 degree stimulations were relatively focused on the upper parts of the wall of the postcentral gyrus, while L5 PNs placed in the deeper parts of the sulcus were activated. Furthermore in L3 PNs, the excitability in the precentral gyrus and the postcentral gyrus was comparable and a bigger area was affected than for L5 PNs. The discrepancies between L5 and L3 PNs confirmed that the morphology and placement of neuronal models has an important impact beyond the position relative to the coil.

The percentage of excited neurons for a stimulation intensity at the motor threshold is shown in

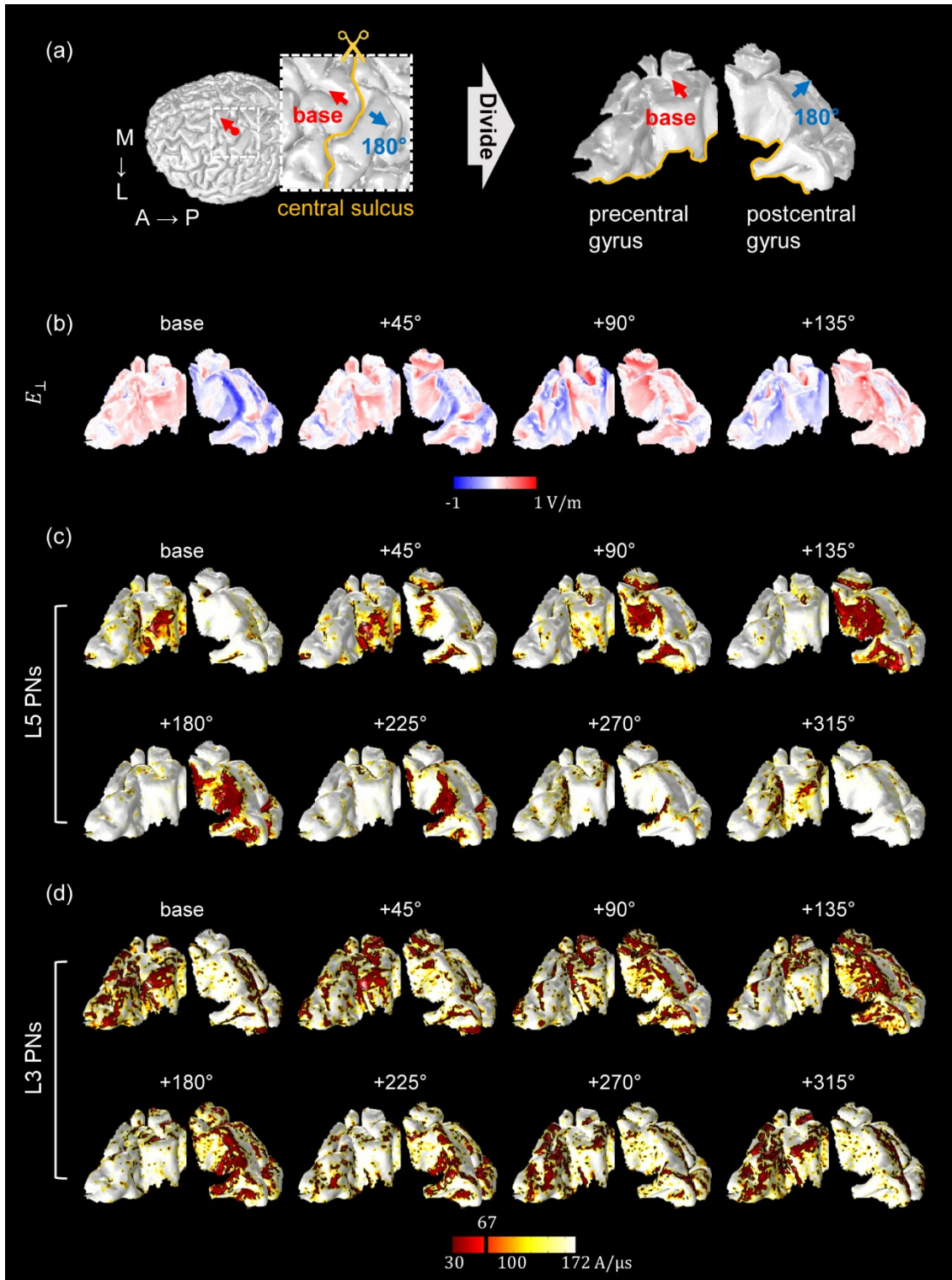


Figure 4.4 The spatial extent of predicted excitability based on the orthogonal component of the electric field (E_{\perp}) and detailed simulations of L5/L3 PNs. (a) The red dot on the border between GM and

CSF indicates the location of the center of the coil. The base orientation is shown as red arrows. The inset represents the region of interest in which PNs were distributed. The blue arrows indicate the opposite coil orientation (+180°). The precentral and postcentral gyri were virtually divided for visualization purposes. The spatial patterns of E_{\perp} (b) and threshold maps of L5 (c) and L3 (d) PNs depended on coil orientation as shown. The black and red colored areas in the threshold maps (c-d) indicate the excitable areas under the stimulator output corresponding to the average motor threshold ($67 \text{ A}/\mu\text{s}$). The directions of coil orientations in the 2nd row are the opposite directions of the 1st row (in the threshold map in (c and d)) simulated by changing the sign of the current through the coil. Note how the excitable areas strongly depend on the coil orientation.

Figure 4.5. Consistent with the results for the threshold maps in Figure 4.4 we found that the percentage of excited L5 PNs increased from base to +135 degrees and then decreased gradually thereafter. Similarly, the maximum percentage of excited L3 PNs was observed when the coil was rotated at +135 degrees and L3 PNs had about two times higher activations over all coil orientations. The overall percentage of excited neurons under the maximum stimulator output ($171 \text{ A}/\mu\text{s}$) had a similar pattern; in standard orientation, 29% and 38% of L5 and L3 PNs were activated, respectively, and these numbers increased to 33% and 44% when the coil was oriented at +135 degrees.

The majority of action potentials were initiated at the axon initial segment and others at the axon near the boundary between GM and WM for L5 PNs and at the middle and terminal points for L3 PNs (Figure 4.6). In the base orientation, threshold stimulation elicited action potentials first at the initial segment for 90% of both the L5 and the L3 PNs. This fraction increased with increasing coil rotation up to 97% at +135

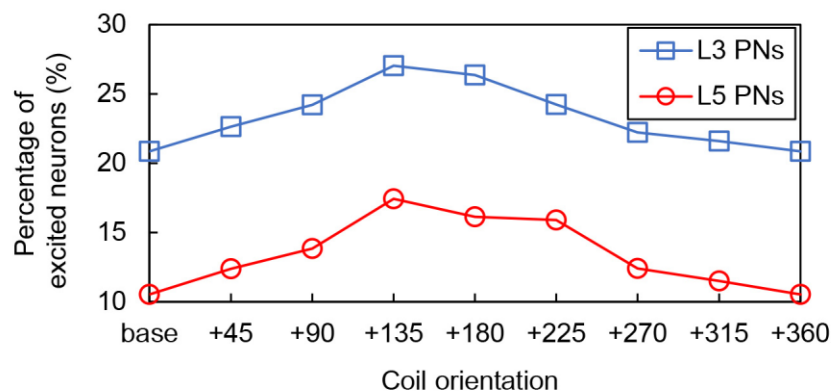


Figure 4.5 The percentage of L5 and L3 PNs that are activated for a stimulation intensity at the motor threshold ($67 \text{ A}/\mu\text{s}$) as a function of coil orientation.

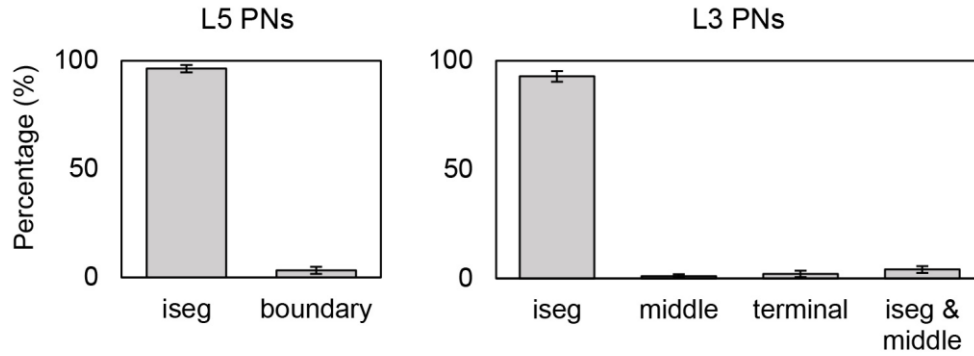


Figure 4.6 The percentage of action potential initiation sites of L5 and L3 PNs for a stimulation intensity corresponding to the motor cortex threshold ($67 \text{ A}/\mu\text{s}$) averaged over different coil orientations. Sites include the axon initial segment (iseg) and the boundary between gray matter and white matter (boundary). Additionally, the terminal part (terminal) and middle point of the axon (middle) for L3 PNs were considered. Most action potentials are first evoked at the axon initial segment of L5 PNs ($96.31 \pm 1.72\%$) and L3 PNs ($92.76 \pm 2.42\%$). The remaining number of L5 PNs show action potential initiation at the axon near the boundary between gray matter and white matter. Only few L5 PNs ($0.49 \pm 0.14\%$) initiate action potentials simultaneously at the axon initial segment and the GM-WM. For L3 PNs, middle ($1.05 \pm 0.78\%$) and terminal points ($2.08 \pm 1.45\%$) of axons are also activated occasionally.

degrees in L5 PNs and up to 95% at +90 degrees in L3 PNs. Example plots of membrane potential dynamics induced by the threshold stimulus evoking action potentials are shown in Figure 4.7. We observe the propagation of the action potentials from the axon initial segment to the more distal parts of the neurons. In both L5 and L3 PNs, following the action potential at the initial segment, the soma was activated as it is closest to the initial segment. The terminal points of the axons were activated last as they are most distal from the axon initial segment. Since the axon of a L5 PN is quite long compared to that of a L3 PN, the arrival of the action potential at the terminal point was substantially delayed. Similarly, dendrites of L5 PNs showed delayed activation while in the L3 PNs dendrites were occasionally activated.

The PNs that were morphologically reconstructed had asymmetric dendritic trees that might affect the neuronal responses. We studied the impact of dendritic trees on threshold maps and the percentage of excited neurons for a stimulation intensity at the motor threshold by rotating them in steps of 45 degrees around the axis defined by their apical dendrite for a fixed coil orientation at +180 degrees. In the threshold maps for L5 PNs as shown in Figure 4.8, the highest variations of the thresholds caused by these rotations

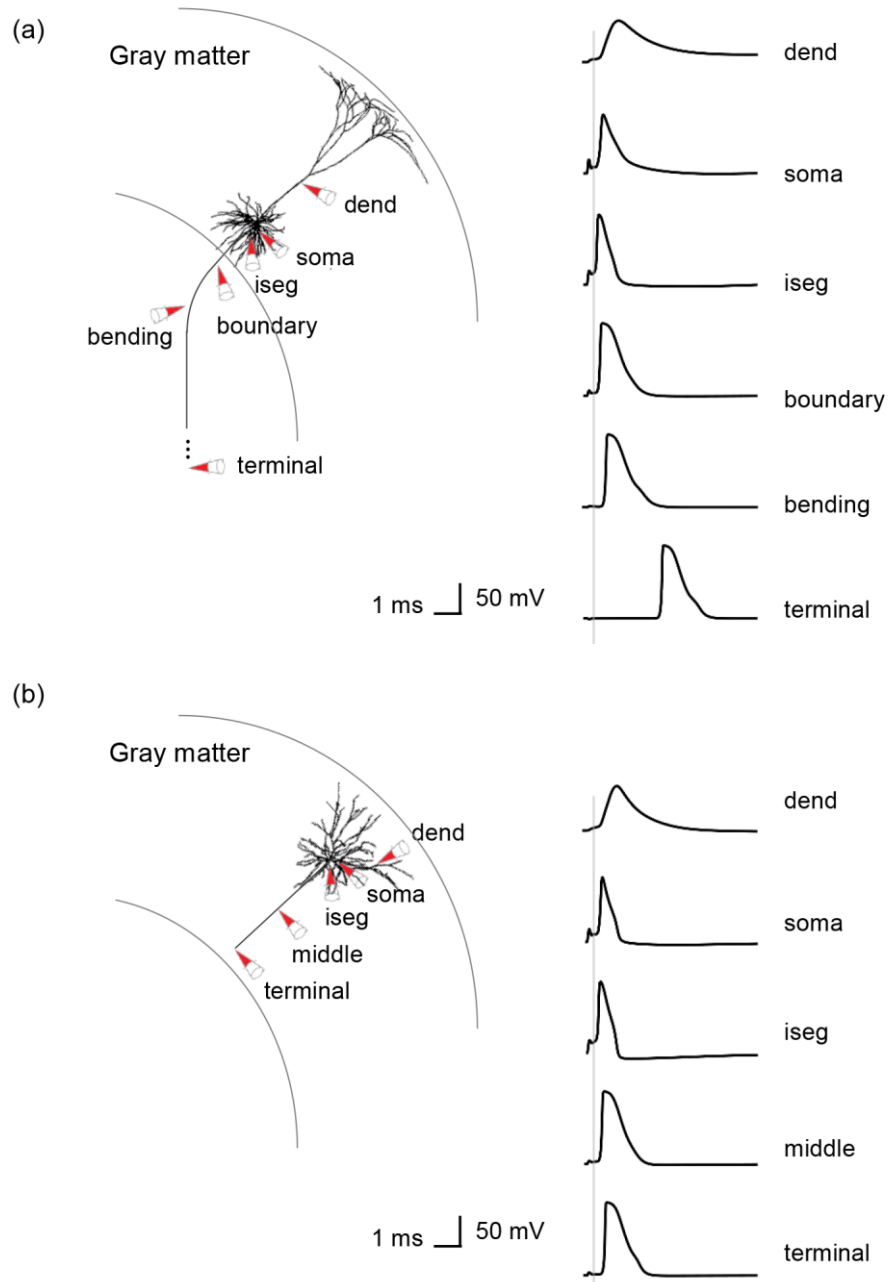


Figure 4.7 Virtual recordings of membrane potential dynamics of L5/L3 PNs. The simulated recordings were performed from dendrites (dend), soma and parts of the axons, as indicated by the red colored cones. (a) In a L5 PN, the membrane potentials are recorded at the axon initial segment (iseg), the location where the axon crosses the boundary between gray matter and white matter (boundary), bending and terminal points. (b) Additionally, the middle points of axons of L3 PNs are recorded.

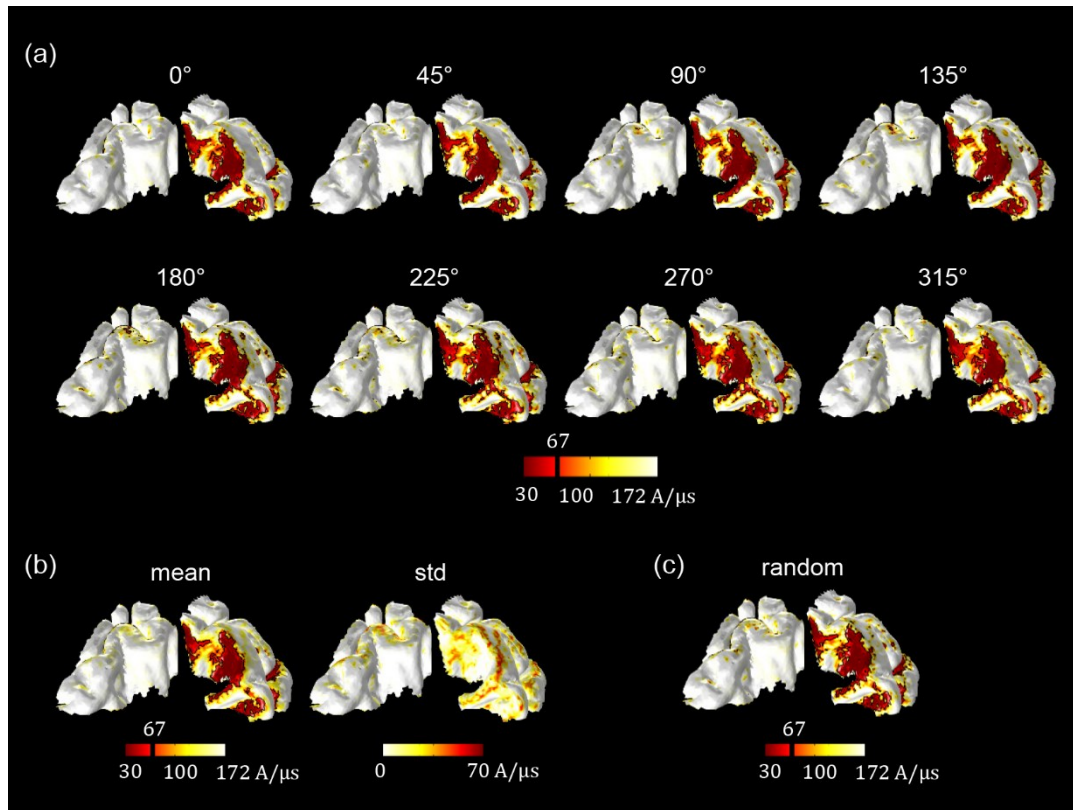


Figure 4.8 The impact of dendritic tree morphology of L5 PNs was evaluated by rotating them in steps of 45° for a fixed coil orientation at +180°. (a) The threshold maps according to the different orientations of dendritic trees and (b) its mean and standard deviation are shown. The map of standard deviations in (b) indicates precise orientation of the dendritic tree can alter activation thresholds in a noticeable fashion in certain situations. Overall, however, the activated areas in (a) do not change much compared to the threshold map for randomly rotated dendritic trees in (c).

were observed in the boundary between the top of the postcentral gyrus and the sulcus. However, the coil dependency in the threshold maps did not change and thus the L5

PNs toward the postcentral gyrus were activated consistently. Compared to the percentage of excited L5 PNs with randomly rotated dendritic trees (16.12% as shown in Figure 4.5), the fixed orientation of dendritic trees induced changes in the fraction of activated neurons of up to 2%. The threshold variations in the L3 PNs were hardly noticeable compared to those of the L5 PNs. The percentage of excited L3 PNs was 26.4% with randomly rotated dendritic trees, and when the orientations of dendritic trees were fixed it resulted in changes of at most 0.3%. Thus, we found that the morphology of the dendritic tree of the L5 PN model had a bigger impact than that of the L3 PN model, possibly due to its greater lack of rotational

symmetry. Overall, however, rotations of the dendritic trees around the axis defined by the apical dendrite did not alter the spatial extent of activated regions much.

4.4 Discussion

The detailed mechanisms through which TMS activates cortical cells and cortical circuits are still not fully understood. In this study, we used multi-scale computational modeling to predict cortical activation as a function of coil orientation in two different ways. First, we simply considered the strength of the component of the TMS-induced electric field that is orthogonal to the gray matter surface as suggested by the C^3 -model^{73,141}. Second we developed a detailed computational modeling approach that combined an anatomically realistic head model with complex multi-compartment neuronal models of L5/L3 PNs and quantified their stimulation thresholds. A major finding was the characterization of the induced electric fields and the thresholds of L5/L3 PNs as a function of coil orientations as shown in Figure 4.4. In addition, threshold variations according to different morphologies of PNs were observed.

The magnitude of the electric field was considered first, because the strength of the electric field is commonly used to extrapolate neuronal activation^{19,55,78}. We found that the magnitude of the TMS-induced field is focused on the top of the gyrus, which is in agreement with previous modeling studies^{41,73,77,129}. However, the electric field magnitude showed little dependency on coil orientation⁷³. Then, we investigated the directional electric field, especially the orthogonal component that is perpendicular to the cortical surface, as this has been suggested to contribute most to the TMS-induced activation according to the C^3 -model^{73,141,143}. We found a strong dependence of the orthogonal field component on coil orientation, as shown in Figure 4.3. In contrast to the electric field magnitude, the highest field values were found in the sulcal walls and never on the apex (or crown) of the gyrus.

While the analysis of TMS-induced electric fields has been widely addressed in the past, the incorporation of multi-compartment neuronal models has hardly been investigated. To permit a more detailed understanding of the biophysical mechanisms of TMS, a few previous modeling studies employed detailed neuronal models and calculated the membrane potential dynamics generated by the electromagnetic field.

However, these attempts had various limitations. First, in early studies no anatomical information on large-scale brain morphology was applied^{51,54,62}. Rather than constructing a finite element head model, these studies applied a uniform electric field to the neuronal model. Even though such investigations achieved reasonable results regarding the neuronal activation, they did not consider the effects of the complex folding patterns of the cortex and the effects of tissue borders such as the borders between GM on the one hand and CSF or WM on the other hand. However, the importance of anatomically realistic head models has been shown convincingly^{41,77,129}. Furthermore, the impact of detailed brain anatomy has been considered in various methods of brain stimulation and substantial differences have been demonstrated by improving anatomical information related to the head model^{48,59,80,95}. Salvador et al. (2011) investigated neuronal responses using a simplified head model of a cortical sulcus with several types of neurons and found changes of the stimulation threshold depending on the pulse waveform and the coil orientation¹³⁵. However, the used head model had an approximated geometry restricted to the motor cortex and a full complex geometry, such as the hook-shaped hand knob, was not considered. Furthermore, the modeled coil orientation was limited to anterior to posterior and its reversal due to the simplified geometry of the head model. Most recently, Goodwin and Butson (2015) proposed a more realistic approach that integrates an anatomically realistic head model derived from MR images with detailed neuronal models⁹⁴. They considered the excitability of neurons as a function of coil orientation. However, in contrast to our results, excitability maps hardly showed a systematic dependence on coil orientation and activation thresholds were lower in the gyral crown. We speculate that this might be caused by the different morphology of PNs or the different way in which they calculated the external currents to simulate neuronal responses. Also, we considered two types of L3/L5 PNs spread over a wider region of the cortex. Finally, we also established the site of action potential initiation and found that most PNs are activated at the axon initial segment and action potential initiations at other parts of the neuron are comparatively rare.

The threshold maps we calculated demonstrate acute sensitivity to coil orientation, but different spatial extents were observed according to the different morphologies of the PNs. In L5 PNs, activation thresholds were low in the sulcal walls, matching predictions based on the orthogonal component of the electric field. The excitation in the sulcal cortical surface was consistent with the well-established columnar neuronal orientation and functional organization of the cortex and functional imaging studies^{141,144}.

Furthermore, the excitable area of the L5 PNs were wider in the postcentral gyrus compared to the precentral gyrus. This might be due to the severe curvature in the precentral gyrus or the thinner cortex on the postcentral side such that the neurons were smaller than those in precentral gyrus. This suggests an additional important factor of cortex geometry for TMS next to neuron placement and coil orientation¹. The L3 PNs had different morphology with shorter axons than the L5 PNs such that they were located completely within the gray matter. Similar to the L5 PNs, the coil orientation had a significant impact on the responses of the L3 PNs, but the precise patterns of the threshold maps differed between the L3 and L5 PNs. As hypothesized by Day et al., here the proximity to the coil played an important role¹⁴⁵, as L3 PNs in the gyral crown and the upper parts of the sulcal wall were predominantly activated.

The neural response to TMS is composed of a direct (D) and several indirect (I) waves. The D-wave is thought to be produced by direct activation of L5 PNs as we have modeled it here and is followed by I-waves that are thought to be generated by synaptic excitation and/or re-excitation of L5 pyramidal cells with longer latencies^{126,145}, presumably via pyramidal cells in superficial cortical layers L2 and L3. According to Di Lazzaro et al. (2004), at the lowest stimulation intensity to evoke neuronal responses, an I-wave is elicited, and with increasing stimulation intensity, the earlier, small D-wave is produced¹. This indicates that thresholds for eliciting I-waves are lower than those for eliciting D-waves¹¹⁵. In this work, we explored the excitation thresholds of both L3 and L5 PNs and found that the percentage of excited neurons for a stimulation intensity at the motor threshold was about two times higher for L3 PNs than for L5 PNs. Furthermore, the activation of the L3 PNs was consistently higher than that of the L5 PNs for the full range of stimulation intensities. The lower stimulation thresholds of the L3 PNs are consistent with lower stimulation intensities required to produce I-waves^{57,146}, and the higher stimulation intensities required to produce D-waves.

The highest percentage of excited PNs was observed at +135 degrees and the excited regions were focused on the postcentral gyrus. The base coil orientation induced the lowest percentage of activated PNs, but as shown in Figure 4.4 the precentral gyrus was targeted better than for other coil orientations. Thus, to activate the precentral gyrus, the base coil orientation is recommended by our model, congruent with previous research^{147,148}, and +135 degrees should be ideal to stimulate the postcentral gyrus.

The question of the precise initiation site of action potentials is a central issue for understanding the

physiological effects of TMS. According to our study, the dominant initiation site leading to action potentials is the axon initial segment in both L5 and L3 PNs. This is consistent with previous studies arguing that action potentials giving rise to the D-wave might be initiated close to the soma and/or axon initial segment^{149,150}. In addition, L5 PN action potentials were also initiated at the axon where it crosses the boundary between gray matter and white matter, where tissue conductivity changes abruptly¹¹⁷. However, it will be important to verify these results with more realistic axon models.

There are several limitations in our modeling study. A first limitation is related to neuronal properties and morphologies. The L3 and L5 PNs were taken from cat visual cortex due to the lack of models for most human cortical cell types. However, despite the uncertainty with regard to properties of PNs, we produced results matching both experimental studies and other computational studies^{51,62} that incorporated the same models of PNs.

While we observed the stimulation of neural activity in the superficial cortex nearby the coil, TMS might also affect deep brain areas that cannot be stimulated directly. This can be explained on the basis of the propagation of action potentials along white matter fiber tracts. Recent studies modeled tractography-based white matter fiber tracts using diffusion tensor imaging (DTI) and observed activation of axon bundles^{47,77,128}. Compared to fiber tracts in previous modeling, we modeled straightly stretched axons of L5 PNs inside the WM. Due to such limitations, the axons inside the WM occasionally passed through protruding parts of GM. Notwithstanding this intersection could affect the neuronal responses such as the action potential initiation or thresholds, most PNs initiated action potentials at the axon initial segment and coil orientation dependency observed in threshold maps was consistent with observations in previous studies. Further developments in tractography may improve detailed neuronal models and may lead to a deeper understanding of the TMS-induced brain activity propagations from the superficial cortex to distant brain regions.

Another limitation is that the reconstructed PNs were synaptically isolated. For the L5 cells this means that we basically studied the generation mechanism of D-waves. The activation of L3 cells could be seen as a proxy for the generation of I-waves. A logical next step is to synaptically couple L3 and L5 cells as done in a recent model for the generation of D and I-waves using L5 PNs that were contacted by a pool of excitatory and inhibitory layer 2 and 3 neurons⁵⁷. This model successfully reproduced various characteristics of I-waves and highlighted the importance of the complex morphology of the L5 PNs for the generation of I-

waves. An improvement would be to use the anatomical information on the activation of PNs as modeled here, as we found a clear difference in the threshold maps for L5 and L3 PNs based on their morphology. Therefore, in future work, we plan to incorporate synaptic connections between L3 and L5 PNs. We hope that this will bring us one step closer to a detailed understanding of the mechanisms through which TMS activates cortical circuits, paving the way for more precise and effective application of TMS based on individual brain morphology in clinical and basic research settings.

V. Effect of a Transcranial Channel as a Skull/Brain Interface in High-Definition Transcranial Direct Current Stimulation—A Computational Study

5.1 Introduction

To achieve intense and focused neuromodulation with minimal invasiveness, Wingeier et al. introduced a transcranial channel combined with tDCS.¹⁵¹ A transcranial channel acts as an interface through the thickness of the skull to deliver current induced by tDCS into the targeted area. Implanted in the patient's skull, it is made of biocompatible and highly conductive materials. To lower the risk of infection, it does not breach the extradural space. It has various designs, including an I-shaped cylindrical channel (shaft) and a T-shaped channel (shaft with hat), among others. However, this transcranial channel has only been proposed conceptually, and to date there has been no concrete study of its efficacy. Thus, it remains unknown how well a transcranial channel improves the efficiency of brain stimulation in the underlying cellular mechanisms.

In this study, we investigated the effects of a transcranial channel by combining HD-tDCS, using a computational study that allowed a cost-effective prediction of the influence of brain stimulation.^{21,130,152–155} The spatial extent of stimulus-induced EF has been estimated in computational studies with the assumption that the EF magnitude is correlated with the modulation of cortical excitability.^{19,23,24,45,46} However, it cannot reflect stimulus-evoked neuronal polarization, which is dependent on target neuronal morphology, location, and EF orientation.^{55,56,117} We incorporated compartmental models of pyramidal neurons (PNs) into an anatomically realistic volume conduction head model, and then investigated the way in which implantation of a transcranial channel modulated cortical excitability. We focused on stimulus-induced membrane polarization in two kinds of pyramidal neurons (PN), layer 5 (L5) and layer 3 (L3).

Our objective was to investigate the influence of the inclusion of a transcranial channel, its shape (I- or T-shaped), and displacement of the tDCS electrode relative to the transcranial channel. This study may be the first step in assessing the use of a transcranial channel combined with HD-tDCS, which may confirm its efficacy for clinical use.

5.2 Methods

5.2.1 The volume conduction model of an anatomically realistic head

We developed a volume conduction model of an anatomically realistic head for HD-tDCS using human magnetic resonance imaging (MRI), following SimNIBS pipeline⁴¹ (Figure 5.1(a)). We note that this human MRI data is example dataset provided by SimNIBS under the ethical approval⁴¹. The model was segmented by the white matter (WM), gray matter (GM), cerebrospinal fluid (CSF), skull, and scalp, respectively. Dura mater was made artificially by deleting 0.5 mm¹⁵⁶ of the boundary between the CSF and skull layer based on the assumption that it was mapped to the skull layer.^{157,158} Then, we constructed disc-type electrodes (height = 1 mm; radius = 4 mm) to form a 4×1 HD-tDCS electrode montage with the “active” center electrode on the target hand knob in the precentral gyrus,¹¹⁴ and with four “return” electrodes positioned in a circular fashion.²³ CCNY-4 gel (height = 2 mm; radius = 4 mm) was modeled between the scalp and the electrodes. Thereafter, two types of transcranial channels were designed, one an I-shaped channel with a shaft only, and the other a T-shaped channel that consisted of a shaft with a hat. These transcranial channels were designed to traverse the entire thickness of the skull (Figure 5.1(b)). The diameters of the shaft varied from 1 to 9 mm and we set the diameter of the hat to the shaft diameter + 1 mm.

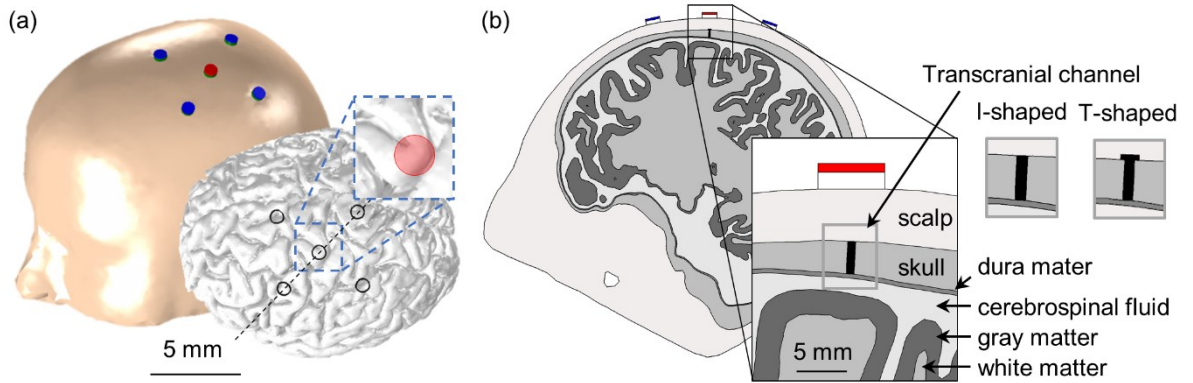


Figure 5.1. The shape of the anatomically realistic head model. Electrodes were placed (a) overlaying the head (left) and brain (right). The red circle in the right inset represents the ROI on the hand knob. The cross-sectional view along the black dotted line is illustrated (b) and shows the two types of transcranial channels.

3D-optimized tetrahedral volume mesh was constructed from the surface mesh using iso2mesh¹⁰¹

and tetgen.¹⁰² There were approximately 18 million total tetrahedral elements, with far smaller elements distributed around the electrode, transcranial channel, and regions of interest (ROIs) in the precentral gyrus; element size ranged from an average of 0.0043 mm³ (in the transcranial channel) to an average of 1.25 mm³ (in the skull). The electrical conductivities of the compartments were set to isotropic values (in units of S/m):^{37,53,61,108} scalp, 0.465; skull, 0.01; dura mater, 0.065; CSF, 1.65; GM, 0.276; WM, 0.126; gel, 0.30, and electrode, 5.80e.7 In this paper, we considered the transcranial channel made of titanium with the conductivity of 7.40e5 S/m, because it is a biocompatible material used commonly as a skull plate.¹⁵⁴ The Laplace equation was solved with the boundary conditions—the exposed surface of the active electrode was set to 1 mA inward current, those of the return electrodes were set to ground (-0.25 mA for each return electrode), and all other external boundaries were set to be insulated. We used the linear system solver of the conjugate gradient method with a relative tolerance of 1×10^{-9} in COMSOL Multiphysics 5.2 (Comsol Inc, Massachusetts).

5.2.2 The compartmental model of pyramidal neurons

We constructed two kinds of compartmental models, L5 and L3 PNs. Their morphology and electrical properties were taken from the cat visual cortex.¹¹⁰ Furthermore, to investigate the robustness of the estimated polarizations for the neuronal morphology, we adapted two established L5 PNs additionally that were composed by different morphologies (illustrated in Figure 5.8(a)).^{90,159} The same compartment composed of axons and electrical properties were applied. The PNs were lengthened following the irregular dimensions of the cortex to reach the dendritic trees to layer 1.^{61,112} Simulations for the compartmental models of PNs were performed in the NEURON environment.¹¹¹

L5 and L3 PNs were coupled indirectly within the hand knob (Figure 5.1(a)) in the anatomically realistic head model (for details, see Seo et al.^{58,59}). Because PNs are oriented perpendicular to the cortex,^{47,160,161} we set the neuronal orientation perpendicular to the brain surface, with boundary elements between CSF and GM, and the axons of L5 PNs were curved beyond the boundary between the GM and WM.^{53,58,61,63} We constructed L5 and L3 PNs (2137 numbers of PNs each), and then applied the stimulus-induced potential fields distributed in the anatomically realistic head model at each center point of the compartmental models of PNs by extracellular stimulation. As complex membrane polarization was evoked

according to neuronal morphology and orientation relative to the induced EF,^{55,56,162} we investigated a range of steady-state membrane polarizations in each compartment (dendrites, soma, initial segment, and axons) of the L5 and L3 PN. To investigate the focality and intensity of the target area we analyzed the median value of polarization and their deviations in pre-selected ROI, where it is directly under the center electrode, as shown by the red circle in Figure 5.1(a). This process was implemented in MATLAB (MathWorks, Natick, MA, USA) and COMSOL 5.2 with MATLAB.

5.3 Results

5.3.1 Effects of varying the dimension of the transcranial channel

For each configuration of the transcranial channel, we calculated the EFs induced and the membrane polarizations in the brain. The shaft diameter of the I- and T-shaped channels increased from 1 to 9 mm. First, we calculated the peaks of induced EF (Table 1) and found that implantation of the transcranial channel induced 3.3 to 10.3 times greater peak EFs than did the conventional HD-tDCS without the transcranial channel. As the diameter of the shaft increased, the stimulus-induced peak EF increased in diameter by up to 7 mm; however, we observed reduced peak EFs in both the T- and I-shaped models with a shaft diameter of 9 mm. Similar peak EFs occurred in both types of transcranial channels, although the T-shaped channel induced slightly higher EFs than the I-shaped channel.

Second, in order to measure the relative focality (Table 1), we calculated the volume of the cortex, where EFs were greater than 50%, 60%, 70%, or 80% of the peak EF values, respectively. The area with the highest EF magnitude (Vol80) was smaller in the conventional HD-tDCS without the transcranial channel compared to that of the transcranial channel. Higher EF (Vol50-70) was distributed more widely in the conventional HD-tDCS, while the transcranial channel helped capture it. Thus, the transcranial channel resulted in higher relative focality than did the conventional HD-tDCS, with the smaller area higher than 50% to 70% of the peak EF. Within the HD-tDCS configurations with the transcranial channel, the relative focality decreased as the diameter of the shaft increased, because the larger area of the transcranial channel conveys the stimulus-induced EF to the extended target area.

Table 5.1. Variation in the stimulus-induced EF within the brain with increments in the shaft diameter of the T- and I-shaped channels. The conventional HD-tDCS without the transcranial channel is compared. The peak EF magnitude (V/m) and cortex volumes in excess of 50%, 60%, 70%, or 80% of the peak EF magnitude (Vol50, Vol60, Vol70 and Vol80 (mm³)) were observed. Note the conventional HD-tDCS has a lower peak EF value and lower relative focality compared to that with the transcranial channel.

Channel Type	Shaft diameter	Peak EF (V/m)	Vol ₅₀	Vol ₆₀	Vol ₇₀	Vol ₈₀
Conventional HD-tDCS		0.30	1538.20	366.99	19.74	0.17
T-shaped Channel	1 mm	0.99	12.02	5.02	2.05	0.54
	3 mm	2.53	12.78	5.78	2.42	0.70
	5 mm	3.35	22.81	10.19	3.78	0.87
	7 mm	3.40	52.98	23.87	8.69	1.76
	9 mm	3.09	92.19	41.11	16.68	5.27
I-shaped Channel	1 mm	0.88	13.49	5.45	2.22	0.58
	3 mm	2.28	13.04	5.88	2.46	0.70
	5 mm	3.10	23.04	10.28	3.79	0.88
	7 mm	3.26	53.22	23.92	8.71	1.76
	9 mm	2.97	92.60	41.23	16.72	5.29

To further assess the way in which the transcranial channel improved the efficacy of stimulation, we presented spatial distributions of EFs between the conventional HD-tDCS with and without the T-shaped transcranial channel and set the channel diameter to 7 mm as it showed maximum peak EF. We focused the T-shaped channel due to I- and T-shaped channels showed comparable distributions of EFs. As shown in Figure 5.2, EF distributions depended upon whether or not the inclusion of the transcranial channel was considered, and which type of channel was incorporated. The conventional HD-tDCS resulted in a 0.3 V/m peak with an extensive EF distribution from the pre- to post-central gyri, while the inclusion of the transcranial channel increased peak EFs focused on the hand knob 10.3 fold in the T-shaped channels. In addition to EFs, the magnitudes of tangential (parallel to the cortical surface) and radial (perpendicular to the cortical surface) components of EFs are visualized (2nd and 3rd columns in Figure 5.2). Tangential component was estimated by the cross product of normal vector of the cortical surface and the EFs; radial component was estimated by the dot product of normal vector and EFs. We found that radial field was

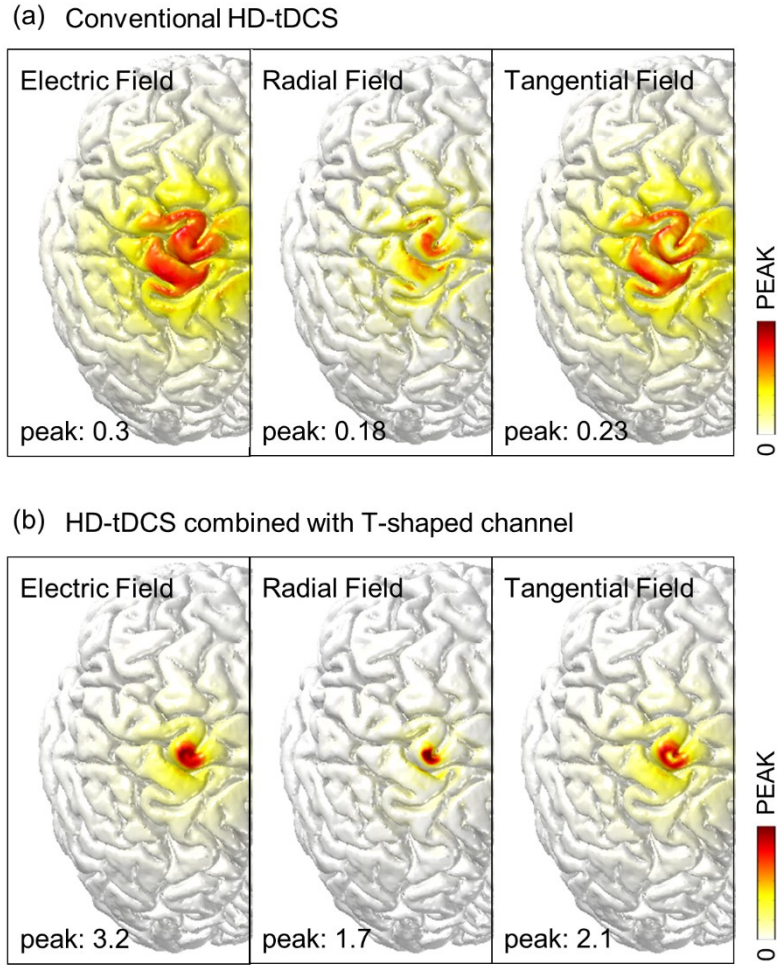


Figure 5.2. Distribution patterns of stimulus-induced EFs decomposed into radial and tangential fields on the cortical surface. Comparison of the conventional HD-tDCS without the transcranial channel (a) and with implantations of the T- shaped transcranial channels at the channel diameter of 7 mm (b); the color density scale is adjusted according to the maximum value of the EFs.

highest in the top of hand knob where is directly under the active electrode, whereas the highest values of tangential field appeared toward the sulcus.

The excitability of the L5 and L3 PNs was then simulated in the region of interest (ROI) with 5 mm radius in the middle of the hand knob, where the top of the precentral gyrus is directly under the active electrode, over varying transcranial channel diameters. We analyzed the distributions of membrane polarization and induced EF in ROI. Note that the electric field flowed directed inward to the ROI, because

ROI was a small area and located directly under the active electrode. Figure 5.3 shows simulated steady-state membrane potentials of L5 and L3 PNs, which include the soma, axon initial segment, bend, terminal, node crossing the gray matter (GM) and white matter (WM) boundary, and some dendrite points. PNs with a non-symmetric dendritic morphology were modulated by the polarity and orientation of the EF, and thus dendrites might have complex polarization patterns.^{55,115,162} In this study, we identified some dendritic trees that suggest membrane depolarization or hyperpolarization according to their position. We found that the maximum polarization increased in the upper part of the dendrites and axon terminal as the channel diameter increased, and that the rate of increase in polarization with increasing channel diameter decreased, so that polarization at the channel diameter of 9 mm was comparable to that at the diameter of 7 mm compared to other configurations. However, the somatic polarization and other compartments show a similar tendency in peak EF behavior, i.e., they increased marginally by up to 7 mm and then decreased slightly at the 9 mm diameter. Overall, as we observed in previous results, the I-shaped transcranial channel (not shown) shows a comparable and slightly lower mean and maximum value of polarization than did the T-shaped channel. Generally, the dendrites' upper parts were hyperpolarized, and the soma's lower parts were depolarized; the transcranial channel amplified this polarization. The peak somatic polarization in L5 PNs for the transcranial channel with 7 mm shaft diameter (that induced maximum somatic polarization) was approximately 11 times higher than without the transcranial channel, and, similarly, we observed a 12-fold increased peak somatic polarization in the L3 PNs when the transcranial channel was incorporated. A smaller deviation was observed in the conventional HD-tDCS without the transcranial channel, indicating relatively uniform distributions of membrane polarization and induced EF within the ROI. The HD-tDCS with the transcranial channel had focused EF distributions under the transcranial channel and then induced EF might be decreased rapidly. Thus, we observed greater variation in membrane polarization in accordance with induced EF.

For further observations, we visualized the spatial distributions of L5 and L3 PNs polarizations focused on the ohm-shaped hand knob (the target area, as illustrated in Figure 5.4(a)). The T-shaped transcranial channel with 7 mm channel diameter was considered and compared to conventional HD-tDCS without the channel (Figure 5.4). We compared the spatial extents of polarization with the magnitude of the radial component of EFs, because the stimulation might contribute to neural activation when the EFs are perpendicular to the cerebrospinal fluid (CSF) and GM boundary.^{141,143,144} In Figure 5.4(b), the positive value

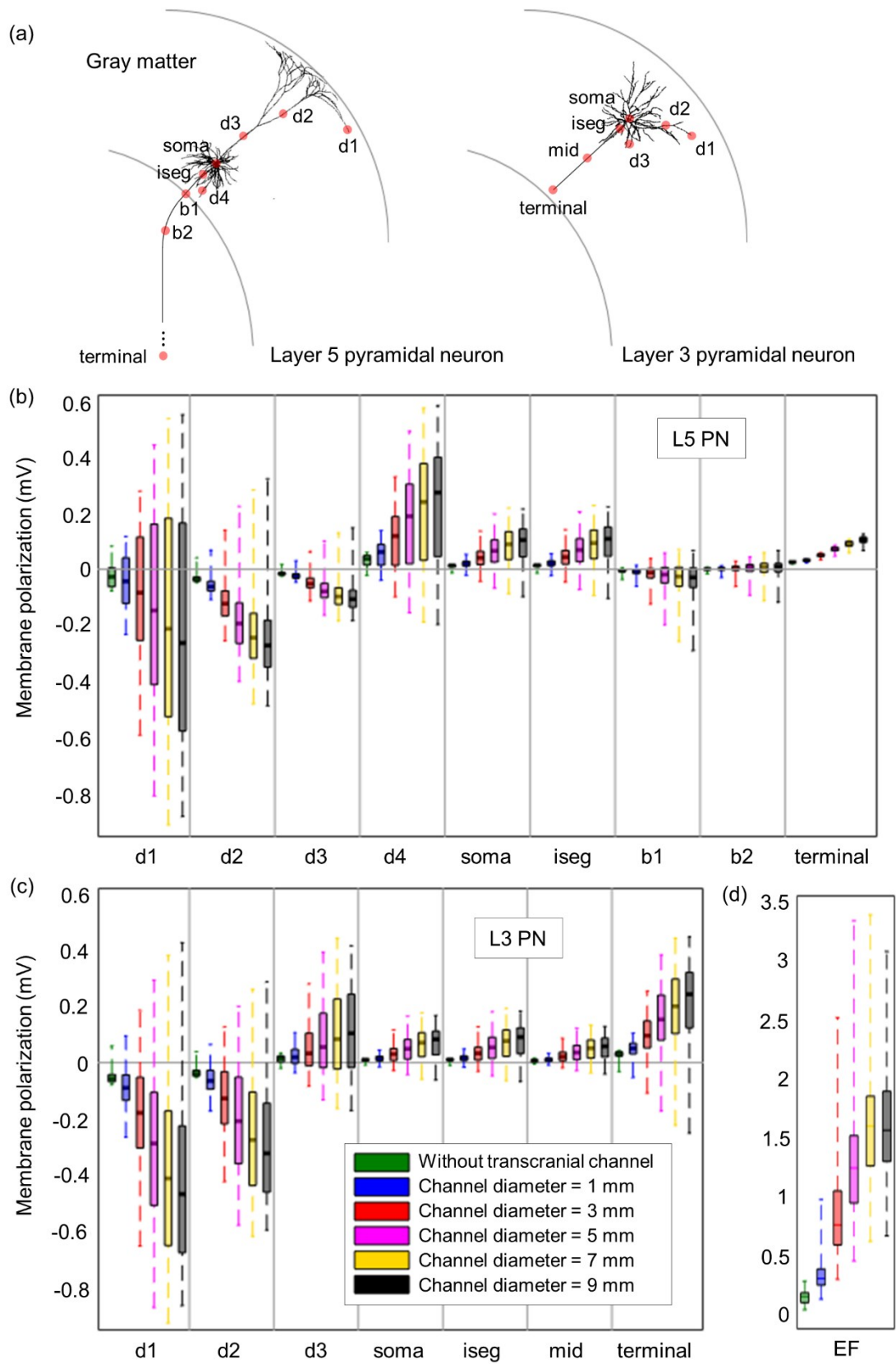


Figure 5.3. Membrane polarization for neuronal compartments in L5 and L3 PN with various diameters of the T-shaped transcranial channel. To investigate the impact of focal and intense stimulation, we focused membrane polarizations of PNs in the region of interest (ROI) with 5 mm radius in the middle of the hand knob, where it is directly under the center electrode, and thus total 112 numbers of L5 and L3 PNs were analyzed. Membrane potentials are examined in each compartment and indicated by red dots on the neuronal morphology (a); in L5 PNs, we simulated membrane potentials at four dendrites (d1, d2, d3, and d4), the soma, initial segment (iseg), axon at the boundary between GM and WM (b1), bent area (b2), and terminal. In L3 PNs, we examined three dendrites (d1, d2, and d3), the soma, initial segment (iseg), middle (mid), and the terminal part of the axon. We then analyzed the membrane polarization (b and c) and induced EF (d) within the given ROI by the median and the first to third quartiles spanning the central rectangles, and whiskers indicate maximum and minimum values.

(red) indicates directed inward and thus most current flows through the top of the gyrus. The polarization maps for the dendritic trees, soma and axon initial segments (not shown but the axon initial segment shows consistent spatial distributions with the soma) also have similar patterns with the radial field. The upper parts of the dendrites (d2 for L5 and L3 PNs) were hyperpolarized while the lower parts of the dendrites (d4 for L5 PNs and d3 for L3 PNs) were depolarized. The axons for L5 PNs induced complex polarization patterns compared to the somatic polarizations. The L3 PNs have consistent polarization distributions for all compartments, which might be due to the restricted dimension of L3 PNs within GM.

Even though the transcranial channel increased the magnitude of induced EFs, the polarizations were restricted to the top of the hand knob and did not extend to the sulcus. To interpret this, we focused on how the transcranial channel affected the EF decay with the cortical depth by the distribution patterns of EFs on the cross-section view (Figure 5.5). We found that the transcranial channel could improve the magnitude of EFs but that the channel did not allow the EFs to flow deeper due to the narrow width of the sulcus (only slight changes were observed). We then shifted the electrodes and the channel to target the deeper area of the central sulcus. The highest field magnitudes were located at the curvature of the gyrus in both precentral and postcentral gyrus (Figure 5.6). By placing the transcranial channel to the sulcus, the stimulus-induced polarization (Figure 5.4(e)) showed comparable peak values and similar but shifted polarization patterns compared to the results induced by targeting the top of the gyrus, and it could not reach the bottom of the sulcus (see Figure 5.7 for the simulations of L3 PNs).

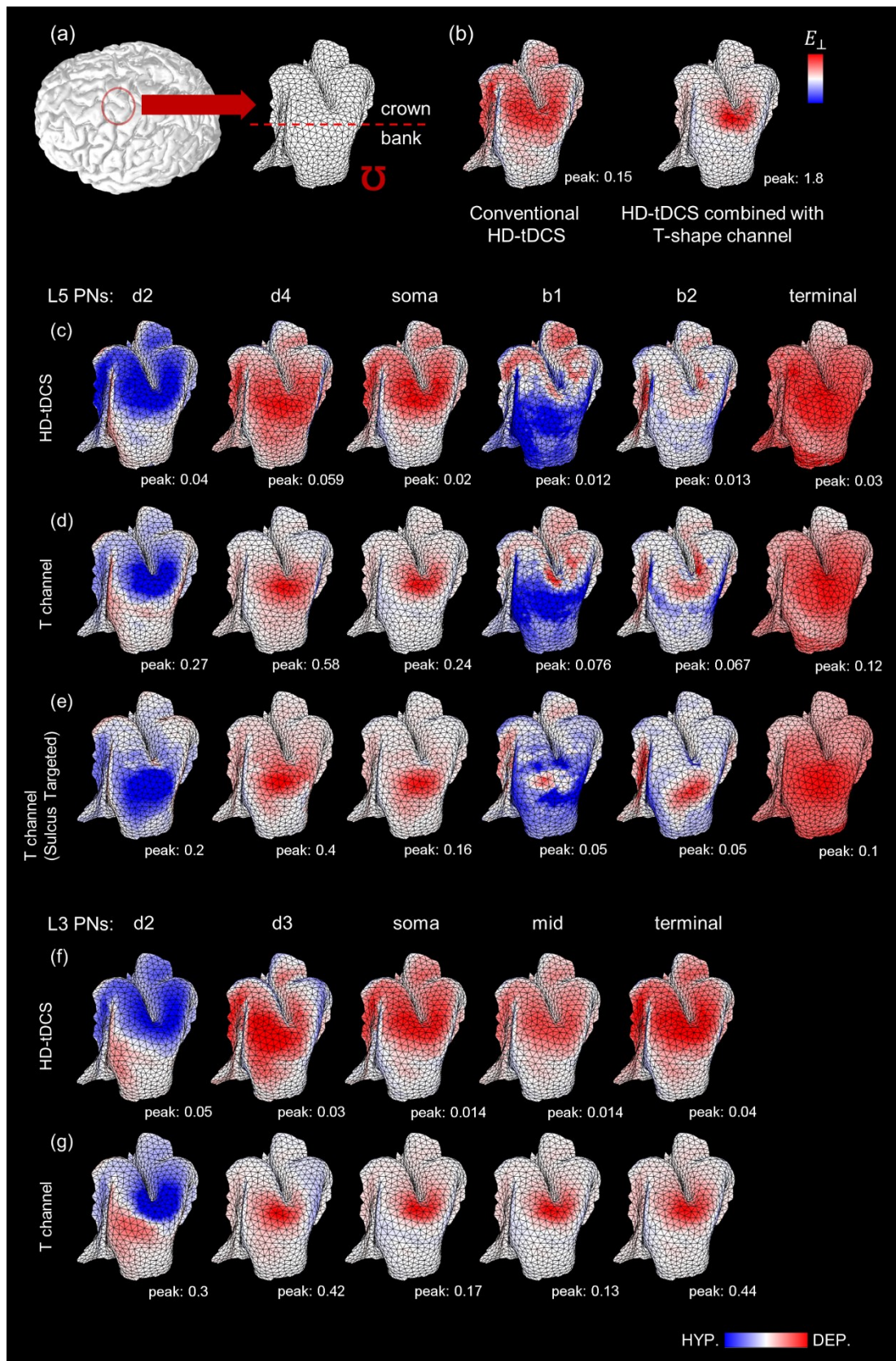


Figure 5.4 The spatial extent of membrane polarizations for L5 and L3 PNs focused on precentral gyrus. (a) We decouple the target area which is the ohm-shaped hand knob, and the crown indicates the top of gyrus and the bank is the wall of the sulcus. We observed how transcranial channel increases focality and intensity of stimulus-induced membrane polarizations compared to conventional HD-tDCS without T-shaped channel. We use two predicted neural responses of the EF strength perpendicular to the CSF-GM boundary (E_{\perp} , (b)) and polarizations at specific compartments (c-g). Interestingly, the spatial distributions for perpendicular component of EFs resembles the most polarization maps. Conventional HD-tDCS for L5 PN (c) and L3 PN (f) have quite diffused patterns of polarizations compared to the HD-tDCS combined with T-shaped channel for L5 PN (d) and L3 PN (g). (e) We further investigate the variations of polarizations by shifting target area from the top of gyrus to the sulcus. All color scale is adjusted according to peak values written by white color under each spatial extent.

To investigate the role of neuronal morphology in determining the stimulus-induced membrane polarization, we incorporated two established L5 PN (type 2 and 3, as shown in Figure 5.8(a)) that had different morphologies and same electrical properties were applied. We examined polarization profiles induced by HD-tDCS with T-shaped transcranial channel set to a diameter of 7 mm. Figure 5.8(a) shows polarization profiles of the dendritic trees of L5 PN directly under the transcranial channel. Similar polarization patterns were observed, with hyperpolarization observed in the upper parts of the dendrites corresponding to the dendrite depolarization positioned below the soma. Figure 5.8(b) illustrates the spatial distributions of polarization and the color scale is adjusted to the peak values induced by type 1 PN for absolute comparison. The somata of type 2 and 3 PN had 2.5-3 times higher peak values of polarizations compared to type 1 PN and thus they induced somatic depolarization in wider regions (red in Figure 5.8(b)). The magnitudes of axonal polarizations were slightly changed according to different PN morphologies but the spatial patterns did not alter. In addition, we found similar observations for the conventional HD-tDCS without the transcranial channel with increased somatic polarization with type 2 and 3 PN compared to type 1 PN.

Furthermore, we analyzed the cell-specific somatic coupling constant (mm) to define sub-threshold sensitivity, which is the somatic membrane polarization (mV) per unit EF applied (mV/mm).^{55,56,162} In the conventional HD-tDCS without the transcranial channel, the mean and standard deviations of the somatic coupling constant were 0.0784 ± 0.0384 mm in L5 PN, and 0.0495 ± 0.0194 mm in L3 PN, respectively. In the case of the transcranial channel, there were nominal variations in the coupling constant among the same

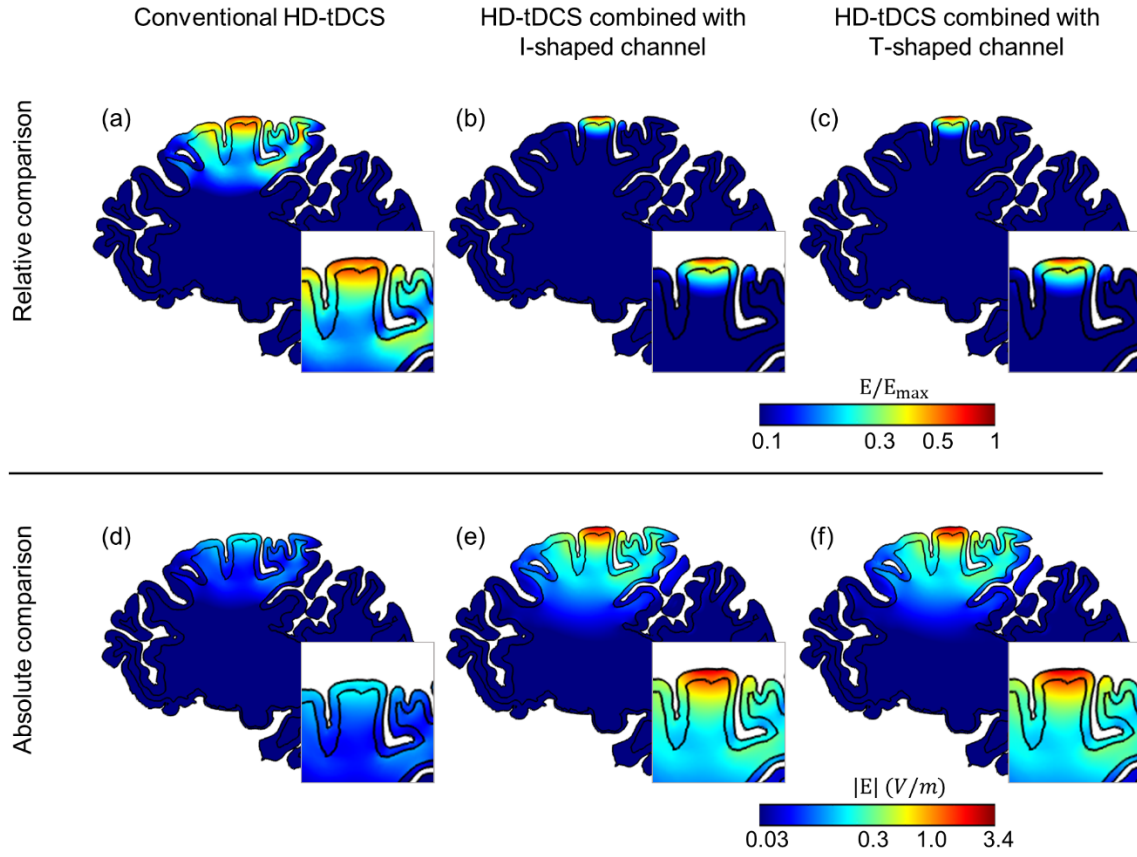


Figure 5.5 Distribution patterns of stimulus-induced electric fields on cross-sectional view. In (a)-(c), the color density scale is normalized to each maximum value of electric fields. HD-tDCS with the transcranial channel induces higher electric fields focalized on the top of gyrus, while conventional HD-tDCS without the transcranial channel has diffused patterns of electric fields. In (d)-(f), scale is adjusted to the maximum value of the electric fields induced by the T-shaped transcranial channel. The transcranial channel conveys the higher strength of stimulus-induced electric fields to the brain by reducing the shunting currents compared to the conventional HD-tDCS.

models of PNs. For the L5 PNs that have different morphologies, the somatic coupling constants were 0.0416 ± 0.1667 mm for type 2 and 0.0673 ± 0.2031 mm for type 3 PNs. The coupling constant was within the experimental range in Radman et al.,⁵⁵ and we found similar observations, in that the different morphologies of the PNs caused the different coupling constant. The notable morphological difference was that, compared to type 1 PNs, type 2 and 3 PNs had flat dendritic trees. When the somatic diameter was increased, the somatic polarization was decreased (Figure 5.9). This agrees with other modeling studies^{54,56,93} showing that different morphologies of PNs play a critical role in determining neural polarization. As shown in Figure

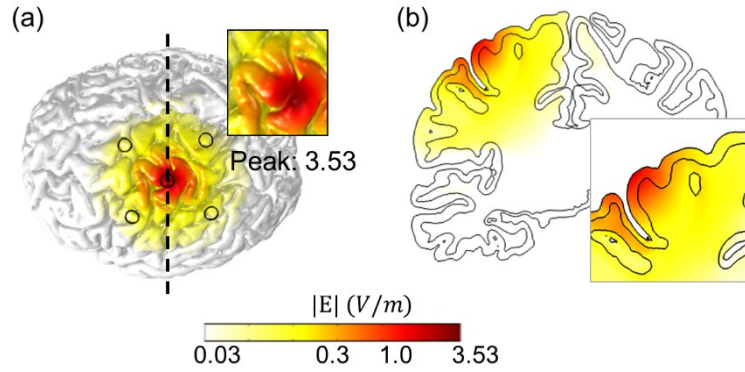


Figure 5.6 Distribution patterns of stimulus-induced EFs when the electrodes and T-shaped channel are shifted to target the central sulcus. In cortical surface view (a) and coronal slice view, the higher field strength of EFs are focused on the peripheral region of the sulcus.

5.8(b), we could estimate the consistent characteristics of polarization patterns regardless of varying morphology, such as those parts that might be depolarized or hyperpolarized.

5.3.2 Displacement of the electrodes from the transcranial channel.

Aligning the active electrode with the transcranial channel is difficult; even a small shift in the electrode may produce a substantial reduction in the stimulation effect in the target area. Therefore, it is essential to identify an acceptable range of electrode displacements relative to the transcranial channel. Accordingly, we investigated the influence of the displacement of the stimulus electrodes, while we fixed the transcranial channel to the target area. We focused on the T-shaped channel at 7 mm diameter, since it showed the most efficient stimulation effect.

Figure 5.10 presents the stimulus-induced EF distributions; the displacement of the center (active) electrode relative to the transcranial channel increased in increments of 5 mm and induced gradually decreasing peak EF values, as well as more diffuse EF distributions. Displacements of up to 5 mm maintained a relatively higher peak EF on the targeted hand knob; however, when the displacement reached approximately 20 mm, the EF magnitude decreased by up to 20% compared to the case with no displacement, and far more extensive spatial EF distributions were observed. Even the induced EF strength decreased as the displacement of the electrodes increased, and we found that the target area was stimulated consistently. Because stimulus-induced current flowed to the transcranial channel, it seemed to reach the target area even

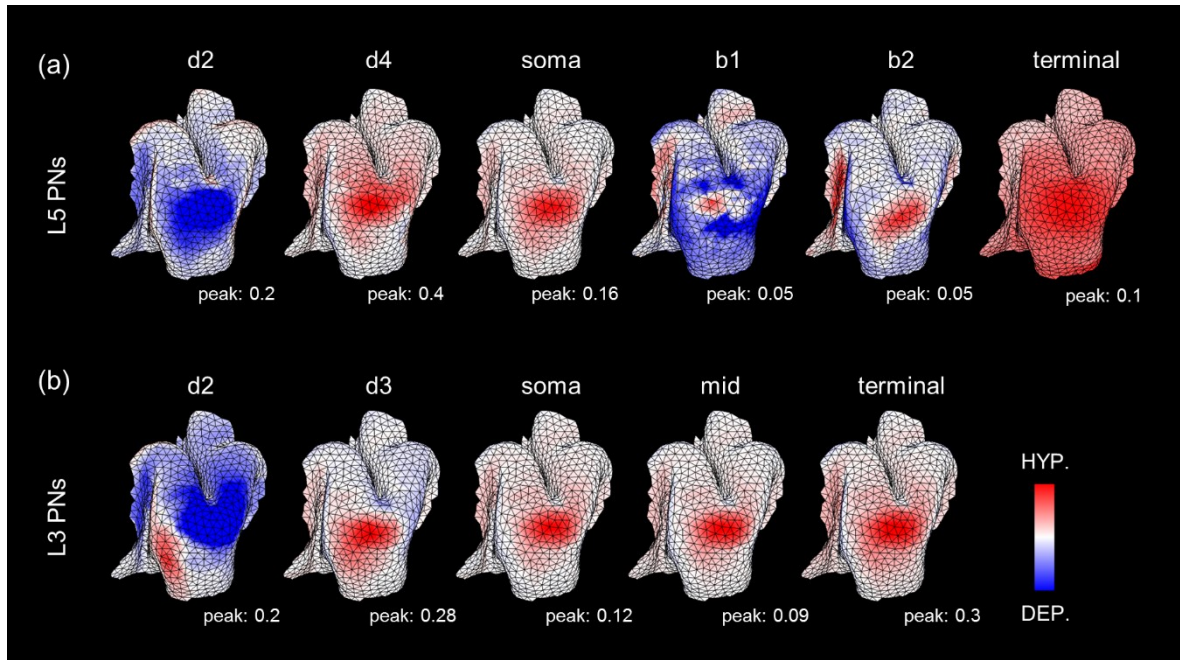


Figure 5.7 The spatial extent of membrane polarization for L5 (a) and L3 (b) PN models when the electrodes and T-shaped channel are placed above the central sulcus. PN models in the lip and upper part of bank along the sulcal wall are polarized.

when the electrodes were located far from that area.

As expected, the maximum value of the membrane polarization decreased in both L5 and L3 PN models (Figure 5.11) as the displacement of the center electrode from the transcranial channel increased. When the displacement of the center electrode was up to 5 mm in the postcentral gyrus, we observed that the peak somatic polarization dropped by up to 87% compared to no displacement (exact match between the center electrode and the transcranial channel). Furthermore, when the displacement increased to 10 mm, membrane polarizations in all compartments dropped to 60% or lower.

5.4 Discussion

The transcranial channel resembles an epidural peg or screw electrodes, which are used for intracranial recordings to map seizure foci.^{163–166} The epidural peg electrodes are flexible and mushroom-shaped, while the screw electrodes are tapered, and can be inserted easily and removed percutaneously.

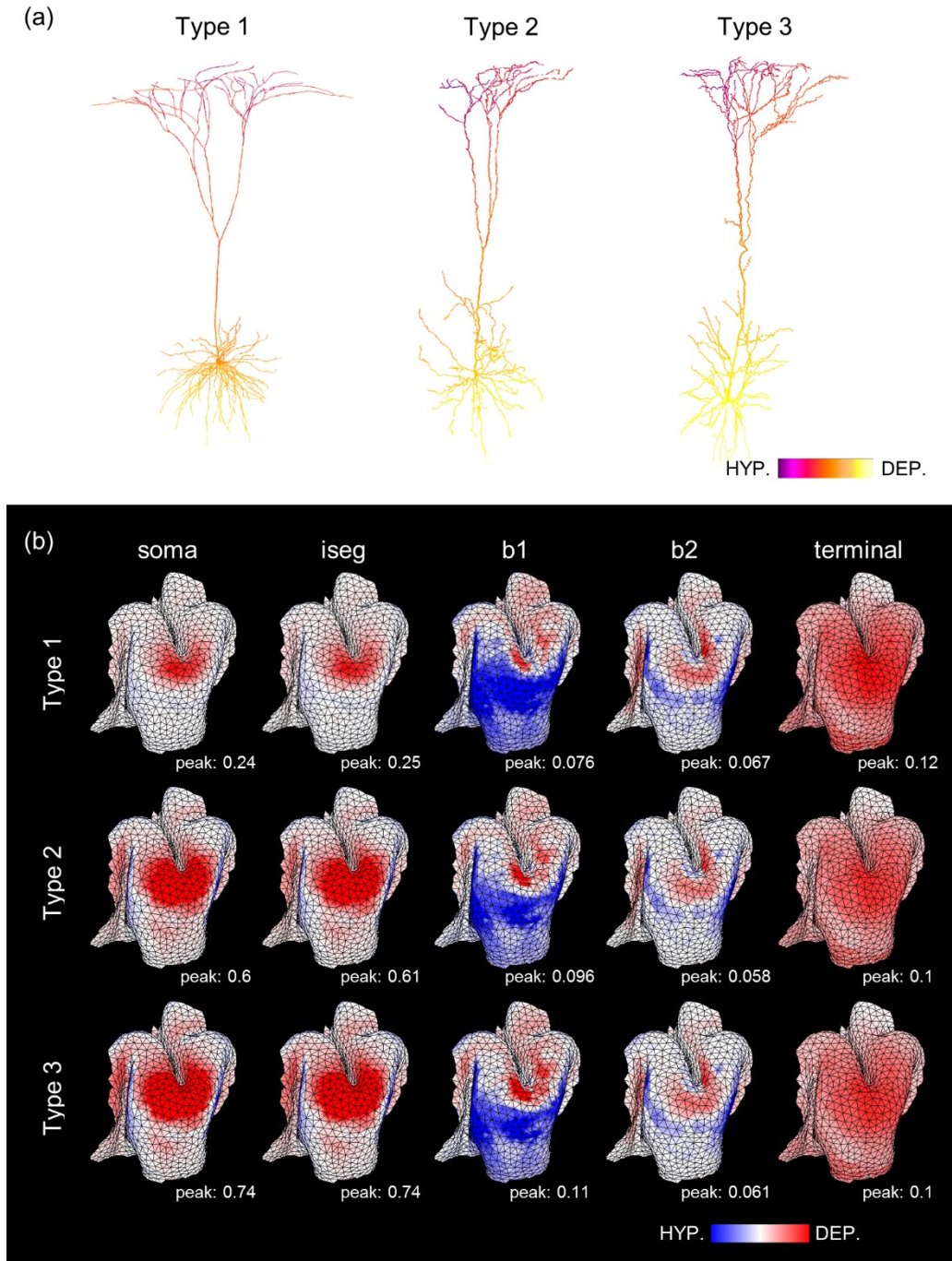


Figure 5.8. The impacts of morphology of L5 PNs on stimulus-induced membrane polarizations in the HD-tDCS combined with T-shaped transcranial channel. (a) Polarization profile illustrates with different morphologies. (b) The membrane polarization for L5 PNs focused on the precentral gyrus is measured at soma, axon initial segment (iseg), axon crossing boundary between GM and WM (b1), axon bending part (b2) and terminal; the color density scale is adjusted according to maximum value of the Type 1 PNs. Notable

differences according to different morphology are observed in soma and the axon initial segment with higher magnitude of depolarization in type 2 and 3 PN's compared to type 1 PN's.

Similar to the epidural peg and screw electrodes, the transcranial channel has the advantages, in that it does not require dissection of the epidural space, craniotomy, or a larger bur hole compared to the epidural strip. Therefore, it has lower risks of infection, hemorrhage and has enhanced patient comfort. Moreover, when the treatment is altered, such as a change in technique or target area, the implanted transcranial channel can be removed in the same way epidural pegs or screw electrodes are removed. Because the epidural screw electrode might permit easier insertion and removal compared to peg electrodes, which require twist-drilled skull holes,^{165,166} the improved design of the tapered screw for the transcranial channel should be considered. Another potential use of the transcranial channel might be to deliver electrical brain activity to measure electroencephalography (EEG), which could alleviate the fundamental limitation of a blurred signal attributable to the preferential flow of electrical current induced by brain activity through the intervening tissue.

Transcranial direct current stimulation (tDCS), which delivers a weak direct current (up to 2 mA) through electrodes on the scalp, has attracted considerable interest, as it is safe, inexpensive, portable, and simple to implement.^{19–22} It conveys a weak current that activates a relatively larger brain area, even in areas

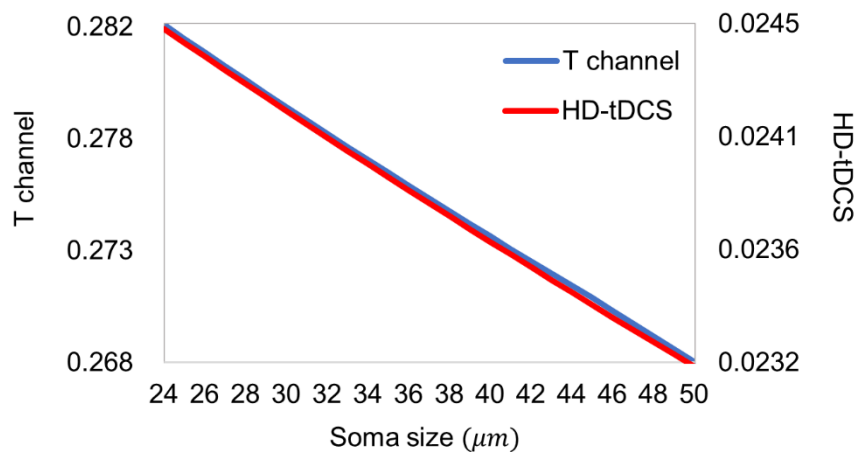


Figure 5.9 The relationship between somatic size and stimulus-induced polarization. The membrane polarizations as a function of somatic size in both HD-tDCS with and without transcranial channel.

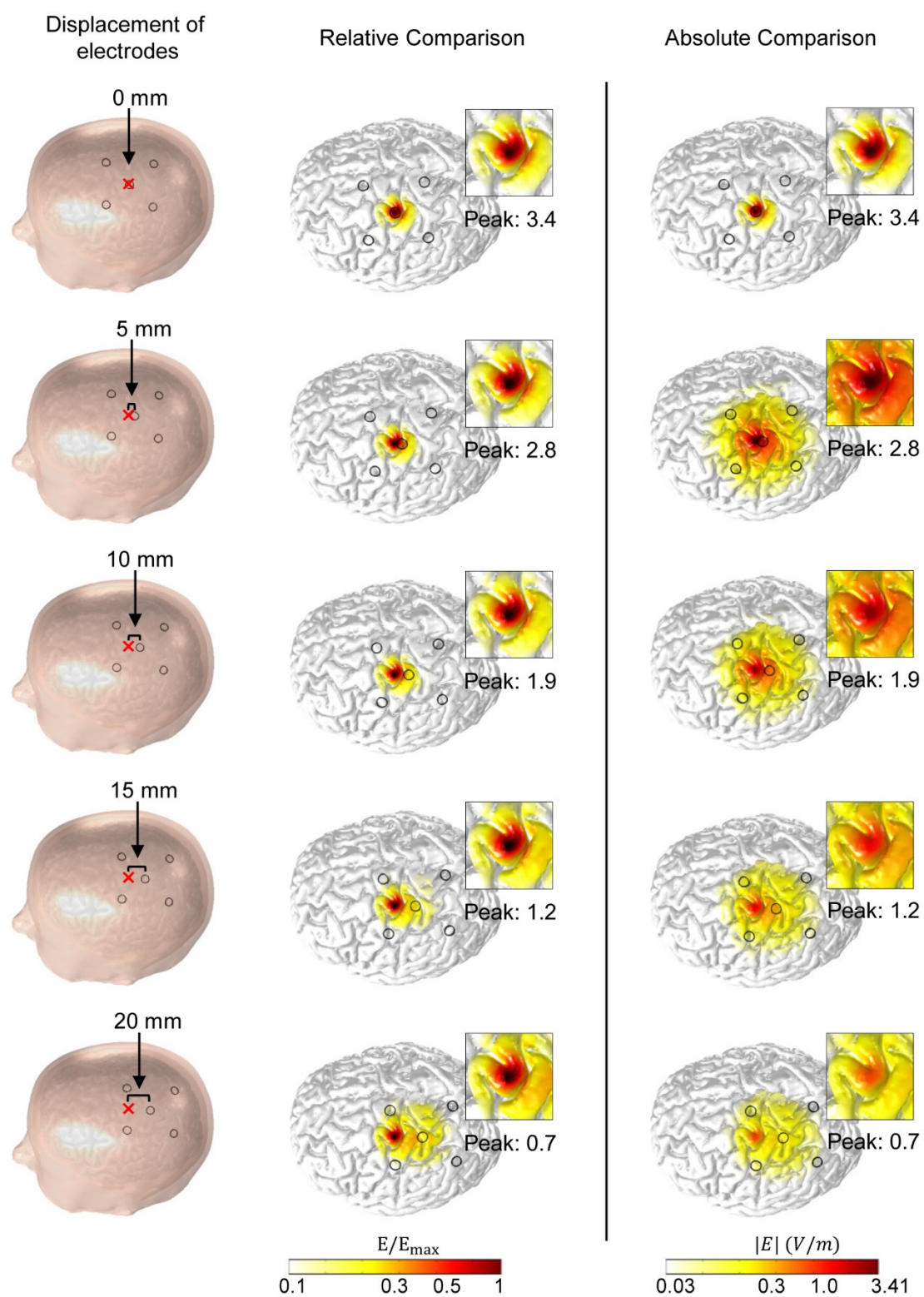


Figure 5.10. EF distributions with respect to displacement of the center (active) electrode relative to the transcranial channel. In the 1st column, character ‘x’ indicates the fixed location of the transcranial channel that targets the ROI, and circles represent electrodes positioned in a circular fashion with the center electrode surrounded by four return electrodes. A T-shaped channel was used here. In the 2nd column, the color scales were adjusted to the peak value of EFs, while in the 3rd column, the color scale was fixed to the EF peak value with no displacement.

under the target electrode,^{16,23,24} as most of the current applied is shunted because of the high impedance of the scalp and skull dispersion. Recently, Datta et al.^{23,26} proposed HD-tDCS and showed that it results in greater targeted brain modulation compared to conventional tDCS, as the electrode montage of tDCS can shape the induced current distribution.^{21,25,26,167} They revealed that it induces the maximal magnitude of the stimulus-induced EF directly beneath the active electrode, and enhanced spatial focality compared to the conventional tDCS. However, HD-tDCS induced EF distributions on the brain are relatively widespread compared to an invasive approach, because intermediate tissues (e.g., scalp, skull, CSF) disturb the current flow produced by HD-tDCS, while an invasive approach has no obstacles. To achieve neuromodulation that is targeted with minimal invasiveness, we introduced HD-tDCS combined with the transcranial channel. It improves stimulus efficacy in terms of higher intensity and focality; however, as far as we know, it has been proposed only conceptually and its effects have not been investigated. Therefore, our computational study demonstrated the ways in which the transcranial channel improves the efficiency of stimulation effects.

As the transcranial channel has fewer shunting effects and conveys injected current to the brain through the relatively highly conductive material, it has greater stimulus efficiency at the target area, as is shown by the stimulus-induced EF distributions between the conventional HD-tDCS with and without the transcranial channel (Figure 5.2). While most previous computational studies have investigated the model leverage in terms of EF intensity based on the assumption that such EF is correlated with the physiological changes desired,^{19,26,37,168} the neural excitability is affected not only by the magnitude of EF, but also by the orientation to the cortical neurons and their morphology.^{55,56,60} Thus, we further investigated the response of variable relative polarization in each compartment of L5 and L3 PNs by including the transcranial channel. The general neuronal responses were hyperpolarization of the upper part of the dendrites and depolarization in the other compartments. This is consistent with the response of PNs to radially-directed uniform EF,^{55,56}

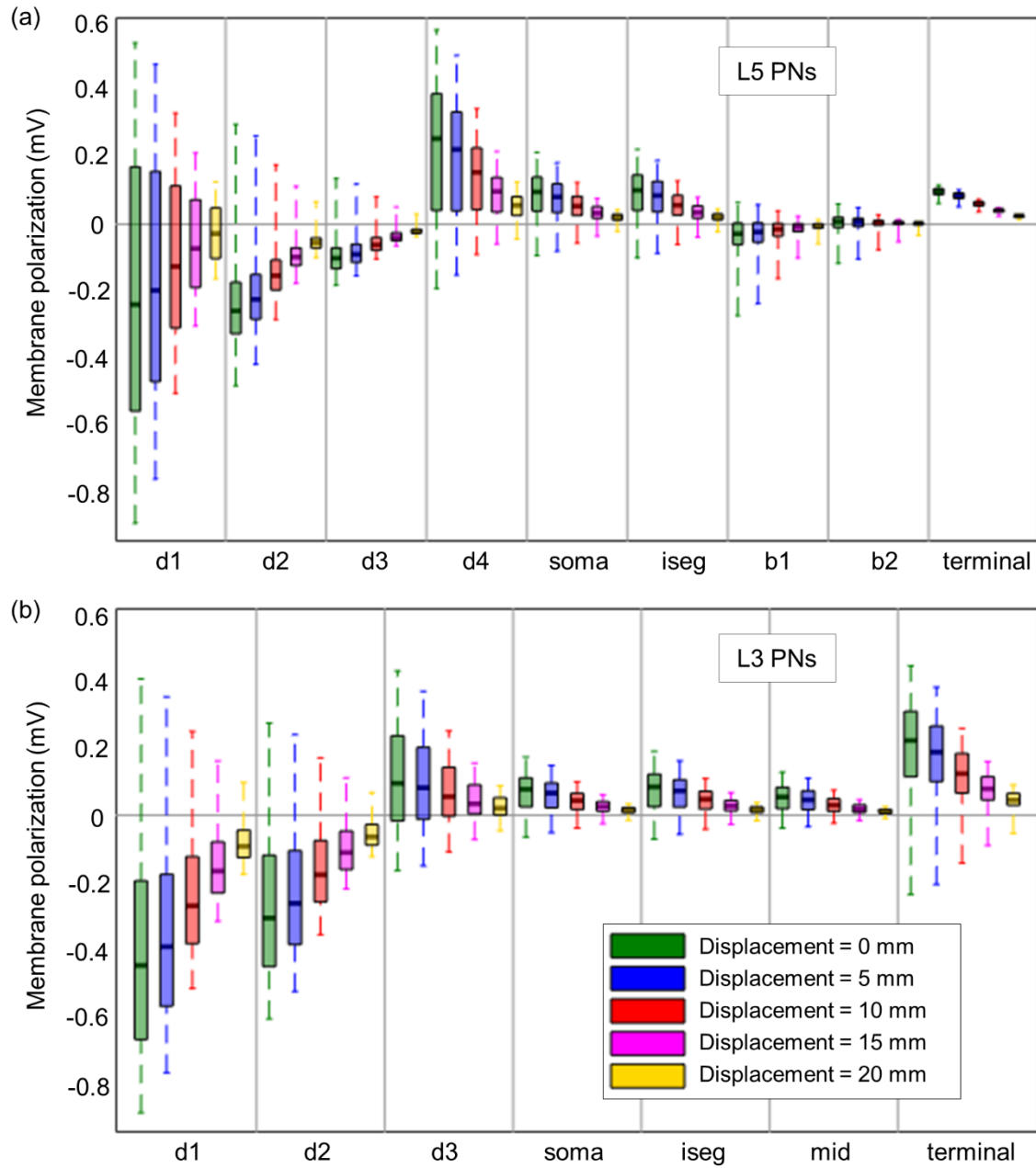


Figure 5.11 The distributions of membrane polarization in neuronal compartments (ROI) in L5 (a) and L3 PNs (b). Displacement of the center electrode relative to the transcranial channel varied in increments of 5 mm. The median and the first quartile to the third quartile of membrane polarization in the neuronal compartments are illustrated; whiskers indicate maximum and minimum membrane polarizations in the compartments.

because the modeled PNs were located on the top of the gyrus perpendicular to the cortex, and thus the extracellular fields to the PNs flowed predominantly perpendicular to the cortical surface. The membrane polarization in the conventional HD-tDCS model without the transcranial channel had a relatively smaller variation within the ROI, while HD-tDCS with the transcranial channel increased it. This indicates that, in accordance with EF distributions, the transcranial channel delivered a focused stimulus to the PNs in ROI compared to the conventional HD-tDCS without the transcranial channel.

We inspected the EFs that were decomposed into radial and tangential components (Figure 5.2) and estimated what components of the induced EFs contributed to modulating the polarizations of PNs. We found that PNs were preferentially polarized by radial field (Figure 5.4); this is because radial field is in the direction of the primary axis of PNs within the GM that were oriented perpendicular to the cortical surface. Therefore, we could extrapolate the neural polarization patterns using the radial component of EFs; however, there were some exceptions in the axon of L5 PN. The axon of L5 PN showed inconsistent patterns with the spatial extent of radial field; this is because the axon of L3 PN was located within the GM, however, the axon of L5 PN was further extended to the WM; the axon of L5 PN after crossing the interface between the GM and WM had different directionality to radial field, as shown in Figure 5.3(a).

The PNs showed polarization in a compartment-specific manner in that they were hyperpolarized at dendrites in the superficial cortex, and were depolarized at both soma and axon initial segment. Somatic polarization may be associated with spontaneous activity^{115,169} and synaptic efficacy^{170,171}. Dendrites and axon may play a significant role in the somatic polarization. 41 Thus, we observed that somata depolarization varied depending on dendritic morphology (Figure 5.8). Furthermore, polarization of the dendrites and axon may influence synaptic processing.¹⁶² Therefore, it is necessary to quantify compartment-specific responses to induced EF.

In this study, we demonstrated that the T-type channel with a 7 mm diameter was the most effective approach. A reasonably acceptable displacement range between the stimulus electrode and the transcranial channel was 5 mm, since it produced higher than 80% performance compared to the case in which there was no displacement. Although the displacement of the active electrode reached 20 mm, we observed that the membrane polarization induced by the inclusion of the transcranial channel was higher than that of the conventional HD-tDCS without the transcranial channel. In addition, substrates around the transcranial

channel were believed to reduce shunting of the current (not shown here); however, this yielded a slightly reduced polarization, and we observed no substantial difference compared to the case without substrates.

The enhanced intensity and focality of EF by combining tDCS and the transcranial channel can be expected in the study from Datta et al., who investigated the influence of skull defects and skull plates, having higher conductivity relative to the skull on tDCS induced EF.¹⁵⁴ They found that the defects altered the intensity and location of current flow and suggested that the higher conductive materials might be beneficial in targeting brain regions. The study of Datta et al. was proposed to find the changes of the overall current flow patterns by the presence of skull defects or skull plates. However, we focused how to maximize both EFs and neural polarizations by higher conductive materials that act as a preferential pathway. We simulated not only the realistic EF distributions but also neural responses using the compartmental models of PNs, and found different polarization patterns at specific neural compartment that cannot be estimated by induced EF. Furthermore, we investigated the dimension of the transcranial channel and the reasonable range of electrode displacement that maximizes neural polarizations.

In accordance with the safety issues of the study from Datta et al., the increased magnitude of induced EF due to high conductive materials might cause potential safety concerns.¹⁵⁴ The concentration of the induced current can be predicted, and we could control the magnitude of the injected current. In addition, according to Wingeier et al., who proposed the conceptual models of the transcranial channel, a heat absorbing or cooling device might be combined to reduce the induced heat when a temperature exceeds a predetermined limit.¹⁵¹ In addition, we may expect possible electrochemical reactions at the tissue-channel interface through the tissue-electrode interface. To transfer the external current into the brain area targeted, the electric current flows into surrounding tissue and is converted into ion movement. Then, some undesirable reactions may be induced, for example, production of possible toxic substances and denaturation of proteins. This is often referred to faradaic current, which is absorbed by a reversed electrochemical reaction by tailing phase of stimulus and by controlling the charge passes per phase in order to minimize the faradaic current.¹⁵¹ The proposed modeling results presented a preliminary study for the use of the transcranial channel; thus, further investigation on potential safety concerns should be done prior to clinical application. The present study is a first step towards understanding the basis of how the transcranial channel helps to convey the external current to the brain effectively and the underlying mechanisms of cellular

responses.

The transcranial channel, combined with HD-tDCS, is proposed for better targeting with reduced shunting effects and provides a stable procedure by fixing maximum excitability at the target area, because the transcranial channel is implanted. Further, applying multiple transcranial channels could tailor the stimulus-induced polarization with respect to specific target area. Therefore, when the transcranial channel is used with repetitive tDCS, it may help to induce prolonged, stabilized and lasting effect and to treat a variety of neurological disorders. Particularly, the transcranial channel may be beneficial for rehabilitation for strokes that are caused by motor defect and focal epileptic cortex, because the transcranial channel restricts its effects to the focal target area.

The accuracy of the dimensions and conductivity values incorporated in the volume conduction head model may be a dominant factor in computational studies.^{19,23,45} In this study, we applied anatomically realistic head geometry derived from MRI data, but the dura mater was constructed arbitrarily by dilating the boundary between the CSF and skull layer. According to the normal anatomical model section of the BrainWeb Simulated Brain Database,¹⁵⁸ the skull layer includes the dura mater generally, but when the dura is thin, it could be included in the CSF layer due to a partial volume effect. To test the effects of dura mater, we compared the conventional HD-tDCS model with and without dura mater. The Model with the dura mater increased the induced EF strength, EF peak, and somatic polarization slightly, but changing the dura mater by shrinking or dilating the boundary between the CSF/skull did not alter the results substantially. We used the computational head model assigned to isotropic conductivity. The effects of anisotropic conductivity in brain stimulation have been addressed widely,^{40,41,44,45,58,80} and Suh et al. reported that there is a significant effect on stimulus-induced EF that is dependent on anisotropic skull conductivity. However, Shahid et al. suggested that anisotropy does not modulate significant changes in comparisons across montages. Therefore, although this work includes inherent modeling limitations as a preliminary study, it may increase our understanding of the ways in which the transcranial channel coupled with HD-tDCS affect cellular modulation.

Stimulation with the conventional tDCS that induces a broadly distributed EF might be desirable when the target area is defined poorly.^{23,168} However, recent research has addressed the ability of focal stimulation to achieve more refined targeting of neuromodulation,^{20,21,24–29,49,50,85,86,168} because the increased focality of stimulation might improve the functional interpretation of stimulation effects, as the outcomes of

brain stimulation are linked to the target area. Furthermore, once the target areas are determined, targeted neuromodulation might be paramount and avoid unwanted effects in other brain areas. To investigate the influence of the focal stimulation, Kuo et al.²⁴ compared the conventional tDCS with HD-tDCS in a neurophysiological study and found a delayed peak of excitability with longer lasting after-effects after HD-tDCS compared to the conventional tDCS; this might be due to the differential modulation of different groups of neurons. Clearly, there are numerous types of neuronal models that may be related to therapeutic tDCS results. Therefore, this computational study should be extended to other kinds of neuronal models in order to understand the underlying mechanisms of the focality effects.

VI. Conclusion and discussion

In this thesis, we proposed multi-scale computational models encompassing noninvasive to invasive brain stimulation. For invasive stimulation, especially subdural cortical stimulation, we found that through stimulus-induced electric field, excitability was focused at the top of gyrus only; however, at the microscopic level, target sites were different according to stimulus polarities: anodal stimulation activated the top of gyrus and cathodal stimulation stimulated the lip and bank area along to sulcus with higher excitation thresholds. Furthermore, we found that increasing the realism of head model in both geometry and electrical properties was a critical factor.

Then one of the noninvasive approaches, transcranial magnetic stimulation, was investigated. The neural excitabilities based on induced electric field and the threshold of cortical neurons were characterized as a function of coil orientations. While major neural excitability was focused in the lip and bank along the sulcal wall, the magnitude of the electric fields was highest at the top of the gyrus consistent with varying coil orientations; however, the electric field component orthogonal to the gray matter surface showed quite matching directionality with the neural excitability. The standard coil orientation that is 45 degree above the hand-knob induced higher excitability in the motor cortex, while an opposite coil orientation had higher excitability focused on postcentral gyrus.

Lastly, a semi-invasive approach was proposed, which is the transcranial channel which increased the focality and magnitude of neuromodulation. Furthermore, we suggested the appropriate dimension of the channel diameter and acceptable range of displacement between stimulus electrodes and the transcranial channel.

In this thesis, the cellular activation was roughly estimated via a stimulus-induced electric field, and through neuronal models we can observe the detail responses such as initiation sites, activation thresholds, and different polarization patterns according to each compartment. The limitations of this study are those neural excitabilities are restricted to the motor cortex and individualized neuronal activations can be observed. The stimulus target area can be extended in the future through tractography using diffusion tensor imaging. Furthermore, the direct and indirect activations by inhibitory and excitatory interneurons should be considered. Rusu et al. proposed morphologically reconstructed layer 5 and layer 3 pyramidal neurons that

connected each other and reproduced direct and indirect responses. We can explore indirect responses by combining connected neuronal models with the anatomically realistic head model by using the multiscale modeling we proposed herein.

References

1. Di Lazzaro, V. *et al.* Comparison of descending volleys evoked by transcranial and epidural motor cortex stimulation in a conscious patient with bulbar pain. *Clin. Neurophysiol.* **115**, 834–838 (2004).
2. Hanajima, R., Ashby, P., Lang, A. E. & Lozano, A. M. Effects of acute stimulation through contacts placed on the motor cortex for chronic stimulation. *Clin. Neurophysiol.* **113**, 635–641 (2002).
3. Holsheimer, J. *et al.* The role of intra-operative motor evoked potentials in the optimization of chronic cortical stimulation for the treatment of neuropathic pain. *Clin. Neurophysiol.* **118**, 2287–2296 (2007).
4. Lefaucheur, J.-P., Holsheimer, J., Goujon, C., Keravel, Y. & Nguyen, J.-P. Descending volleys generated by efficacious epidural motor cortex stimulation in patients with chronic neuropathic pain. *Exp. Neurol.* **223**, 609–614 (2010).
5. Brown, J. A., Lutsep, H., Cramer, S. C. & Weinand, M. Motor cortex stimulation for enhancement of recovery after stroke: Case report. *Neurol. Res.* **25**, 815–818 (2003).
6. Brown, J. A., Lutsep, H. L., Weinand, M. & Cramer, S. C. Motor Cortex Stimulation for the Enhancement of Recovery from Stroke: A Prospective, Multicenter Safety Study: *Neurosurgery* **58**, 464–473 (2006).
7. Canavero, S., Bonicalzi, V., Intonti, S., Crasto, S. & Castellano, G. Effects of Bilateral Extradural Cortical Stimulation for Plegic Stroke Rehabilitation. *Neuromodulation Technol. Neural Interface* **9**, 28–33 (2006).
8. Levy, R. *et al.* Cortical stimulation for the rehabilitation of patients with hemiparetic stroke: a multicenter feasibility study of safety and efficacy. *J. Neurosurg.* **108**, 707–714 (2008).
9. Canavero, S. & Paolotti, R. Extradural motor cortex stimulation for advanced Parkinson's disease: Case report. *Mov. Disord.* **15**, 169–171 (2000).
10. Canavero, S. *et al.* Extradural motor cortex stimulation for advanced Parkinson disease. *J. Neurosurg.* **97**, 1208–1211 (2002).
11. Pagni, C. A. *et al.* Results by motor cortex stimulation in treatment of focal dystonia, Parkinson's disease and post-ictal spasticity. The experience of the Italian Study Group of the Italian Neurosurgical Society. in *Reconstructive Neurosurgery* (eds. Chiu, P. D. W.-T. *et al.*) 13–21 (Springer Vienna, 2008).
12. Picillo, M. *et al.* Subdural Continuous Theta Burst Stimulation of the Motor Cortex in Essential Tremor. *Brain Stimul. Basic Transl. Clin. Res. Neuromodulation* **8**, 840–842 (2015).
13. Tsubokawa, T., Katayama, Y., Yamamoto, T., Hirayama, T. & Koyama, S. Chronic Motor Cortex Stimulation for the Treatment of Central Pain. in *Advances in Stereotactic and Functional Neurosurgery* 9 (eds. Hitchcock, P. E. R. *et al.*) 137–139 (Springer Vienna, 1991). doi:10.1007/978-3-7091-9160-6_37
14. George, M. S. *et al.* Daily repetitive transcranial magnetic stimulation (rTMS) improves mood in depression. *Neuroreport* **6**, 1853–1856 (1995).
15. Pascual-Leone, A., Amedi, A., Fregni, F. & Merabet, L. B. The Plastic Human Brain Cortex. *Annu. Rev. Neurosci.* **28**, 377–401 (2005).
16. Canavero, S. *Textbook of therapeutic cortical stimulation*. (Nova Biomedical Books, 2009).
17. Canavero, S. *Textbook of Cortical Brain Stimulation*. (De Gruyter Open, 2014).
18. Plow, E. B., Carey, J. R., Nudo, R. J. & Pascual-Leone, A. Invasive Cortical Stimulation to Promote Recovery of Function After Stroke A Critical Appraisal. *Stroke* **40**, 1926–1931 (2009).
19. Bikson, M., Rahman, A., Datta, A., Fregni, F. & Merabet, L. High-Resolution Modeling Assisted Design of Customized and Individualized Transcranial Direct Current Stimulation Protocols. *Neuromodulation Technol. Neural Interface* **15**, 306–315 (2012).
20. Wagner, T., Valero-Cabre, A. & Pascual-Leone, A. Noninvasive Human Brain Stimulation. *Annu. Rev.*

- Biomed. Eng.* **9**, 527–565 (2007).
21. Edwards, D. *et al.* Physiological and modeling evidence for focal transcranial electrical brain stimulation in humans: A basis for high-definition tDCS. *NeuroImage* **74**, 266–275 (2013).
 22. Nitsche, M. A. *et al.* Transcranial direct current stimulation: State of the art 2008. *Brain Stimulat.* **1**, 206–223 (2008).
 23. Datta, A. *et al.* Gyri-precise head model of transcranial direct current stimulation: Improved spatial focality using a ring electrode versus conventional rectangular pad. *Brain Stimulat.* **2**, 201–207.e1 (2009).
 24. Kuo, H.-I. *et al.* Comparing Cortical Plasticity Induced by Conventional and High-Definition 4×1 Ring tDCS: A Neurophysiological Study. *Brain Stimulat.* **6**, 644–648 (2013).
 25. Nitsche, M. A. *et al.* Shaping the Effects of Transcranial Direct Current Stimulation of the Human Motor Cortex. *J. Neurophysiol.* **97**, 3109–3117 (2007).
 26. Datta, A., Elwassif, M., Battaglia, F. & Bikson, M. Transcranial current stimulation focality using disc and ring electrode configurations: FEM analysis. *J. Neural Eng.* **5**, 163–174 (2008).
 27. Boreckardt, J. J. *et al.* A Pilot Study of the Tolerability and Effects of High-Definition Transcranial Direct Current Stimulation (HD-tDCS) on Pain Perception. *J. Pain* **13**, 112–120 (2012).
 28. Villamar, M. F. *et al.* Focal Modulation of the Primary Motor Cortex in Fibromyalgia Using 4×1 -Ring High-Definition Transcranial Direct Current Stimulation (HD-tDCS): Immediate and Delayed Analgesic Effects of Cathodal and Anodal Stimulation. *J. Pain* **14**, 371–383 (2013).
 29. Nikolin, S., Loo, C. K., Bai, S., Dokos, S. & Martin, D. M. Focalised stimulation using high definition transcranial direct current stimulation (HD-tDCS) to investigate declarative verbal learning and memory functioning. *NeuroImage* **117**, 11–19 (2015).
 30. Barker, A. T., Freeston, I. L., Jalinous, R. & Jarratt, J. A. Clinical evaluation of conduction time measurements in central motor pathways using magnetic stimulation of human brain. *The Lancet* **327**, 1325–1326 (1986).
 31. Wagner, T., Valero-Cabre, A. & Pascual-Leone, A. Noninvasive Human Brain Stimulation. *Annu. Rev. Biomed. Eng.* **9**, 527–565 (2007).
 32. Barker, A. T., Jalinous, R. & Freeston, I. L. Non-invasive magnetic stimulation of human motor cortex. *The Lancet* **325**, 1106–1107 (1985).
 33. Di Lazzaro, V. *et al.* The diagnostic value of motor evoked potentials. *Clin. Neurophysiol.* **110**, 1297–1307 (1999).
 34. Schulz, R., Gerloff, C. & Hummel, F. C. Non-invasive brain stimulation in neurological diseases. *Neuropharmacology* **64**, 579–587 (2013).
 35. Wongsarnpigoon, A. & Grill, W. M. Computational modeling of epidural cortical stimulation. *J. Neural Eng.* **5**, 443–454 (2008).
 36. Seo, H., Kim, D. & Jun, S. C. A comparative study of the 3D precentral gyrus model for unipolar and bipolar current stimulations. *2012 Annu. Int. Conf. IEEE Eng. Med. Biol. Soc. EMBC* 1892–1895 (2012). doi:10.1109/EMBC.2012.6346322
 37. Datta, A., Baker, J. M., Bikson, M. & Fridriksson, J. Individualized model predicts brain current flow during transcranial direct-current stimulation treatment in responsive stroke patient. *Brain Stimulat.* **4**, 169–174 (2011).
 38. Kim, D., Seo, H., Kim, H.-I. & Jun, S. C. The computational study of subdural cortical stimulation: A quantitative analysis of voltage and current stimulation. *2012 Annu. Int. Conf. IEEE Eng. Med. Biol. Soc. EMBC* 867–870 (2012). doi:10.1109/EMBC.2012.6346069
 39. Parazzini, M. *et al.* Modelling the electric field and the current density generated by cerebellar transcranial DC stimulation in humans. *Clin. Neurophysiol.* **125**, 577–584 (2014).
 40. Suh, H. S., Lee, W. H. & Kim, T.-S. Influence of anisotropic conductivity in the skull and white matter on transcranial direct current stimulation via an anatomically realistic finite element head model. *Phys.*

- Med. Biol.* **57**, 6961 (2012).
41. Windhoff, M., Opitz, A. & Thielscher, A. Electric field calculations in brain stimulation based on finite elements: An optimized processing pipeline for the generation and usage of accurate individual head models. *Hum. Brain Mapp.* **34**, 923–935 (2013).
 42. De Lucia, M., Parker, G. J. M., Embleton, K., Newton, J. M. & Walsh, V. Diffusion tensor MRI-based estimation of the influence of brain tissue anisotropy on the effects of transcranial magnetic stimulation. *NeuroImage* **36**, 1159–1170 (2007).
 43. Shahid, S., Wen, P. & Ahfock, T. Assessment of electric field distribution in anisotropic cortical and subcortical regions under the influence of tDCS. *Bioelectromagnetics* **35**, 41–57 (2014).
 44. Shahid, S. S., Bikson, M., Salman, H., Wen, P. & Ahfock, T. The value and cost of complexity in predictive modelling: role of tissue anisotropic conductivity and fibre tracts in neuromodulation. *J. Neural Eng.* **11**, 036002 (2014).
 45. Wagner, S. *et al.* Investigation of tDCS volume conduction effects in a highly realistic head model. *J. Neural Eng.* **11**, 016002 (2014).
 46. Bai, S., Dokos, S., Ho, K.-A. & Loo, C. A computational modelling study of transcranial direct current stimulation montages used in depression. *NeuroImage* **87**, 332–344 (2014).
 47. Nummenmaa, A. *et al.* Targeting of White Matter Tracts with Transcranial Magnetic Stimulation. *Brain Stimulat.* **7**, 80–84 (2014).
 48. Nummenmaa, A. *et al.* Comparison of spherical and realistically shaped boundary element head models for transcranial magnetic stimulation navigation. *Clin. Neurophysiol.* **124**, 1995–2007 (2013).
 49. Ruffini, G., Fox, M. D., Ripolles, O., Miranda, P. C. & Pascual-Leone, A. Optimization of multifocal transcranial current stimulation for weighted cortical pattern targeting from realistic modeling of electric fields. *NeuroImage* **89**, 216–225 (2014).
 50. Truong, D. Q., Magerowski, G., Blackburn, G. L., Bikson, M. & Alonso-Alonso, M. Computational modeling of transcranial direct current stimulation (tDCS) in obesity: Impact of head fat and dose guidelines. *NeuroImage Clin.* **2**, 759–766 (2013).
 51. Kamitani, Y., Bhalodia, V. M., Kubota, Y. & Shimojo, S. A model of magnetic stimulation of neocortical neurons. *Neurocomputing* **38–40**, 697–703 (2001).
 52. Manola, L., Roelofsen, B. H., Holsheimer, D. J., Marani, E. & Geelen, J. Modelling motor cortex stimulation for chronic pain control: Electrical potential field, activating functions and responses of simple nerve fibre models. *Med. Biol. Eng. Comput.* **43**, 335–343 (2005).
 53. Manola, L., Holsheimer, J., Veltink, P. & Buitenweg, J. R. Anodal vs cathodal stimulation of motor cortex: A modeling study. *Clin. Neurophysiol.* **118**, 464–474 (2007).
 54. Pashut, T. *et al.* Mechanisms of Magnetic Stimulation of Central Nervous System Neurons. *PLOS Comput Biol* **7**, e1002022 (2011).
 55. Radman, T., Ramos, R. L., Brumberg, J. C. & Bikson, M. Role of cortical cell type and morphology in subthreshold and suprathreshold uniform electric field stimulation in vitro. *Brain Stimulat.* **2**, 215–228.e3 (2009).
 56. Rahman, A. *et al.* Cellular effects of acute direct current stimulation: somatic and synaptic terminal effects. *J. Physiol.* **591**, 2563–2578 (2013).
 57. Rusu, C. V., Murakami, M., Ziemann, U. & Triesch, J. A Model of TMS-induced I-waves in Motor Cortex. *Brain Stimulat.* **7**, 401–414 (2014).
 58. Seo, H., Kim, D. & Jun, S. C. Computational Study of Subdural Cortical Stimulation: Effects of Simulating Anisotropic Conductivity on Activation of Cortical Neurons. *PLoS ONE* **10**, e0128590 (2015).
 59. Seo, H., Kim, D. & Jun, S. C. Effect of Anatomically Realistic Full-Head Model on Activation of Cortical Neurons in Subdural Cortical Stimulation—A Computational Study. *Sci. Rep.* **6**, 27353 (2016).
 60. Seo, H., Schaworonkow, N., Jun, S. C. & Triesch, J. A multi-scale computational model of the effects

- of TMS on motor cortex. *F1000Research* **5**, 1945 (2016).
61. Wongsarnpigoon, A. & Grill, W. M. Computer-based model of epidural motor cortex stimulation: Effects of electrode position and geometry on activation of cortical neurons. *Clin. Neurophysiol.* **123**, 160–172 (2012).
 62. Wu, T., Fan, J., Lee, K. S. & Li, X. Cortical neuron activation induced by electromagnetic stimulation: a quantitative analysis via modelling and simulation. *J. Comput. Neurosci.* **40**, 51–64 (2016).
 63. Zwartjes, D. G. M. *et al.* Motor cortex stimulation for Parkinson's disease: a modelling study. *J. Neural Eng.* **9**, 056005 (2012).
 64. Deng, Z.-D., Lisanby, S. H. & Peterchev, A. V. Electric field strength and focality in electroconvulsive therapy and magnetic seizure therapy: a finite element simulation study. *J. Neural Eng.* **8**, 016007 (2011).
 65. Roth, B. J., Saypol, J. M., Hallett, M. & Cohen, L. G. A theoretical calculation of the electric field induced in the cortex during magnetic stimulation. *Electroencephalogr. Clin. Neurophysiol. Potentials Sect.* **81**, 47–56 (1991).
 66. Saypol, J. M., Roth, B. J., Cohen, L. G. & Hallett, M. A theoretical comparison of electric and magnetic stimulation of the brain. *Ann. Biomed. Eng.* **19**, 317–328
 67. Thielscher, A. & Kammer, T. Linking Physics with Physiology in TMS: A Sphere Field Model to Determine the Cortical Stimulation Site in TMS. *NeuroImage* **17**, 1117–1130 (2002).
 68. Ferdjallah, M., Bostick, F. X. & Barr, R. E. Potential and current density distributions of cranial electrotherapy stimulation (CES) in a four-concentric-spheres model. *IEEE Trans. Biomed. Eng.* **43**, 939–943 (1996).
 69. Rush, S. & Driscoll, D. A. Current distribution in the brain from surface electrodes. *Anesth. Analg.* **47**, 717–723 (1968).
 70. Kim, D., Jun, S. C. & Kim, H.-I. Computational study of subdural and epidural cortical stimulation of the motor cortex. *2011 Annu. Int. Conf. IEEE Eng. Med. Biol. Soc. EMBC* 7226–7229 (2011). doi:10.1109/IEMBS.2011.6091826
 71. Heller, L. & Hulsteyn, D. B. van. Brain stimulation using electromagnetic sources: theoretical aspects. *Biophys. J.* **63**, 129–138 (1992).
 72. Wang, W. & Eisenberg, S. R. A three-dimensional finite element method for computing magnetically induced currents in tissues. *IEEE Trans. Magn.* **30**, 5015–5023 (1994).
 73. Janssen, A. M., Oostendorp, T. F. & Stegeman, D. F. The coil orientation dependency of the electric field induced by TMS for M1 and other brain areas. *J. NeuroEngineering Rehabil.* **12**, 47 (2015).
 74. Wagner, S. Optimizing TCS and TMS Multi-sensor Setups Using Realistic Head Models. *Dr. Diss.* (2015).
 75. Chen, M. & Mogul, D. J. Using Increased Structural Detail of the Cortex to Improve the Accuracy of Modeling the Effects of Transcranial Magnetic Stimulation on Neocortical Activation. *IEEE Trans. Biomed. Eng.* **57**, 1216–1226 (2010).
 76. Biro, O. & Preis, K. On the use of the magnetic vector potential in the finite-element analysis of three-dimensional eddy currents. *IEEE Trans. Magn.* **25**, 3145–3159 (1989).
 77. Opitz, A., Windhoff, M., Heidemann, R. M., Turner, R. & Thielscher, A. How the brain tissue shapes the electric field induced by transcranial magnetic stimulation. *NeuroImage* **58**, 849–859 (2011).
 78. Rj, I., J, R. & J, K. Transcranial magnetic stimulation--a new tool for functional imaging of the brain. *Crit. Rev. Biomed. Eng.* **27**, 241–284 (1998).
 79. Janssen, A. M. *et al.* The influence of sulcus width on simulated electric fields induced by transcranial magnetic stimulation. *Phys. Med. Biol.* **58**, 4881 (2013).
 80. Kim, D., Seo, H., Kim, H.-I. & Jun, S. C. Computational Study on Subdural Cortical Stimulation - The Influence of the Head Geometry, Anisotropic Conductivity, and Electrode Configuration. *PLoS ONE* **9**, e108028 (2014).

81. Krings, T. *et al.* Stereotactic transcranial magnetic stimulation: correlation with direct electrical cortical stimulation. *Neurosurgery* **41**, 1319-1325; discussion 1325-1326 (1997).
82. Deng, Z.-D., Lisanby, S. H. & Peterchev, A. V. Electric field depth–focality tradeoff in transcranial magnetic stimulation: Simulation comparison of 50 coil designs. *Brain Stimulat.* **6**, 1–13 (2013).
83. Salinas, F. S., Lancaster, J. L. & Fox, P. T. Detailed 3D models of the induced electric field of transcranial magnetic stimulation coils. *Phys. Med. Biol.* **52**, 2879 (2007).
84. Nitsche, M. A. & Paulus, W. Excitability changes induced in the human motor cortex by weak transcranial direct current stimulation. *J. Physiol.* **527**, 633–639 (2000).
85. Wagner, S., Burger, M. & Wolters, C. H. An optimization approach for well-targeted transcranial direct current stimulation. *SIAM J. Appl. Math.* **76**, 2154–2174 (2016).
86. Schmidt, C., Wagner, S., Burger, M., Rienen, U. van & Wolters, C. H. Impact of uncertain head tissue conductivity in the optimization of transcranial direct current stimulation for an auditory target. *J. Neural Eng.* **12**, 046028 (2015).
87. Roth, B. J. & Bassar, P. J. A model of the stimulation of a nerve fiber by electromagnetic induction. *IEEE Trans. Biomed. Eng.* **37**, 588–597 (1990).
88. Davey, N. J., Romaguère, P., Maskill, D. W. & Ellaway, P. H. Suppression of voluntary motor activity revealed using transcranial magnetic stimulation of the motor cortex in man. *J. Physiol.* **477**, 223–235 (1994).
89. Nagarajan, S. S., Durand, D. M. & Warman, E. N. Effects of induced electric fields on finite neuronal structures: a simulation study. *IEEE Trans. Biomed. Eng.* **40**, 1175–1188 (1993).
90. Larkum, M. E., Nevian, T., Sandler, M., Polsky, A. & Schiller, J. Synaptic Integration in Tuft Dendrites of Layer 5 Pyramidal Neurons: A New Unifying Principle. *Science* **325**, 756–760 (2009).
91. Hu, W. *et al.* Distinct contributions of Nav1.6 and Nav1.2 in action potential initiation and backpropagation. *Nat. Neurosci.* **12**, 996–1002 (2009).
92. Rattay, F. Analysis of models for extracellular fiber stimulation. *IEEE Trans. Biomed. Eng.* **36**, 676–682 (1989).
93. McIntyre, C. C. & Grill, W. M. Excitation of Central Nervous System Neurons by Nonuniform Electric Fields. *Biophys. J.* **76**, 878–888 (1999).
94. Goodwin, B. D. & Butson, C. R. Subject-Specific Multiscale Modeling to Investigate Effects of Transcranial Magnetic Stimulation. *Neuromodulation Technol. Neural Interface* **18**, 694–704 (2015).
95. Grant, P. F. & Lowery, M. M. Electric field distribution in a finite-volume head model of deep brain stimulation. *Med. Eng. Phys.* **31**, 1095–1103 (2009).
96. Seo, H., Kim, D. & Jun, S. C. Comparison of neuronal excitation between extruded slab partial head model and full head model in subdural cortical stimulation. *2013 35th Annu. Int. Conf. IEEE Eng. Med. Biol. Soc. EMBC* 241–244 (2013). doi:10.1109/EMBC.2013.6609482
97. Park, J. S., Chung, M. S., Hwang, S. B., Shin, B.-S. & Park, H. S. Visible Korean Human: Its techniques and applications. *Clin. Anat.* **19**, 216–224 (2006).
98. Fischl, B., Sereno, M. I. & Dale, A. M. Cortical Surface-Based Analysis: II: Inflation, Flattening, and a Surface-Based Coordinate System. *NeuroImage* **9**, 195–207 (1999).
99. Smith, S. M. *et al.* Advances in functional and structural MR image analysis and implementation as FSL. *NeuroImage* **23**, **Supplement 1**, S208–S219 (2004).
100. Scientific Computing and Imaging Institute (SCI). Seg3d: Volumetric image segmentation and visualization.
101. Fang, Q. & Boas, D. A. Tetrahedral mesh generation from volumetric binary and grayscale images. in *IEEE International Symposium on Biomedical Imaging: From Nano to Macro, 2009. ISBI '09* 1142–1145 (2009). doi:10.1109/ISBI.2009.5193259
102. Si, H. & Gärtner, K. Meshing Piecewise Linear Complexes by Constrained Delaunay Tetrahedralizations. in *Proceedings of the 14th International Meshing Roundtable* (ed. Hanks, B. W.)

- 147–163 (Springer Berlin Heidelberg, 2005).
103. Geddes, L. A. & Baker, L. E. The specific resistance of biological material—A compendium of data for the biomedical engineer and physiologist. *Med. Biol. Eng.* **5**, 271–293 (1967).
 104. Akhtari, M. *et al.* Conductivities of Three-Layer Live Human Skull. *Brain Topogr.* **14**, 151–167 (2002).
 105. Baumann, S. B., Wozny, D. R., Kelly, S. K. & Meno, F. M. The electrical conductivity of human cerebrospinal fluid at body temperature. *IEEE Trans. Biomed. Eng.* **44**, 220–223 (1997).
 106. Gabriel, C., Gabriel, S. & Corthout, E. The dielectric properties of biological tissues: I. Literature survey. *Phys. Med. Biol.* **41**, 2231 (1996).
 107. Basser, P. J., Mattiello, J. & LeBihan, D. MR diffusion tensor spectroscopy and imaging. *Biophys. J.* **66**, 259–267 (1994).
 108. Nicholson, P. W. Specific impedance of cerebral white matter. *Exp. Neurol.* **13**, 386–401 (1965).
 109. Gorman, A. L. Differential patterns of activation of the pyramidal system elicited by surface anodal and cathodal cortical stimulation. *J. Neurophysiol.* **29**, 547–564 (1966).
 110. Mainen, Z. F. & Sejnowski, T. J. Influence of dendritic structure on firing pattern in model neocortical neurons. *Nature* **382**, 363–366 (1996).
 111. Hines, M. L. & Carnevale, N. T. The NEURON Simulation Environment. *Neural Comput.* **9**, 1179–1209 (1997).
 112. DeFelipe, J., Alonso-Nanclares, L. & Arellano, J. I. Microstructure of the neocortex: Comparative aspects. *J. Neurocytol.* **31**, 299–316 (2002).
 113. Gordon, B. *et al.* Parameters for direct cortical electrical stimulation in the human: histopathologic confirmation. *Electroencephalogr. Clin. Neurophysiol.* **75**, 371–377 (1990).
 114. Yousry, T. A. *et al.* Localization of the motor hand area to a knob on the precentral gyrus. A new landmark. *Brain* **120**, 141–157 (1997).
 115. Hern, J. E. C., Landgren, S., Phillips, C. G. & Porter, R. Selective excitation of corticofugal neurones by surface-anodal stimulation of the baboon's motor cortex. *J. Physiol.* **161**, 73–90 (1962).
 116. Phillips, C. G. & Porter, R. Unifocal and bifocal stimulation of the motor cortex. *J. Physiol.* **162**, 532–538 (1962).
 117. Miranda, P. C., Correia, L., Salvador, R. & Basser, P. J. Tissue heterogeneity as a mechanism for localized neural stimulation by applied electric fields. *Phys. Med. Biol.* **52**, 5603–5617 (2007).
 118. Lazzaro, V. D. *et al.* Effects of voluntary contraction on descending volleys evoked by transcranial electrical stimulation over the motor cortex hand area in conscious humans. *Exp. Brain Res.* **124**, 525–528 (1999).
 119. Chan, C. Y. & Nicholson, C. Modulation by applied electric fields of Purkinje and stellate cell activity in the isolated turtle cerebellum. *J. Physiol.* **371**, 89–114 (1986).
 120. Dale, A. M., Fischl, B. & Sereno, M. I. Cortical Surface-Based Analysis: I. Segmentation and Surface Reconstruction. *NeuroImage* **9**, 179–194 (1999).
 121. Güllmar, D., Haueisen, J. & Reichenbach, J. R. Influence of anisotropic electrical conductivity in white matter tissue on the EEG/MEG forward and inverse solution. A high-resolution whole head simulation study. *NeuroImage* **51**, 145–163 (2010).
 122. Wolters, C. H. *et al.* Influence of tissue conductivity anisotropy on EEG/MEG field and return current computation in a realistic head model: A simulation and visualization study using high-resolution finite element modeling. *NeuroImage* **30**, 813–826 (2006).
 123. Tuch, D. S., Wedeen, V. J., Dale, A. M., George, J. S. & Belliveau, J. W. Conductivity tensor mapping of the human brain using diffusion tensor MRI. *Proc. Natl. Acad. Sci.* **98**, 11697–11701 (2001).
 124. Hallez, H., Vanrumste, B., Hese, P. V., Delputte, S. & Lemahieu, I. Dipole estimation errors due to differences in modeling anisotropic conductivities in realistic head models for EEG source analysis. *Phys. Med. Biol.* **53**, 1877 (2008).
 125. Holsheimer, J., Nguyen, J.-P., Lefaucheur, J.-P. & Manola, L. Cathodal, anodal or bifocal stimulation

- of the motor cortex in the management of chronic pain? in *Operative Neuromodulation* (eds. Sakas, D. E. & Simpson, B. A.) 57–66 (Springer Vienna, 2007).
126. Patton, H. D. & Amassian, V. E. Single and multiple-unit analysis of cortical stage of pyramidal tract activation. *J. Neurophysiol.* **17**, 345–363 (1954).
 127. Struijk, J. J., Holsheimer, J., van der Heide, G. G. & Boom, H. B. K. Recruitment of dorsal column fibers in spinal cord stimulation: influence of collateral branching. *IEEE Trans. Biomed. Eng.* **39**, 903–912 (1992).
 128. Geeter, N. D., Dupré, L. & Crevecoeur, G. Modeling transcranial magnetic stimulation from the induced electric fields to the membrane potentials along tractography-based white matter fiber tracts. *J. Neural Eng.* **13**, 026028 (2016).
 129. Thielscher, A., Opitz, A. & Windhoff, M. Impact of the gyral geometry on the electric field induced by transcranial magnetic stimulation. *NeuroImage* **54**, 234–243 (2011).
 130. Kim, D. *et al.* Validation of Computational Studies for Electrical Brain Stimulation With Phantom Head Experiments. *Brain Stimulat.* **8**, 914–925 (2015).
 131. Laakso, I., Hirata, A. & Ugawa, Y. Effects of coil orientation on the electric field induced by TMS over the hand motor area. *Phys. Med. Biol.* **59**, 203 (2014).
 132. Opitz, A. *et al.* Physiological observations validate finite element models for estimating subject-specific electric field distributions induced by transcranial magnetic stimulation of the human motor cortex. *NeuroImage* **81**, 253–264 (2013).
 133. Lenz, M. *et al.* Repetitive magnetic stimulation induces plasticity of excitatory postsynapses on proximal dendrites of cultured mouse CA1 pyramidal neurons. *Brain Struct. Funct.* **220**, 3323–3337 (2014).
 134. Lenz, M. *et al.* Repetitive magnetic stimulation induces plasticity of inhibitory synapses. *Nat. Commun.* **7**, 10020 (2016).
 135. Salvador, R., Silva, S., Basser, P. J. & Miranda, P. C. Determining which mechanisms lead to activation in the motor cortex: A modeling study of transcranial magnetic stimulation using realistic stimulus waveforms and sulcal geometry. *Clin. Neurophysiol.* **122**, 748–758 (2011).
 136. Silva, S., Basser, P. J. & Miranda, P. C. Elucidating the mechanisms and loci of neuronal excitation by transcranial magnetic stimulation using a finite element model of a cortical sulcus. *Clin. Neurophysiol.* **119**, 2405–2413 (2008).
 137. Thielscher, A., Antunes, A. & Saturnino, G. B. Field modeling for transcranial magnetic stimulation: A useful tool to understand the physiological effects of TMS? *2015 37th Annu. Int. Conf. IEEE Eng. Med. Biol. Soc. EMBC* 222–225 (2015). doi:10.1109/EMBC.2015.7318340
 138. Attene, M. A lightweight approach to repairing digitized polygon meshes. *Vis. Comput.* **26**, 1393–1406 (2010).
 139. Geuzaine, C. & Remacle, J.-F. Gmsh: A 3-D finite element mesh generator with built-in pre- and post-processing facilities. *Int. J. Numer. Methods Eng.* **79**, 1309–1331 (2009).
 140. Renard, Y. & Pommier, J. GetFEM++ Homepage — GetFEM++. *getfem, A Generic Finite Element Library in C. Documentation* (2010). Available at: <http://download.gna.org/getfem/html/homepage/>.
 141. Fox, P. T. *et al.* Column-based model of electric field excitation of cerebral cortex. *Hum. Brain Mapp.* **22**, 1–14 (2004).
 142. Kammer, T., Beck, S., Thielscher, A., Laubis-Herrmann, U. & Topka, H. Motor thresholds in humans: a transcranial magnetic stimulation study comparing different pulse waveforms, current directions and stimulator types. *Clin. Neurophysiol.* **112**, 250–258 (2001).
 143. Krieg, T. D., Salinas, F. S., Narayana, S., Fox, P. T. & Mogul, D. J. Computational and experimental analysis of TMS-induced electric field vectors critical to neuronal activation. *J. Neural Eng.* **12**, 046014 (2015).
 144. Krieg, T. D., Salinas, F. S., Narayana, S., Fox, P. T. & Mogul, D. J. PET-Based Confirmation of

- Orientation Sensitivity of TMS-Induced Cortical Activation in Humans. *Brain Stimulat.* **6**, 898–904 (2013).
145. Day, B. L. *et al.* Electric and magnetic stimulation of human motor cortex: surface EMG and single motor unit responses. *J. Physiol.* **412**, 449–473 (1989).
 146. Di Lazzaro, V. *et al.* I-wave origin and modulation. *Brain Stimulat.* **5**, 512–525 (2012).
 147. Brasil-Neto, J. P. *et al.* Optimal focal transcranial magnetic activation of the human motor cortex: effects of coil orientation, shape of the induced current pulse, and stimulus intensity. *J. Clin. Neurophysiol. Off. Publ. Am. Electroencephalogr. Soc.* **9**, 132–136 (1992).
 148. Mills, K. R., Boniface, S. J. & Schubert, M. Magnetic brain stimulation with a double coil: the importance of coil orientation. *Electroencephalogr. Clin. Neurophysiol. Potentials Sect.* **85**, 17–21 (1992).
 149. Baker, S. N., Olivier, E. & Lemon, R. N. Task-related variation in corticospinal output evoked by transcranial magnetic stimulation in the macaque monkey. *J. Physiol.* **488**, 795–801 (1995).
 150. Edgley, S. A., Eyre, J. A., Lemon, R. N. & Miller, S. Excitation of the corticospinal tract by electromagnetic and electrical stimulation of the scalp in the macaque monkey. *J. Physiol.* **425**, 301–320 (1990).
 151. Wingeier, B. & Pless, B. Systems, methods and devices for a skull/brain interface. (2015).
 152. Miranda, P. C., Lomarev, M. & Hallett, M. Modeling the current distribution during transcranial direct current stimulation. *Clin. Neurophysiol.* **117**, 1623–1629 (2006).
 153. Wagner, T. *et al.* Transcranial direct current stimulation: A computer-based human model study. *NeuroImage* **35**, 1113–1124 (2007).
 154. Datta, A., Bikson, M. & Fregni, F. Transcranial direct current stimulation in patients with skull defects and skull plates: High-resolution computational FEM study of factors altering cortical current flow. *NeuroImage* **52**, 1268–1278 (2010).
 155. Lee, M. *et al.* What is the optimal anodal electrode position for inducing corticomotor excitability changes in transcranial direct current stimulation? *Neurosci. Lett.* **584**, 347–350 (2015).
 156. Bashkatov, A. N. *et al.* Glucose and Mannitol Diffusion in Human Dura Mater. *Biophys. J.* **85**, 3310–3318 (2003).
 157. Perdue, K. L. & Diamond, S. G. T1 magnetic resonance imaging head segmentation for diffuse optical tomography and electroencephalography. *J. Biomed. Opt.* **19**, 026011–026011 (2014).
 158. Aubert-Broche, B., Griffin, M., Pike, G. B., Evans, A. C. & Collins, D. L. Twenty New Digital Brain Phantoms for Creation of Validation Image Data Bases. *IEEE Trans. Med. Imaging* **25**, 1410–1416 (2006).
 159. Schaefer, A. T., Larkum, M. E., Sakmann, B. & Roth, A. Coincidence Detection in Pyramidal Neurons Is Tuned by Their Dendritic Branching Pattern. *J. Neurophysiol.* **89**, 3143–3154 (2003).
 160. Mountcastle, V. B. *Perceptual Neuroscience: The Cerebral Cortex*. (Harvard University Press, 1998).
 161. Elston, G. N. Cortex, Cognition and the Cell: New Insights into the Pyramidal Neuron and Prefrontal Function. *Cereb. Cortex* **13**, 1124–1138 (2003).
 162. Bikson, M. *et al.* Effects of uniform extracellular DC electric fields on excitability in rat hippocampal slices in vitro. *J. Physiol.* **557**, 175–190 (2004).
 163. Barnett, G. H., Burgess, R. C., Skipper, G. J., Edwards, C. R. & Luders, H. Epidural Peg Electrodes for the Presurgical Evaluation of Intractable Epilepsy. *Neurosurgery* **27**, 113–115 (1990).
 164. Drury, I. *et al.* Ictal patterns in temporal lobe epilepsy recorded by epidural screw electrodes. *Electroencephalogr. Clin. Neurophysiol.* **102**, 167–174 (1997).
 165. Ross, D. A., Henry, T. R. & Dickinson, L. D. A Percutaneous Epidural Screw Electrode for Intracranial Electroencephalogram recordings. *Neurosurgery* **32**, 332–334 (1993).
 166. Shorvon, S. D., Perucca, E. & Jr, J. E. *The Treatment of Epilepsy*. (John Wiley & Sons, 2009).
 167. Moliadze, V., Antal, A. & Paulus, W. Electrode-distance dependent after-effects of transcranial direct

- and random noise stimulation with extracephalic reference electrodes. *Clin. Neurophysiol.* **121**, 2165–2171 (2010).
168. Dmochowski, J. P., Datta, A., Bikson, M., Su, Y. & Parra, L. C. Optimized multi-electrode stimulation increases focality and intensity at target. *J. Neural Eng.* **8**, 046011 (2011).
 169. Terzuolo, C. A. & Bullock, T. H. MEASUREMENT OF IMPOSED VOLTAGE GRADIENT ADEQUATE TO MODULATE NEURONAL FIRING*. *Proc. Natl. Acad. Sci. U. S. A.* **42**, 687–694 (1956).
 170. Fröhlich, F. & McCormick, D. A. Endogenous Electric Fields May Guide Neocortical Network Activity. *Neuron* **67**, 129–143 (2010).
 171. Reato, D., Rahman, A., Bikson, M. & Parra, L. C. Low-Intensity Electrical Stimulation Affects Network Dynamics by Modulating Population Rate and Spike Timing. *J. Neurosci.* **30**, 15067–15079 (2010).

Acknowledgements

바이오컴퓨팅 연구실에서 보낸 지난 석사/박사 기간은 저에게 매우 소중한 시간이었습니다. 먼저 부족한 저를 박사과정까지 지도해 주신 전성찬 교수님께 진심으로 감사드립니다. 연구뿐만 아니라 제가 나아가는 길에 아낌없는 조언과 용기를 주셨습니다. 졸업 후 지금까지 배운 가르침을 기반으로 더 나은 연구자가 되려 합니다. 또한 논문 심사 과정에서 많은 가르침을 주신 윤국진 교수님, 이현주 교수님, 이보름 교수님, 그리고 독일 University of Münster의 Carsten Wolters 박사님께도 감사를 드립니다.

광주과학기술원에서 머문 6년이란 시간 동안 함께한 연구실 동료들에게도 감사의 마음 전합니다. 많은 일들이 있었습니다. 기쁜 일에 함께 축하해주고 슬픈 일에 위로를 받고 그 밖에 연구실 내에서 함께한 소중한 추억 잊지 않으려 합니다.

마지막으로 사랑하는 저희 가족에게 감사의 마음 전합니다. 존경하는 아빠, 표현하지 않아도 항상 아낌없이 주시는 사랑 덕분에 오랜 공부기간에도 든든히 버틸 수 있었습니다. 사랑하는 엄마, 아직도 엄마의 손길이 필요한 어리고 부족한 딸인 저를 사랑해 주셔서 감사합니다. 더욱 자랑스러운 딸이 되도록 하겠습니다. 언니 바라기인 내 동생 서주희, 동생 임에도 제 삶의 의지가 되어주고 기쁨이 되어주었습니다. 제 동반자인 남편 최우오빠, 든든한 지원군이 되어줘 감사합니다, 그리고 사랑합니다.

많은 분들의 도움으로 막연히 꿈꾸던 대학원 생활이 가치 있게 마무리되었습니다. 다시 한번 모든 분들께 감사드립니다.

Curriculum Vitae

Name : Hyeon Seo
Birth Date : June 12, 1987
Birth Place : Gwangju, Gwangsan-gu, South, Korea
Permanent Address : Gwangju, Gwangsan-gu, South, Korea

Education

2006 – 2010 Mathematics (B.S.)
2010 – 2013 Electrical Engineering and Computer Science (M.S.)
2013 – 2017 Electrical Engineering and Computer Science (Ph.D.)

International Experience

NRF-DAAD Summer Institute Program 2015.07-08
Internship in Frankfurt Institute of Advanced Studies (FIAS), Frankfurt am Main, Germany
Global Leader Project(GLP) Exchange student 2009.03-06
Bulacan State University Language Center, City of Malolos, Philippines

Book

Sergio Canavero, *Textbook of Cortical Brain Stimulation*, Berlin: De Gruyter Open. Retrieved 3 Apr. 2015, from <http://www.degruyter.com/view/product/450127>; Chapter 19 Modelization: Overview, Hyoung-Ihl Kim, Donghyeon Kim, **Hyeon Seo**, Sung Chan Jun,

Publications

Hyeon Seo, Hyoung-Ihl Kim and Sung Chan Jun, "Effect of a Transcranial Channel as a Skull/Brain Interface in High-Definition Transcranial Direct Current Stimulation-A Computational Study," *Scientific Reports*, 2016 (Accepted)

Hyeon Seo, Natalie Schaworonkow, Sung Chan Jun and Jochen Triesch, "A multi-scale computational model of the effects of TMS on motor cortex," *F1000Research*, 2016, **5**

Hyeon Seo, Donghyeon Kim and Sung Chan Jun, "Effect of Anatomically Realistic Full-Head Model on Activation of Cortical Neurons in Subdural Cortical Stimulation-A Computational Study," *Scientific Reports*, 2016, **6**, pp.27353

Hyeon Seo, Donghyeon Kim and Sung Chan Jun, "Effects of Electrode Displacement in High-Definition Transcranial Direct Current Stimulation: A Computational Study," *Proceedings of 38th Annual International Conference of the IEEE Engineering in Medicine and Biology Society*, 2016, pp. 4618-4621.

Hyeon Seo, Donghyeon Kim and Sung Chan Jun, "Computational Study of Subdural Cortical Stimulation: Effects of Simulating Anisotropic Conductivity on Activation of Cortical Neurons," *PLoS ONE*, 2015, **10**, pp.e0128590

Hyeon Seo, Donghyeon Kim and Sung Chan Jun, "The effect of transcranial channel as skull/brain interface in transcranial direct current stimulation," *Brain Stimulation: Basic, Translational, and Clinical Research in Neuromodulation*, 2015, **8(2)**, pp. 420-421.

Hyeon Seo, Donghyeon Kim and Sung Chan Jun, "Comparison of Neuronal Excitation between Extruded Slab Partial Head Model and Full Head Model in Subdural Cortical Stimulation," *Proceedings of 35th Annual International Conference of the IEEE Engineering in Medicine and Biology Society*, 2013, pp. 241-244.

Hyeon Seo, Donghyeon Kim and Sung Chan Jun, "A Comparative Study of the 3D Precentral Gyrus Model for Unipolar and Bipolar Current Stimulations," *Proceedings of 34th Annual International Conference of the IEEE Engineering in Medicine and Biology Society*, Aug. 28 – Sept. 1, 2012, pp. 1892-1895.

Hyeon Seo and Sung Chan Jun, "A Simulation Study of Epidural Cortical Stimulation for Unipolar and Bipolar Current Stimulation," *The Korean Society of Medial and Biological Engineering*, 2012, pp. 335-336.

Hyeon Seo, Wonwoo Lee and Woontack Woo, "Sensor based Image Rectification for Online Patch Learning on Mobile Phones," *The Korean Signal Processing Conference*, 2011, pp. 252-253.

Hyeon Seo, Hyoseok Yoon and Woontack Woo, "Mashup Content Recommendation Based on Social Relationship," *The Korean Institute of Information Scientists and Engineers Korea Computer Congress*, 2010, pp. 54-55.

Donghyeon Kim, **Hyeon Seo**, Hyoung-Ihl Kim and Sung Chan Jun, "Computational Study on Subdural Cortical Stimulation - The Influence of the Head Geometry, Anisotropic Conductivity, and Electrode Configuration," *PLoS ONE*, 2014, **9**, e108028. doi:10.1371/journal.pone.0108028

Donghyeon Kim, **Hyeon Seo**, Mijin Lee and Sung Chan Jun. "E-CoCS: Environment of computational simulator for cortical stimulation." *Biomedical Engineering Letters* 2014 **4(2)**, pp. 186-192.

Donghyeon Kim, **Hyeon Seo**, Hyoung-Ihl Kim and Sung Chan Jun, "The Computational Study of Subdural Cortical Stimulation: A Quantitative Analysis of Voltage and Current Stimulation," *Proceedings of 34th Annual International Conference of the IEEE Engineering in Medicine and Biology Society*, Aug. 28 – Sept. 1, 2012, pp. 867-870.